Theory and interpretation of solar decimetric radio bursts

DOCTORAL THESIS

Ondřejov, 2002 **Miroslav Bárta**

Matematicko-fyzikální fakulta University Karlovy v Praze

a

Astronomický ústav Akademie věd České republiky

DISERTAČNÍ PRÁCE

Theory and interpretation of solar decimetric radio bursts

November 6, 2002

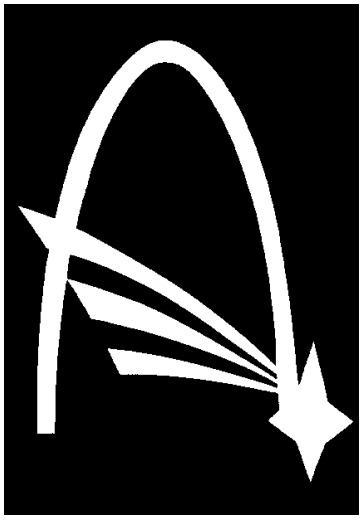

Miroslav Bárta

supervisor: RNDr. Marian Karlický, DrSc.

Cover: The Ondřejov solar radiospectrograph *RT 5* operating in the frequency range 0.8 GHz – 2 GHz (*Photo: J. Havelka*).

Contents

Preface

Solar physics belongs undoubtedly to those branches of astrophysics that experienced very strong development during several past decades. It concerns to progress in both observations as well as basic theoretical concepts.
The large enhancement in data acquisition is due to improvement of classical observational techniques such as classical spectroscopy and photometry in optical band but, above all due to enlargement of range of observable wavelengths to practically whole spectrum of electromagnetic radiation. The classical solar astronomy has developed in various ways. Firstly, new large ground-based telescopes devoted to solar physics were built during last period (i.e. THEMIS, SVST, Dutch Open Telescope). Also storm development of computers and digital technologies generally contributed greatly to optical observations enhancement. It enabled two complementary methods widely used now - adaptive optics and image processing, that at least partly overcomes the image distortions due to Earth atmosphere.
On the other hand, observations on formerly unreachable wavelengths outside the optical band faced us to completely new view on the Sun, particularly on its atmosphere. It was just observations on radio waves that made the first break-through into this *terra incognita* of the Sun's nature. The radiospectrographs and radioheliographs has changed significantly our ideas mainly in the field of solar activity. The other bands of electromagnetic spectrum followed soon after the satellites and space technologies generally had appeared. Let us remind at least some of the space-borne devices that contributed greatly to our knowledge of the processes on the Sun: Skylab (launched 1973) – provided at the first time direct soft X-ray (SXR) images of the Sun, Yohkoh (1991) – SXR imaging, HXR (hard X-ray) integral flux measurement, SOHO (1995) – observations in the optical (solar oscillations and photospheric magnetic field measurements – MDI, coronagraphs LASCO), UV (spectrograph SUMER) and EUV (EIT imaging telescope) spectral bands, or TRACE (1998) – high resolution images in EUV and SXR range of wavelengths. The strong development of satellite solar astronomy continues further as can be demonstrated by recently launched devices - HXRS (2000) – the solar HXR spectrometer on MTI satellite or RHESSI (2002) – HXR high-resolution imaging telescope as well as the new projects planed in near future (Solar B, STEREO).

New discoveries made by these enhanced observational devices changed completely our image of many phenomena on the Sun, especially the image of the solar atmosphere. Hand by hand with these changes the new basic theoretical concepts appeared. Let remind only few of them: the model of solar interior verified by helioseismologic observations, the model of solar magnetic field generation – the concept of the solar dynamo, whole class of models of solar activity and energy release based on magnetic field reconfiguration and reconnection, or new theories on the heating of the solar corona.
Besides of these models describing macroscopic processes on the Sun the class of theoretical concepts necessary for the correct interpretation of observed data had to be developed. The later cover particularly the microphysics of the generation and propagation of the electromagnetic radiation which is, with exception of direct measurements of the solar wind and neutrinos experiments, our unique source of information about the Sun. These are namely the non-LTE

approach to radiative transfer widely used especially in the spectral range from infrared up to UV frequencies, and the theory of generation of the radio waves in the solar corona, particularly the so called "Plasma emission model". The later includes the quasi-linear theory of waves-particles interaction in plasmas (the counterpart of the non-LTE approach on radio frequencies) as well as the non-linear interaction of plasma wave modes.

The main goal of the presented work is just to contribute to the development of the theory of radio radiation, particularly the radiation of the flare plasmas, with emphasis to plasma diagnostics using radio spectral observations of the Sun.
Technically, this work can be divided to several parts. The first two chapters represents an introductory part. The current state of our knowledge of the Sun and solar activity is present there.
The basic formal concepts used in the solar radio radiation theory are summarised in the third chapter.
Finally, the last two chapters contain the core of the work itself. It is based on summary and extension of already published papers by Bárta & Karlický (1999, 2000, 2000b, 2001) and Karlický, Bárta et al. (2001).
The chapter "Interpretation of observed radio spectra" is, as the title indicates, devoted to the identification of mechanisms of radio emission for specific types of radio bursts in decimetric range. The last chapter, "Wave mode conversion" should be regarded as contribution to the theory of the radiation mechanism which is specific particularly for the solar radio emission – already mentioned plasma emission model.

As can be seen, many pains have been taken for solar research. This effort, to which presented work try to be a tiny contribution, has many good reasons and it already has brought its fruits. Besides the deeper knowledge of the processes going on the Sun which itself increases our understanding to the Nature in general, there is a set of problems closely related to solar physics. Above all it is currently frequently discussed question of solar–terrestrial connection and the space weather. This topic overlaps several scientific branches from plasma physics through solar physics and geophysics to biological sciences or information, communication and space technologies. The importance of the problem increases as civilisation becomes dependent on more and more advanced but also more sensitive technology. It is just solar physics that holds the key to the satisfactory forecasting of events which can reach the live on the Earth, due to dominant role of solar processes in the heliosphere.
Another topic closely related to the solar research is the question of thermo-nuclear fusion in devices with magnetic confinement of plasmas – the key subject of contemporary plasma physics. Particularly the problem of anomalous resistivity and wave–particle interactions important for plasma heating in solar flares as well as in tokamacs is solved in close collaboration between these two scientific branches.
Many other examples of various problems in various regions of science to which solution solar research can contribute could be listed. Let us finish with quite recent discovery in the field of fundamental physics strongly influenced by results of solar research. Very soon after the standard model of solar interior had been introduced the measurements of solar neutrino flux started. Well known discrepancies led to doubts about solar core model at the beginning. When its correctness was proved by recent technique of solar oscillations analysis more intensive research was devoted to this topic from the point of view of particle physics. The so called neutrino oscillations – the permutations among three types of neutrinos were discovered what is regarded as important result of quantum field theory and fundamental physics generally.

This brief discussion have hopefully shown the meaning of the solar physics not only for our general understanding to the Universe but also for the applications that may have an economical

impact in modern civilisation. If the effort spent in the solar research will not weaken further new surprising results can be expected in this fascinating field.

Remark on units: In whole the thesis the *SI* system of units is used unless another set is explicitly announced (dimension-less units or, exceptionaly, *CGS* system).

Chapter 1

The Sun and its activity

From the classical astrophysics point of view the Sun is a normal star on the Main Sequence of the HR diagram approximately in the middle of its life. Sun's great importance for physicist resides – besides the generally known fact, that it is absolutely essential for entire the life on the Earth (including the scientists[1]) – in its proximity to the Earth, that allows us – unlike in the case of the other stars – really detailed investigations of basic physical processes forming together the stellar life. Almost all observable information we can obtain about the Sun is due to its interface to the outer space – the solar atmosphere, with exception of direct observations of solar neutrinos and helioseismic waves that reach also the solar interior. However, even the latter are detectable only by means of analysis of the photospheric light and, hence the study of the solar atmosphere plays a key role in the research of the Sun generally.

1.1 Solar atmosphere

Although it is well known fact now that the solar atmosphere is highly inhomogeneous and anisotropic medium with low amount of symmetry, it still can be divided into several concentric layers that differs each other in basic physical parameters significantly. The schematic picture of the averaged plasma parameters depending on the height is shown on Fig. 1.1. According to this figure four layers of the solar atmosphere can be distinguished:

- photosphere,
- chromosphere,
- transition region, and
- corona and solar wind.

Firstly, the properties of the innermost atmospheric shells will be briefly described.

1.1.1 Lower atmosphere – photosphere, chromosphere and the transition region

The photosphere is the deepest layer of the solar atmosphere. It represents the visible surface of the Sun – the energy flux originating in the solar core changes its realisation from the convective to the radiative transfer here, again. Photosphere's thickness is given by mean free path of photons what is about 300 km in the optical band. Prevailing emission mechanism in the photosphere is the thermal emission (also called *bremsstrahlung*, *free-free emission* – see the Chapter 3 by free electrons intercepted by neutral hydrogen atoms and, hence the photospheric light shows broad-band spectrum with maximum approximately in the middle of the interval of visible wavelengths. The corresponding temperature of the photosphere is about 6000 K.

[1] For solar physicist that is true even in double :-)

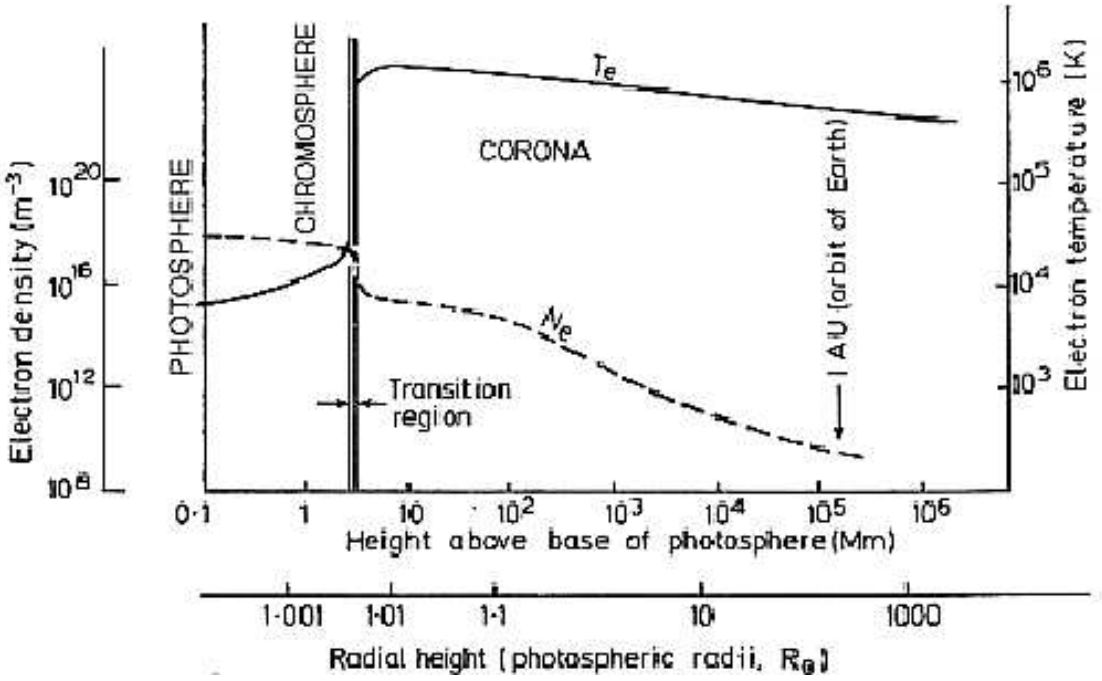

Fig. 1.1: Solar atmosphere height profile. Averaged electron density and temperature is depicted. After Mc Lean & Labrum 1985.

The chromosphere Unlike the photosphere, the chromosphere is observable in specific spectral lines within the optical and UV/EUV bands and in centimetre radio continuum only. The line emission is due to radiative transitions between various states of chromospheric atoms and ions that are excited thermally, but sometimes also by (photospheric) radiation and thus the non-LTE approach is usually required for correct interpretation of observations in chromospheric lines. Since each spectral line is formed in limited extent of physical parameters (temperature, density, radiation field in case of non-LTE lines) that vary particularly with the height in the solar atmosphere, observing in the specific wavelength one views corresponding specific layer of the chromosphere – see Fig. 1.2.

The main feature observed in the chromospheric lines is the *chromospheric network* clearly visible in the Fig. 1.3. The network brightening is believed to be due to enhanced magnetic field which tends to be concentrated by horizontal convective motions in the boundaries of super-granular cells.
Other objects that usually appear in the chromospheric line filtergrams such as *filaments, prominences* etc. will be discussed in the Section 1.2.1.

The transition region As the name indicates this very thin layer represents a transition between rather dense and cold chromosphere and hot and sparse corona. As the temperature and the electron density change approximately by two orders of magnitude here within the thickness of a few hundreds of kilometres the most characteristic property of the transition region is very steep gradient in both these plasma parameters (see Fig. 1.1).

As in the case of chromosphere, the transition region shows the structure which copies that of the super-granular cells and their boundaries. This can be clearly seen particularly in the pictures taken in the lower transition region lines. An example is shown in the Fig. 1.4 made by SUMER instrument in the *C* IV line whose formation temperature is about 10^5 K. In the

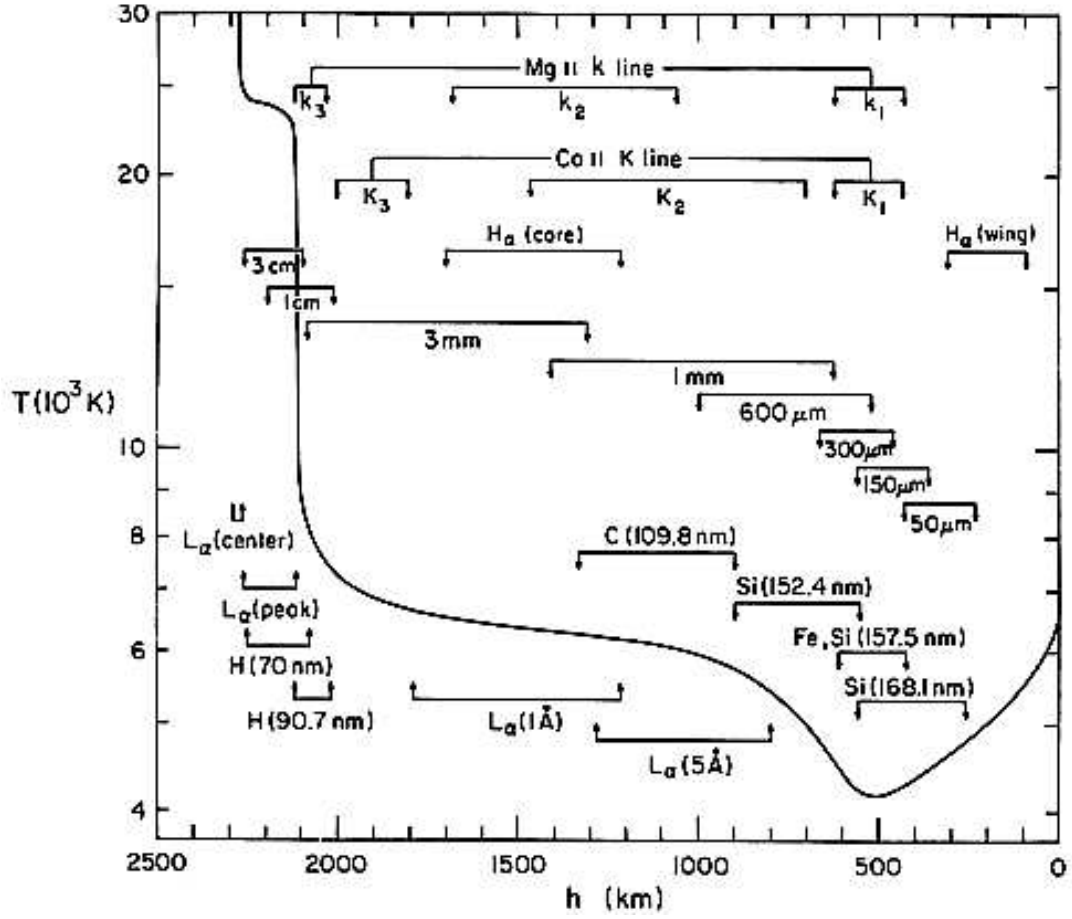

Fig. 1.2: Lower solar atmosphere temperature profile according to the VAL model (`Vernazza et al. 1981`). Height intervals, where various lines are formed, are indicated.

wavelengths formed in higher layers the network becomes less and less sharp what is interpreted as a spread of originally concentrated magnetic field with height.

1.1.2 Solar corona

Solar corona is very hot, sparse, inhomogeneous and frequently also time variable environment. Its first observations are that made during total solar eclipses in white light – see Fig. 1.5. Except the eclipse duration such observations were practically impossible before the space-born devices have appeared because of low intensity of coronal light (due to scattering on free electrons) relatively to the diffusive radiation of the Earth's atmosphere.

The satellite equipments have brought a great break-through to our understanding of solar corona in several ways. Firstly, the observations in white light continua are made permanently and with much larger field of view now (see Fig. 1.6) what allows one to investigate coronal (sometimes very rapid) dynamics. Nevertheless, the essential contribution to our insight to the structure of solar corona have brought the observations on – from the Earth's surface unreachable – UV, EUV and X-ray wavelengths. The common feature seen in this spectral bands clearly shows that corona is highly structured medium of, basically, fibrous appearance – Fig. 1.7 represents a nice example. That indicates, that coronal plasmas is governed by the magnetic field, what is the opposite case to the situation in the lower solar atmosphere where the field lines are

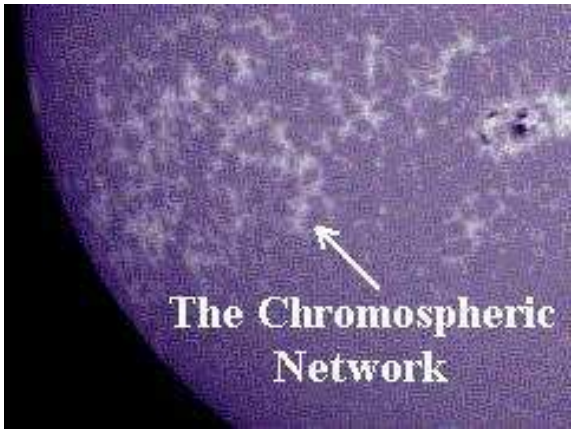

Fig. 1.3: The chromospheric network observed at *Ca* II spectral line (λ = 393.4 nm). Adopted from `SpaceScience.com`

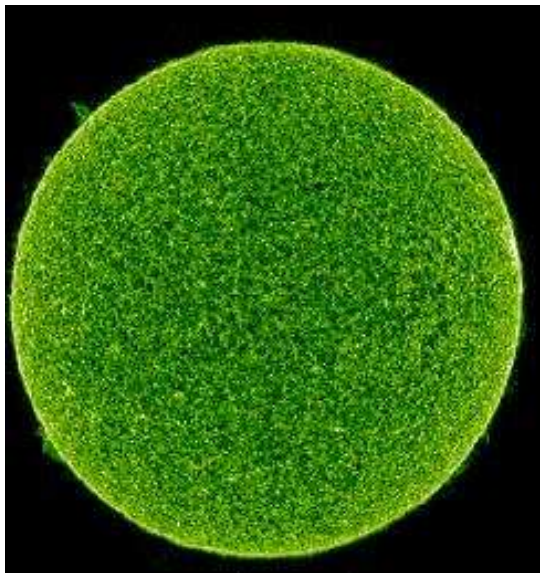

Fig. 1.4: The transition region as seen by the SUMER instrument onboard the SOHO (see `SOHO home webpage`) mission at the *C* IV line (λ = 154.8 nm).

practically dragged by dense matter.

As was already mentioned, besides the soft X-ray thermal continuum solar corona also radiates on many emission lines in the UV and EUV bands. Similarly as in case of chromosphere and the transition region each of these lines is emitted only from places where important physical parameters – particularly the plasma temperature – resides in some characteristic interval. In this sense one can speak about observation of – for example – one and half million degree corona seen in emission line *Fe* XII (19.5 nm) – see the Fig. 1.8.

All the observations show that at the height approximately 0.5 – 1 solar radii above the photosphere there is a change of magnetic field lines topology from mostly closed at the lower heights to open at the higher. At the same heights the hydrostatic equilibrium breaks down as can be derived from coronal density and temperature profiles such as that in Fig. 1.1. Both these facts indicate the transition between (at least at quiet state) stationary corona and outward moving *solar wind*. However, there may be areas on the Sun, where magnetic field lines are opened practically from the solar photosphere. Such places are characterised by density depletions that manifest themselves as darkening on, say, soft X-ray images (the place around the solar north pole on Fig. 1.7). These regions – known as *coronal holes* – represent a significant source of the solar wind, as fast particles can easily escape from the Sun along these open field lines.

1.2 Solar activity

The total power released from the Sun can be regarded as almost constant since it varies within one percent even during the wildest solar processes. Nevertheless, it is clear from the first look that the Sun is rather dynamic object that shows many even very fast variations generally called the *solar activity*. The high significance of active processes comparatively with their rather low effect to the total solar power is particularly due to form at which the energy is released during bursts of solar activity. Especially sudden high enhancement of radiation at X-rays, through

Fig. 1.5: The solar corona as seen during the total solar eclipse 11^{th} August, 1999 (*Photo: J. Kulík).*

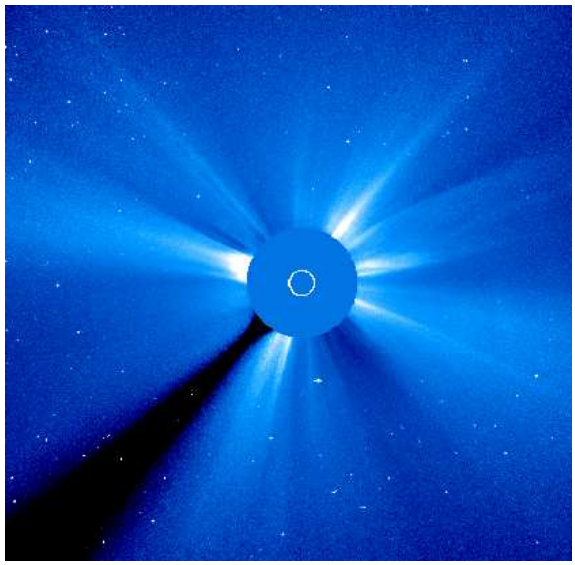

Fig. 1.6: Snapshot of the solar corona made by *LASCO – C3* coronagraph onboard the SOHO probe 17^{th} October, 2002 (`SOHO home webpage`).

EUV, UV and optical lines down to radio frequencies, particle streams accelerated even up to relativistic energies or clouds of magnetised plasmas shotted from the Sun at high speeds are not only very spectacular manifestations of solar activity, but some of them can have far-reaching consequences in whole heliosphere including the Earth and terrestrial civilisation.

The solar activity is very variable in time and space. The time variations are not completely irregular as averaged quantitative measures of the solar activity (such as relative number of sunspots, hard X-ray flux or radio flux at 10 cm) show quasi-periodic behaviour on large time-scales known as 11-year cycle[2].

Also spatial distribution of solar activity at given time is not uniform and dynamic processes occur in some *active regions* at the Sun while the rest of Sun's surface remains almost quiet.

1.2.1 Magnetic field and active regions

The reason for this spatial grouping is given by non-uniform distribution of solar magnetic field that is undoubtedly responsible for all manifestations of solar activity. It is commonly believed, that all dynamical phenomena on the Sun such as solar flares or coronal mass ejections (CMEs) are directly caused by sudden simplification of formerly complex magnetic field what is connected with the release of energy in various forms. Hence, various manifestations of solar activity could be expected in the regions, where the magnetic field geometry is highly complicated as a consequence of convective motions acting together with solar rotation. Justification of such expectations is clearly shown on the Fig. 1.9 where high amount of correlation between the complex magnetic field and active phenomena in various layers of the solar atmosphere is evident:

Photosphere: The most clearly visible structure in the photosphere are groups of *sunspots.* Because of a relative easiness of their observation the sunspots represent the first active event ever discovered at the Sun. From observational point of view they are strictly localised places of lower brightness which is caused by temperature decrease of about

[2]Taking into account changes of polarity of magnetic field the cycle lasts 22 years actually

Fig. 1.7: Soft X-ray image of solar corona observed by SXT telescope onboard the Yohkoh (see `Yohkoh website`) satellite 8^{th} May, 1992.

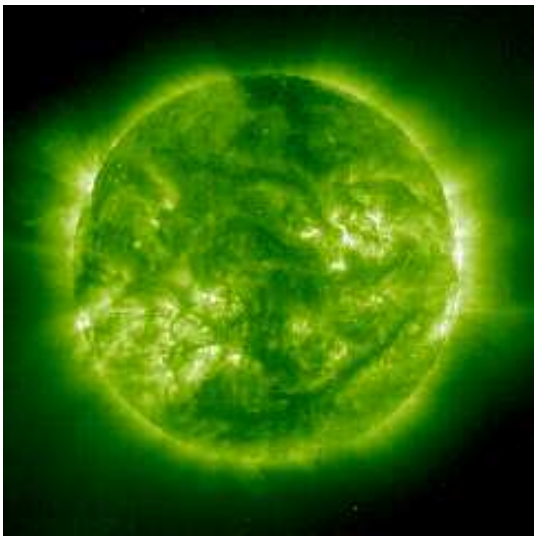

Fig. 1.8: Solar corona as seen by the EIT instrument onboard the SOHO (`SOHO home webpage`) mission at the *Fe* XII line ($\lambda = 19.5$ nm). The formation temperature of the line is about 1.5 MK.

2000 K comparatively with surrounding quiet photosphere. The temperature decrease is explained in terms of suppressed convective motions in the strong sunspot magnetic field. Due to direct bound between the photospheric magnetic field and sunspots the correspondence between regions of complex field geometry and fine-structured groups of sunspots (compare Figs. 1.9 a, b) is obvious.

Chromosphere: As shown on Fig. 1.9c, in the chromosphere above the active region several phenomena can be observed. The most obvious ones are perhaps the bright *plages* in the vicinity of sunspots. Each of them represents a region with enhanced plasma temperature. Another clearly visible structures are the dark *filaments* formed by relatively cold and dense matter. They are supposed to be supported against the solar gravitation by almost horizontal magnetic field. Such a structure is usually rather stable as interaction between the field and dense plasma forms a *magnetic dip* (`Anzer 2002`) – the region with local gravitational potential minimum. Nevertheless, sometimes the stability can be suddenly destroyed and filament consequently disappears what is often accompanied with the filament matter ejection. Such a phenomenon is known as *filament eruption.*
Filaments when seen above the solar limb appear in H_α emission on the other hand and form well known and frequently very spectacular solar *prominences.*

Corona: The active region in the solar corona is dominated by bright *coronal loops* (Fig. 1.9 d). Their rather complicated, distorted geometry (e.g. shear, twisting) reflects the complex topology of magnetic field within the active region. Such a geometry also indicates the electric currents flowing likely along the loops. According to some models the dissipation of these currents is just the still not surely identified source of the coronal heating.
It is commonly believed, that the surplus of magnetic energy stored in this complex coronal field configuration serves as a driver for such dynamic phenomena as are *solar flares* and *coronal mass ejections.*

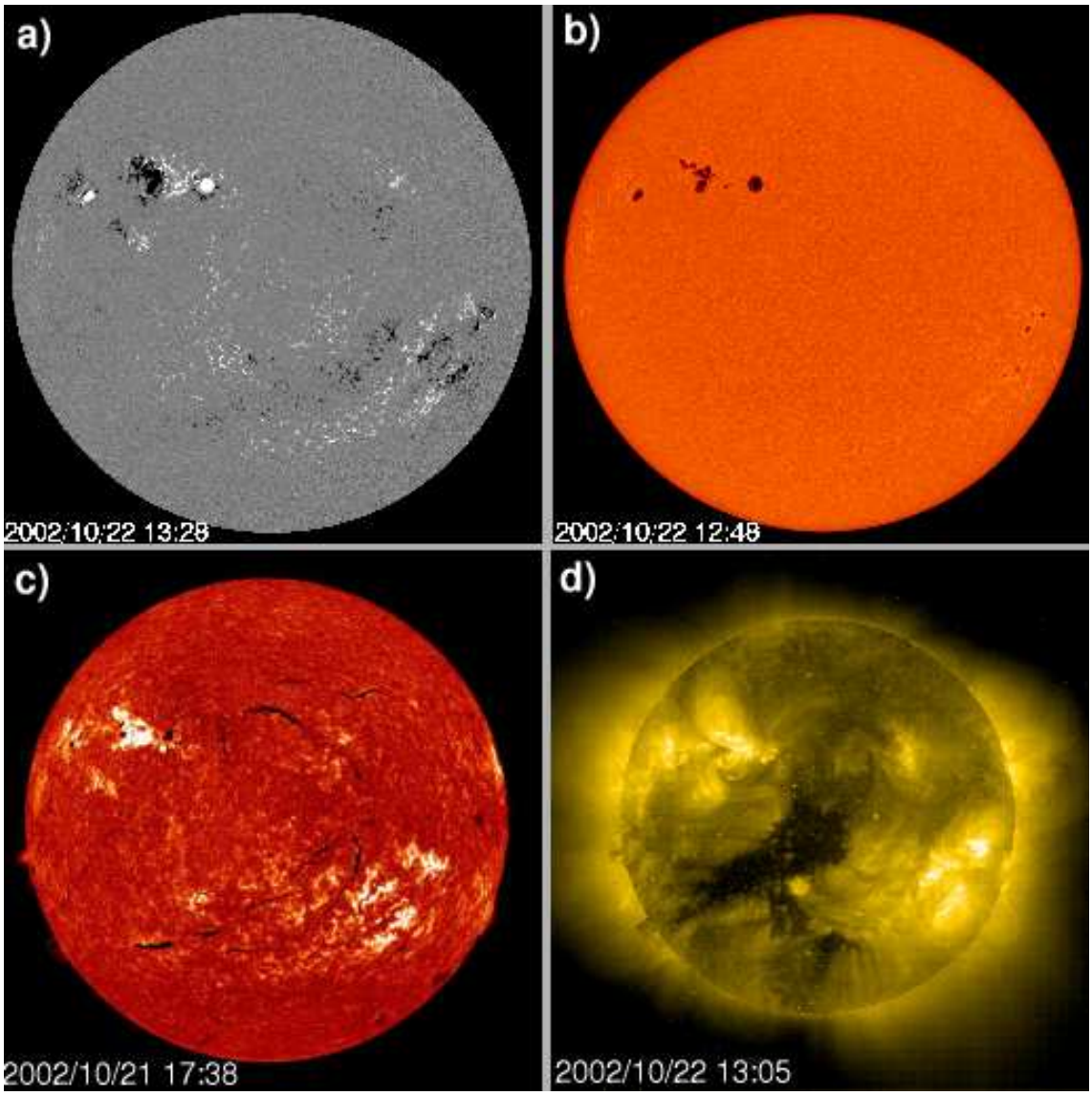

Fig. 1.9: Active region as seen by various instruments corresponding to various layers of the solar atmosphere. All the images were taken at the approximately same time (within one day). **a)** Solar magnetogram made by the *MDI* instrument onboard the SOHO mission (`SOHO home webpage`) shows an active region as an area of enhanced and rather complex photospheric magnetic field. **b)** White light picture of the photosphere taken by the same instrument. The region of the enhanced field corresponds to the group of sunspots. **c)** Full-disc H_α image of the chromosphere by Big Bear Solar Observatory (see `BBSO website`). Activity in the region is pronounced particularly by the bright plages. **d)** Solar corona observed by the *EIT* (`SOHO home webpage`) at the *Fe* XV (28.4 nm) line. The main feature seen in the active region at this layer consists of bright coronal loops.

1.2.2 Solar flares

By the term *flare* is meant rapid, explosive energy release in the solar atmosphere. Firstly the flares were observed as sudden, well localised brightenings of the chromosphere in the H_α line (Fig. 2.3), exceptionally – in case of major events – even in the white light. In virtue of such observations flares were considered as intrinsically chromospheric phenomena what reflects already their former name – *chromospheric flares* – used in older literature. Nevertheless, now – despite the lack of the unambiguous, complete model of flares – it is clear, that the solar flare is much

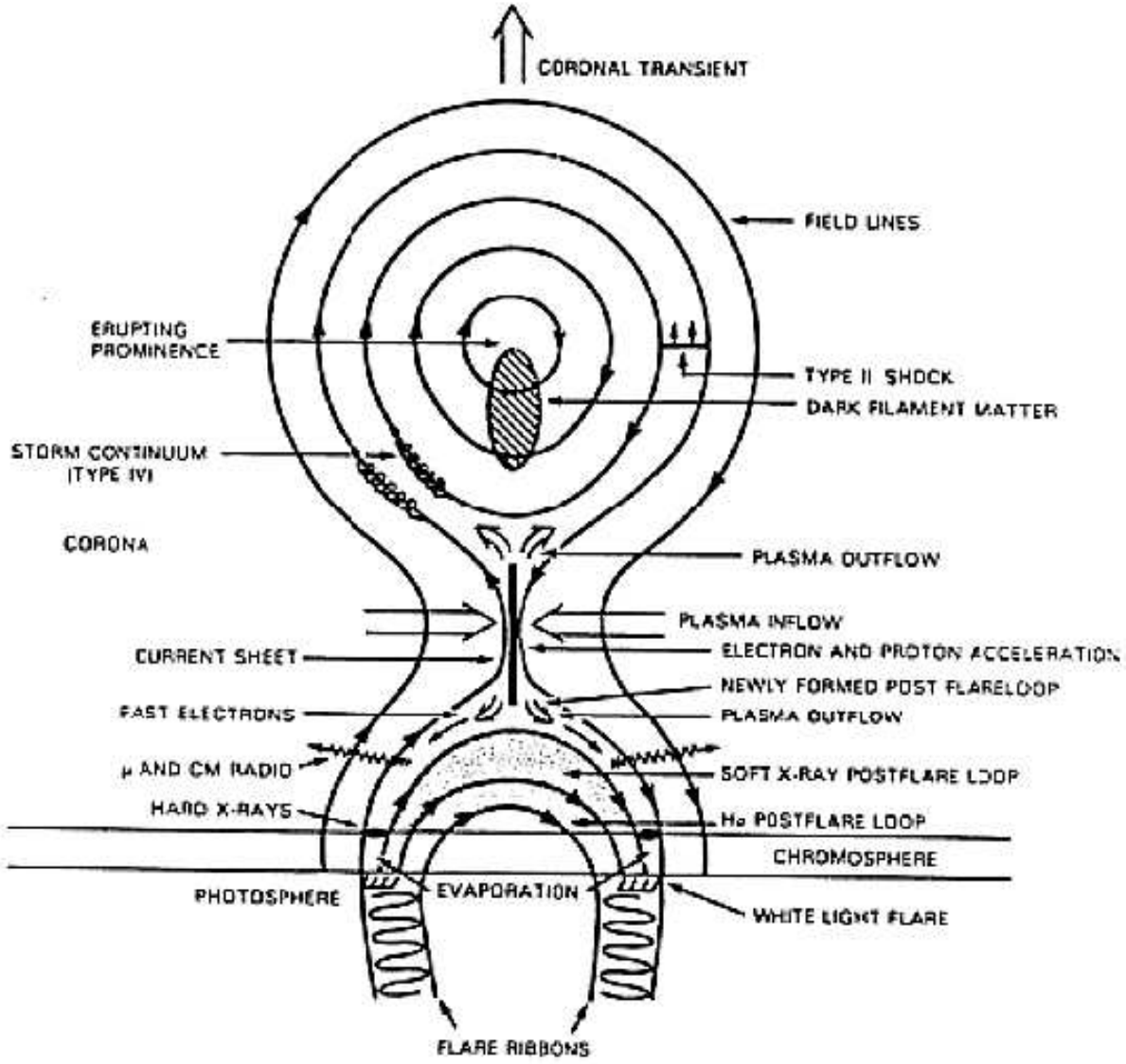

Fig. 1.10: Schematic 2-D view on the magnetic reconnection model of the two-ribbon flare. Adopted from `Martens & Kuin 1989`.

complicated process. It affects all layers of the solar atmosphere and its consequences extend even far to the interplanetary space; however, it seems that the primary flare energy release site is well localised region in the low corona.

Although – as already mentioned – the complete model describing all the flare associated observed phenomena and fitting to all flares ever recorded is still missing, the general idea of a flare as rather fast, localised process converting the magnetically stored energy into its various another forms is commonly accepted. Within this framework the probably most elaborated suggestion of the mechanism of energy release from the magnetic field employs the *reconnection* of the field lines (e.g. `Priest 1984`, `Karlický 1988`). The popular cartoon by Martens & Kuin (`1989`; this and many other flare model schemes are reviewed on `H. Hudson's flare models archive`) showing schematically situation in 2-D is presented at Fig. 1.10. In spite of doubts

concerning general validity of the magnetic field geometry in this model it explains a lot of observational fact found for significant class of solar flares – so called *two-ribbon flares*. The main features of this, and generally whole the class of reconnection-based models, can be summarised in these few points:

- The magnetic energy is transformed into the other forms through the *current sheet* – a thin region occupying rather small extent in the space where the magnetic field gradient is extremely high.

- The current sheet represents an effective particle accelerator – charged particles can gain their kinetic energy in the DC electric field and/or from microturbulence, both the entities are expected in this region. Particle beams as well as broad variety of other types of non-thermal velocity distributions may evolve.

- Accelerated particles move along field lines both up- and down-ward producing intensive radio radiation – see the Chapter 4 (Fig. 4.1). Up-ward moving particles can be detected in the interplanetary space even near the Earth.

- The down-ward moving particles are almost immediately stopped when they reach dense layers of solar chromosphere or photosphere. Part of their kinetic energy is radiated in the form of hard X-rays (Fig. 2.8), the rest is absorbed in the dense layers.

  All these above described non-thermal processes are together known as the *impulsive phase* of the flare.

- This energy deposit leads to sudden intensive heating of the chromospheric/photospheric matter. As a consequence, a shock front propagates up-ward to the corona (e.g. `Varady 2002`) followed by heated chromospheric plasmas (*chromospheric evaporation*). Small part of the deposited beam energy can be also carried out by surface photospheric wave – see Fig. 2.5.

- Warm chromospheric gas produces the bright H_α emission in the footpoints of magnetic loops arcade (Fig. 2.3). Hence, the effect that originally led to the recognition of solar flares represents according to the present model only the secondary process.

- Loops filled by hot matter and relatively dense plasmas start to radiate intensively in soft X-ray continuum and UV/EUV emission lines (Figs. 2.1, 2.2).

- Already reconnected field lines tends to shrink to minimise the free magnetic energy. However, they are frozen in the high-conductive plasmas that is such a way carried out together with them forming the *reconnection jets*.

- The MHD shocks are formed on the jets boundaries with the background plasmas.

Even thought the reconnection-based interpretation of the solar flares naturally unify many effects found on various wavelengths, a lot of questions remains open. Particularly, the problem of a flare triggering – why the magnetic energy quiescently accumulate till to the beginning of flare for a long time is suddenly very rapidly released? Further, there is a really big uncertainty concerning the basic geometry of reconnecting fields and many different models were suggested – see the review by Hudson (`H. Hudson's flare models archive`). Also some quantitative discrepancies in the question of particle acceleration at very short timescales has not been explained yet. To sum up, a lot of both observational as well as theoretical work has to be done to reach satisfactory description on this topic.

1.2.3 Coronal mass ejections

From the observational point of view the coronal mass ejections (CMEs) are very spectacular events when large amount of matter is thrown out of the Sun – see Fig 1.11. This phenomena were discovered relatively recently – not before the space-born solar coronagraphs had started to observe – since such dynamic events hardly could be found during short-lasting total solar eclipses on the Earth.

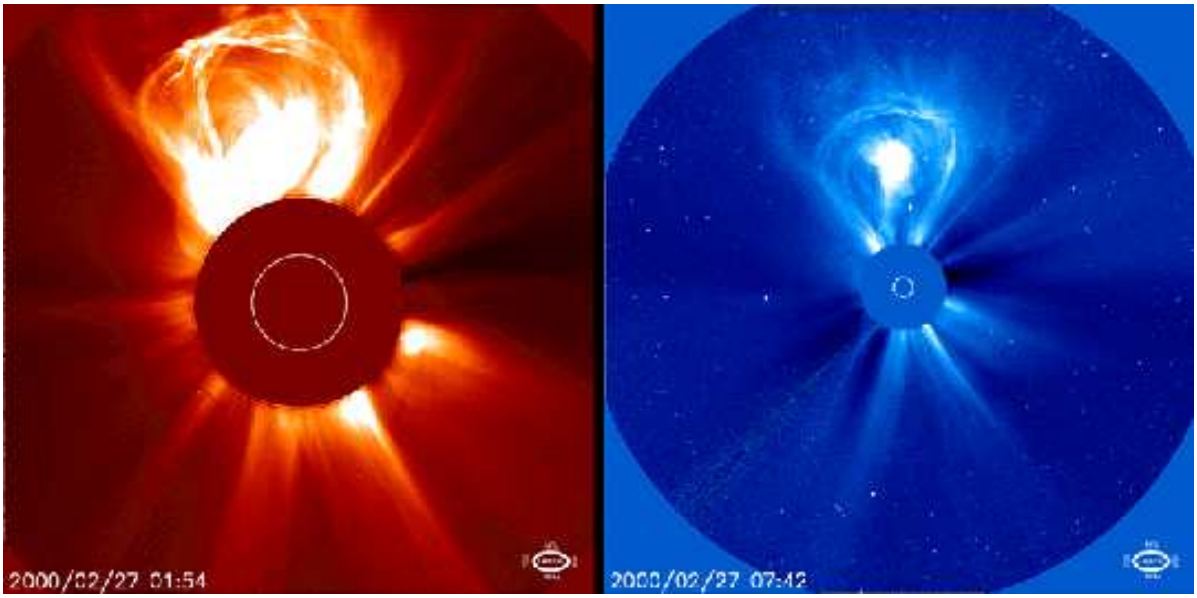

Fig. 1.11: Two subsequent images of coronal mass ejection observed by SOHO/LASCO (`SOHO home webpage`) coronagraphs on 27^{th} February, 2000. The left picture was taken by the *C2* coronagraph at 1:54 UT, the right one by the *C3* at 7:42 UT.

Similarly as solar flares the CMEs are supposed to be driven by sudden simplification of the field configuration accompanied by conversion of magnetic energy – in this case predominantly into the kinetic energy of ejected plasmas. On the other hand, unlike in the case of flares, even the framework, generally acceptable concept of this events is still missing. Formerly suggested models considered the CME as a consequent part of the solar flare as can be seen also on the flare model cartoon (Fig. 1.10), but recent studies (`Schwenn 2002`) seem to preclude this hypothesis.

As a final remark, the great importance of the CMEs as well as the flares for *space weather* applications and solar-terrestrial relations should be noted. Particularly, CMEs represents potentially the most effective source of geomagnetic storms with all their consequences for Earth's atmosphere, biosphere and civilisation.

Chapter 2

Multiwavelenght solar observations

As has been already indicated in the previous chapter the Sun is a star of many faces which it shows depending on the wavelength band and observational technique used. In virtue of this fact complete information about whatever phenomena – and particularly about the active processes – on the Sun hardly could be gained by single instrument and many complementary observations are required. In this chapter a brief review of observational techniques used in the field of solar physics will be given with emphasis to observation of active processes, particularly solar flares. Advantages, limitations and also some peculiarities of each technique are briefly discussed.

Because of nearly common both theoretical as well as observational treatment of the radiation on the moderate and short wavelengths – and also due to role that it plays in the solar flares – it is convenient to discuss quickly this spectral band separately from the 'extremes' – the hard X-rays and radio-waves whose properties will be described afterwards.

2.1 Domain of classical astrophysics – short and moderate wavelengths

Possibilities of the observations in this spectral range are basically given by the fact that optical elements can be generally used for an image formation. It implies rather high spatial resolution reached on these wavelengths.
The theoretical point of view has two coupled aspects: the generation of the radiation and the radiative transfer. It is commonly accepted, that radiation in this spectral range are basically due to thermal emission with only minor effect of non-thermal processes, particularly to polarisation state of the radiated photons. Quantum mechanics is essential in this frequency interval as a large amount of diagnostically important radiation – namely in EUV band – is emitted in spectral lines only.
The situation is complicated by the fact that radiation at these wavelengths is often optically thin. Hence, the information at, say, one pixel of the image does not come from one location at the Sun but is the weighted sum of contributions along whole line of sight. Also the absorption and emission coefficients of the medium sometimes depends on the radiation field and non-LTE approach thus has to be employed. Both these circumstances brings difficulties to interpretation of the data gained using just this spectral band.

2.1.1 Solar activity in the light of the soft X and EUV rays

As was already mentioned, the solar radiation on these wavelengths is basically of thermal origin. Hence the fact, that one observes sometimes very intensive emission of these rather energetic photons indicates by itself the presence of very hot regions in the solar atmosphere. Such hot

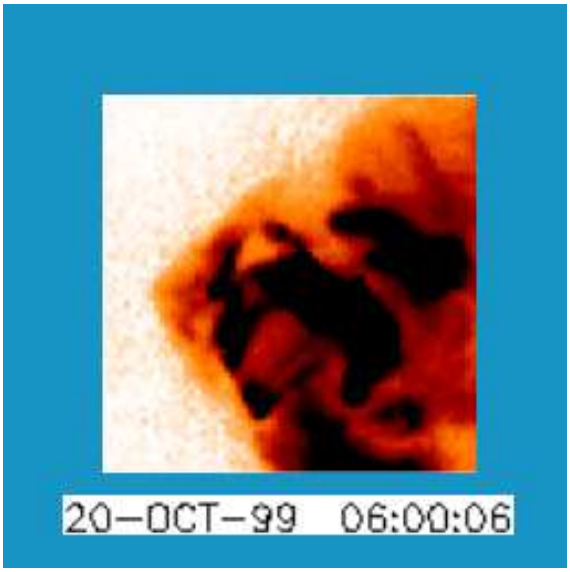

Fig. 2.1: A large solar flare observed in the soft X-rays continuum by the Yohkoh/SXT instrument on 20^{th} October, 1999. The loops arcade formation is clearly visible.

Fig. 2.2: Hot coronal loops observed by the *TRACE* satellite (`TRACE home pages`) in the *Fe* IX line (171 nm). The formation temperature of the line is about 1.3 MK.

and also rather dense – since the intensity of radiation depends also on the *emission measure*[1] – plasma is created particularly during the thermal phase of the solar flare. Hence, the observations in this spectral range provide a useful tool for diagnostics of namely flare and post-flare loops.

There are particularly three observational techniques used within this band: direct imaging in continuum, imaging in specific wavelength (filtergrams) and spectral analysis of radiation. Examples of soft X-ray continuum image of the solar flare and single-wavelength observation of hot coronal loops at the Fe IX line (171 nm) are shown on Figs. 2.1 and 2.2.

2.1.2 The visible Sun

Solar research in the optical wavelengths has due to obvious reasons the most long-lasting history. Early observations of the most obvious manifestations of solar activity at this spectral band – the sunspots – were carried out by Galileo, and even hundreds years before him by old Chinese astronomers.

Currently used observational techniques at these wavelengths involve above all:

White light (continuum) imaging As mentioned above optical continuum originates in the photosphere. Consequently, this technique is used for analysis of photospheric active phenomena. Particularly, studies of sunspots and their dynamics with high spatial as well as temporal resolution are carried out by direct white light imaging.

Monochromatic imaging This technique is based on filtering of integral solar radiation by – usually narrow pass-band – spectral filter. Since specific spectral lines or their components (core, wings) are formed in different layers of the solar atmosphere (see the Fig. 1.2) the monochromatic image of the Sun (or its selected part) shows only the plasma with corresponding physical parameters (namely the temperature).

[1] Emission measure is the volume integral of the square of electron density

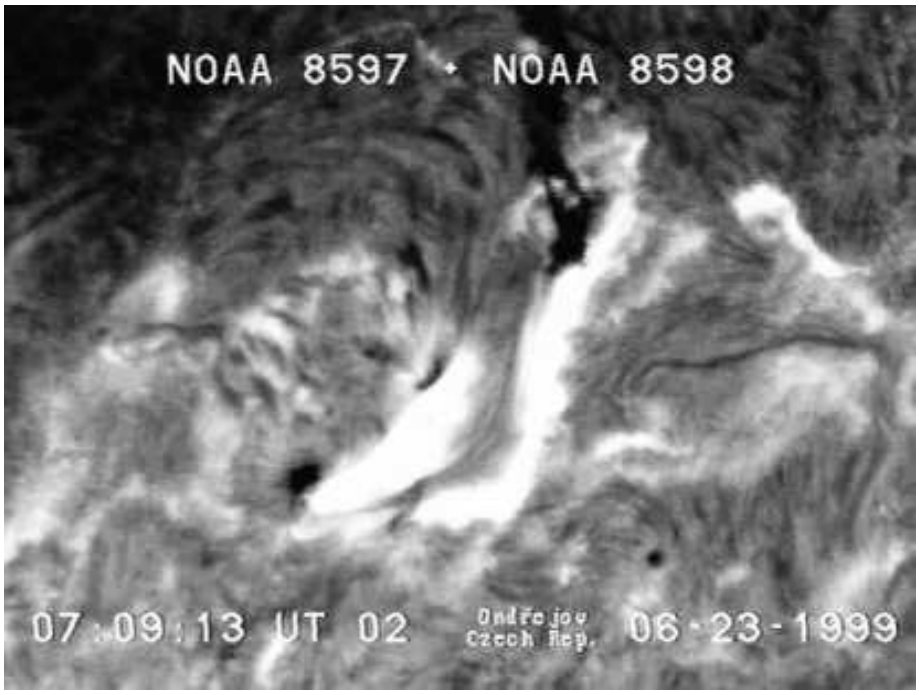

Fig. 2.3: A two-ribbon flare observed in the H_α at the Ondřejov observatory (`Ondřejov Solar Patrol site`) 23^{th} June, 1999.

For solar flare studies are particularly important observations in chromospheric spectral lines. Monochromatic image of the solar flare in the H_α line is shown on the Fig. 2.3.

Spectroscopy Spectral analysis of the solar radiation represents important diagnostic technique. Unlike in the case of the two previously mentioned methods in classical spectroscopy only very narrow region selected on the solar surface by the spectrograph slit is analysed. Hence, much more complete information is available than from monochromatic or continuum observations – but only for the selected one-dimensional area – see the Fig. 2.4. To obtain full information in some region the scanning method is usually employed. It obviously brings limitations for studies of rapidly variable phenomena. This disadvantage was partly overcome using modern techniques such as *MSDP* imaging or quasi-simultaneous filtergrams acquisition on many wavelengths (used by SOHO/MDI).

The shapes of spectral lines are influenced by various physical parameters in the radiation source. Such parameters can be consequently diagnosed using interpretation of observed spectra. Among many at least two quantities should be mentioned:
Doppler shift of spectral line position allows measurements of line-of-sight velocities in the solar atmosphere. It is particularly important for analysis of solar oscillations and waves used in *helioseismology* for solar interior studies. The well known example of solar surface wave generated by particle beam during a flare is shown on dopplergram on the Fig. 2.5.
Another important parameter influencing some spectral lines is the magnetic field. By measurements of Zeeman line splitting the magnetic field strength can be estimated in the radiation source. An example of magnetogram is shown o the Fig. 1.9a.

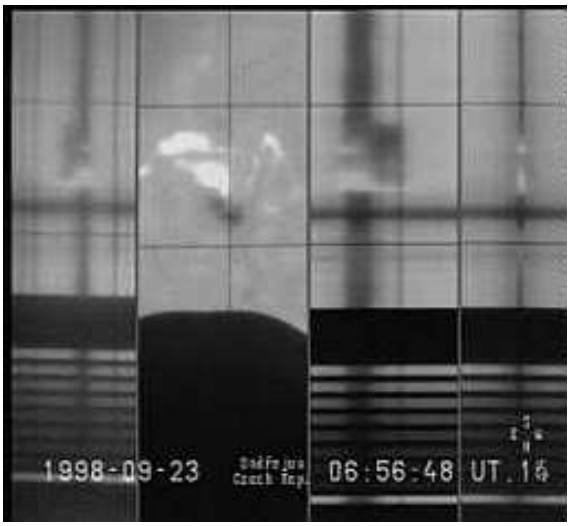

Fig. 2.4: A compound picture (four parts) of the solar flare observed on September 23, 1998 by Multichannel flare spectrograph on the Ondřejov Observatory (`Ondřejov MFS website`). Shown features (left to right): H_β line profile, H_α slit-jaw filtergram, H_α line profile and Ca II (854.2 nm) line profile. The thin vertical line on the H_α image indicates the position of the slit.

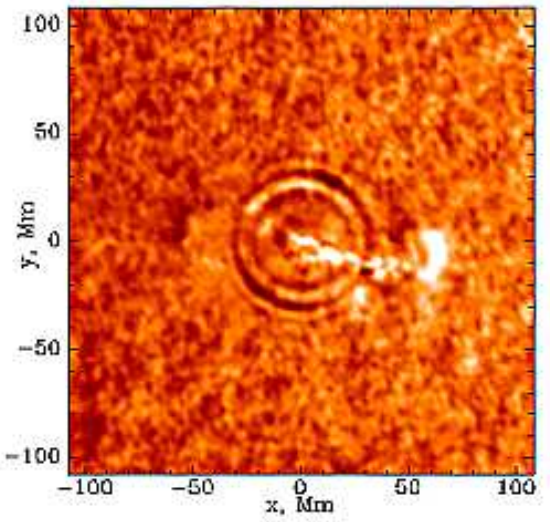

Fig. 2.5: Solar flare observed by SOHO/MDI (`SOHO home webpage`) on July 9, 1996. The present image is the *dopplergram*, hence the velocity field projection to the line of sight is depicted. The surface wave propagating from one of the loop footpoint is clearly visible.

2.2 Extended wavelength range – solar hard X-ray and radio astronomy

Solar research made on the HXR and metric/decimetric radio frequencies differs considerably – at least in two aspects – from the moderate wavelengths observations just discussed above. Firstly, the black-body radiation is too low at these wavelengths for temperatures reached in the solar atmosphere (6000 K – 2 MK) and, hence any significant emission must be of non-thermal origin. This fact predestines the HXR and radio astronomy to be an excellent tool for diagnostics of non-thermal processes going on the Sun. It is important particularly for the solar flare research – as can be clearly seen from the Fig. 2.6 as well as from the theoretical arguments (see the section 1.2.2) the HXR and radio radiation provides unique information about the impulsive phase of the flare.

The second distinction consists in the kind of information provided by observations in, say, classical spectral band and – particularly – by solar radio-spectroscopy. The non-thermal phenomena are usually rapidly variable in radiated spectra over wide range of wavelengths. Simultaneous observations on many frequencies with rather high temporal resolution is therefore desirable. On the other hand, unlike in the case of moderate wavelengths the spatial resolution of HXR and radio observations is low and direct imaging of sources is possible only using some special techniques (see further) involving rather complicated mathematical methods of image acquisition. Frequently detailed broad-band data with high temporal resolution are available but only in the form of the total flux spectral density integrated over whole the Sun.

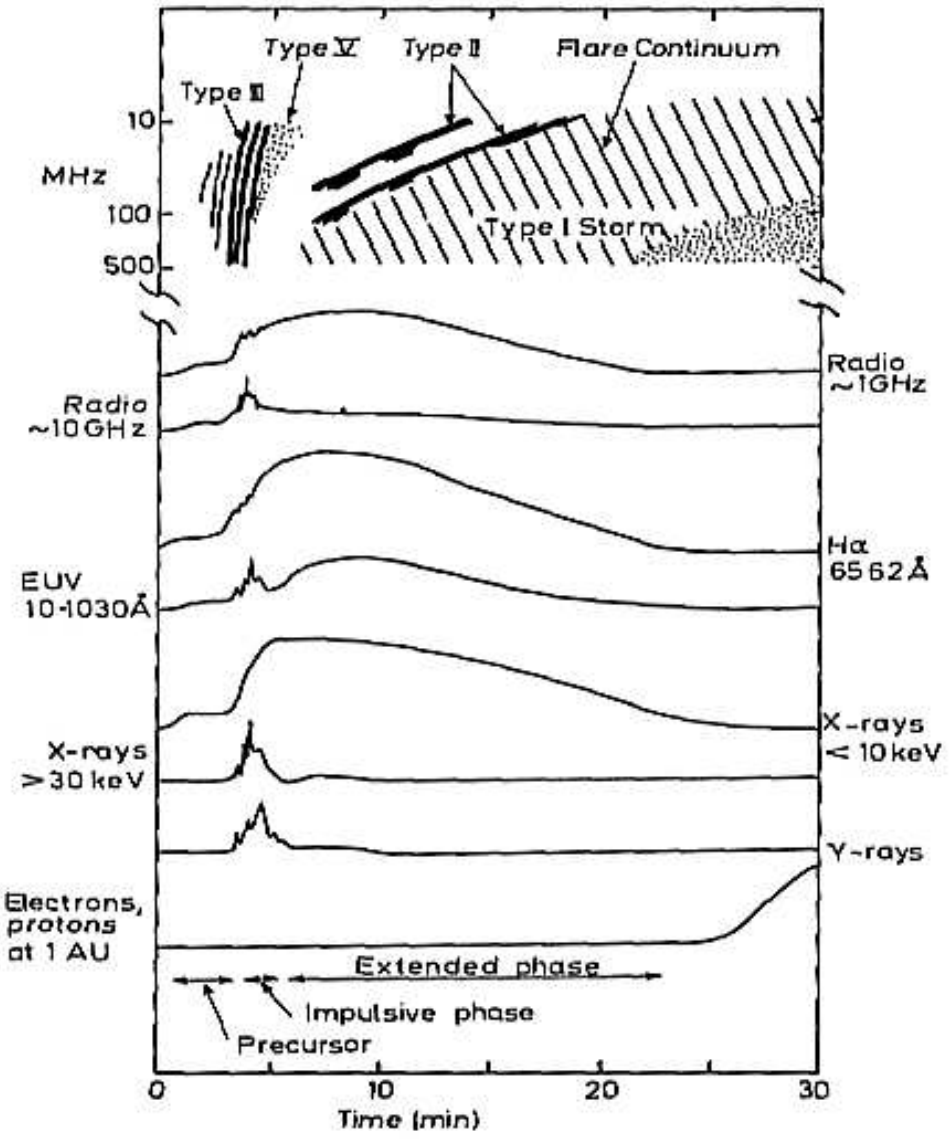

Fig. 2.6: A schematic look on the flare course on various wavelength. Adopted from `Mc Lean & Labrum 1985`.

2.2.1 The Sun on the hard X-rays

Techniques used in this spectral range are of two distinct types: spectral analysis of the spatially-integrated solar HXR flux and, recently introduced direct imaging of solar HXR sources in a given energy channel.

The HXR spectroscopy is – according to the flare frame-work model (section 1.2.2) – important particularly for accelerated particle beams diagnostics. In spite of some ambiguities in the reconstruction of the accelerated particles distribution function from observed spectra some semi-empirical results were obtained. In particular, rather reliable prediction of the proton flares based on the time evolution of the HXR spectra is now available (e.g. `Garcia 1995`). An example of HXR spectroscopic measurement during solar flare is shown on the Fig. 2.7.

The second technique – direct imaging in the HXR – have become available rather recently mainly due to the storm development of computing technology. The use of optical elements for

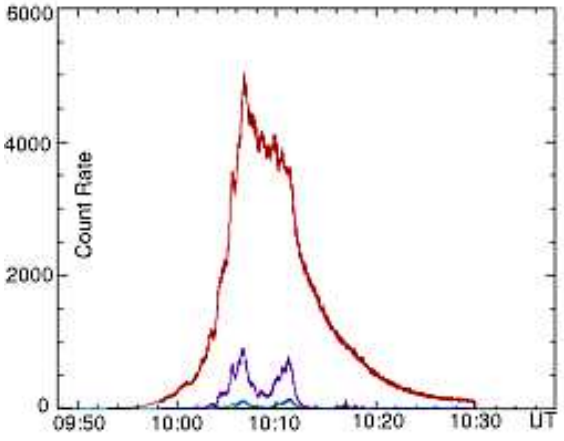

Fig. 2.7: Hard X-ray flux observed in three channels of HXRS spectrograph (`HXRS website`) during March 29, 2001 event.

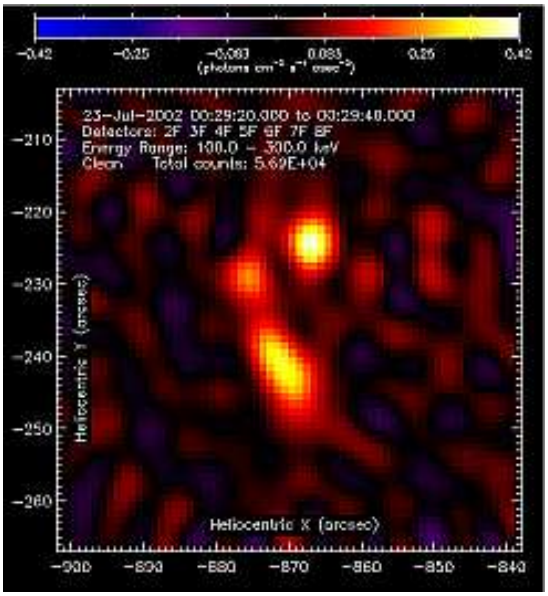

Fig. 2.8: The brightness distribution of the hard X-rays with energies 50 – 100 keV during the impulsive phase of the solar flare observed by *RHESSI* satellite (`RHESSI website`) 25^{th} July, 2002.

imaging is unfortunately impossible on these wavelengths and hence sophisticated mathematical methods of image encoding and subsequent reconstruction have to be employed. The 2-D brightness distribution is firstly encoded to the time series using convolution-like procedure involving the brightness distribution itself and known time-variable pattern. Then, before the analysis the image can be reconstructed using several developed "deconvolution" methods. According to the flare model it is believed, that such imaging technique particularly helps to identify the *flare cores* – points of primary deposit of the particle beam energy. The reconstructed HXR image of the solar flare is shown on the Fig. 2.8.

2.2.2 Solar radiophysics

Solar radiophysics has in some way an exclusive position in the flare research. As was shown, together with the HXR observations it provides unique information about the starting, impulsive phase of the flare, and there are even suggestions of radio manifestation of the basic reconnection process itself.

Somewhat similarly as in the case of spectral lines on moderate wavelengths the non-thermal radio radiation on the given frequency is produced only in the source with corresponding physical parameters. Since the radio emission is usually realised on natural frequencies of radiating plasmas – that are the plasma (ω_p) and cyclotron (ω_B) frequencies (and/or their harmonics) – the radiation on selected wavelength comes from regions of corresponding electron density or magnetic field[2]. These two parameters vary basically with the height in the solar atmosphere, and hence the observation on the given frequency corresponds usually to contribution from radio sources localised in some atmospheric layer. This fact implies another advantage of the radio observations – the decimetric and metric radio waves cover whole the solar corona, where the basic reconnection process is supposed to be localised (see the section 1.2.2).

[2]For optical, UV and EUV emission the most determining parameter is the temperature, on the other hand

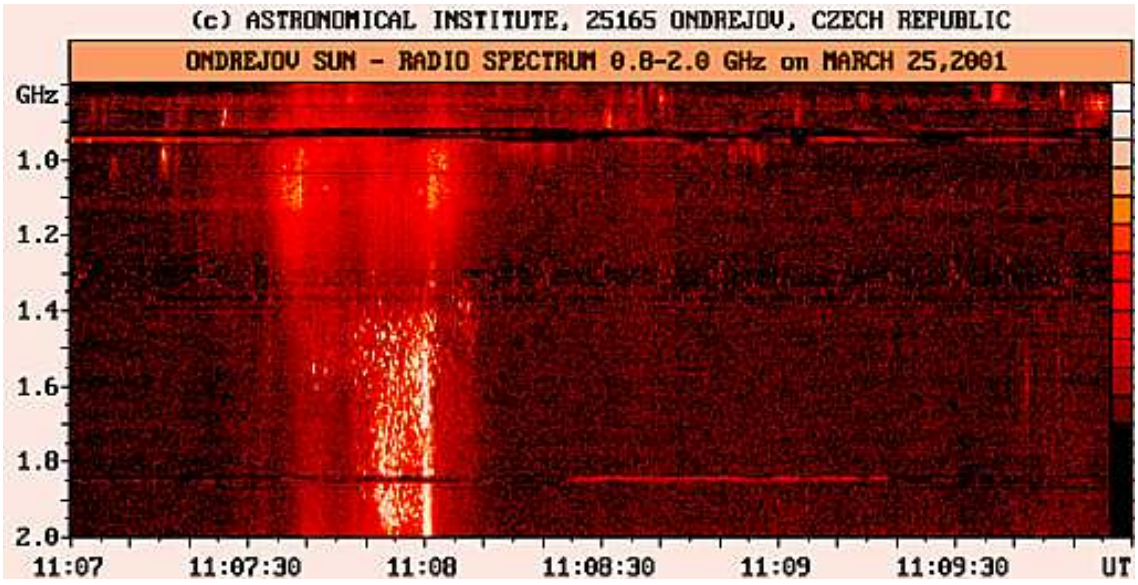

Fig. 2.9: A typical dynamic radio spectrogram on the decimetric wavelength. Fine structures as well as broad-band emission is present. The spectrum was recorded by the Ondřejov radiospectrograph *RT 5* (`Ondřejov solar radiodata webpage`).

Similarly as in the case of the HXR observations two kinds of techniques are used: analysis of various properties of spatially-integrated radio flux and radio imaging at given wavelength. Both will be briefly described now.

2.2.2.1 Radiometry, radio-spectroscopy and spectro-polarimetry

Very early method used to solar radio observations is the *radiometry* – measurement of solar radio flux spectral density at given frequency. Unfortunately, because of mentioned usual rapid spectral variability of non-thermal sources it provides rather incomplete information. Nevertheless, very high temporal resolution can be reached using this technique and thus it remains valuable as an auxiliary method to the other radio observations.

The disadvantage of 'escape' of radio emission outside the scope of one recorded frequency channel encountered in the radiometric method was naturally overcome introducing spectral density measurement on multiple closely spaced frequencies. It is the principle of the *radio-spectroscopy*, probably the most fruitful method used in the solar radioastronomy up today. Interpretation of the time evolution of radiated spectrum may provide useful diagnostic tools for analysis of plasma parameters in known or supposed processes in the flare, or it may even lead to discoveries of till unexpected phenomena. In such a way the explanation of type III and type II radio spectra has started a new period in the flare research extending observed flaring activity outside the chromosphere. The interpretation of the dynamic radio spectra and its applications represent the contents of the Chapter 4.

An example of the dynamic spectrum observed in the decimetric range at the Ondřejov Observatory is shown on the Fig. 2.9. The instantaneous spectrum (flux density distribution) at given time is obtained by vertical slice in the frequency-time plane, the time evolves from left to right. The value of flux spectral density at given time and frequency is expressed by brightness scale, as usual.

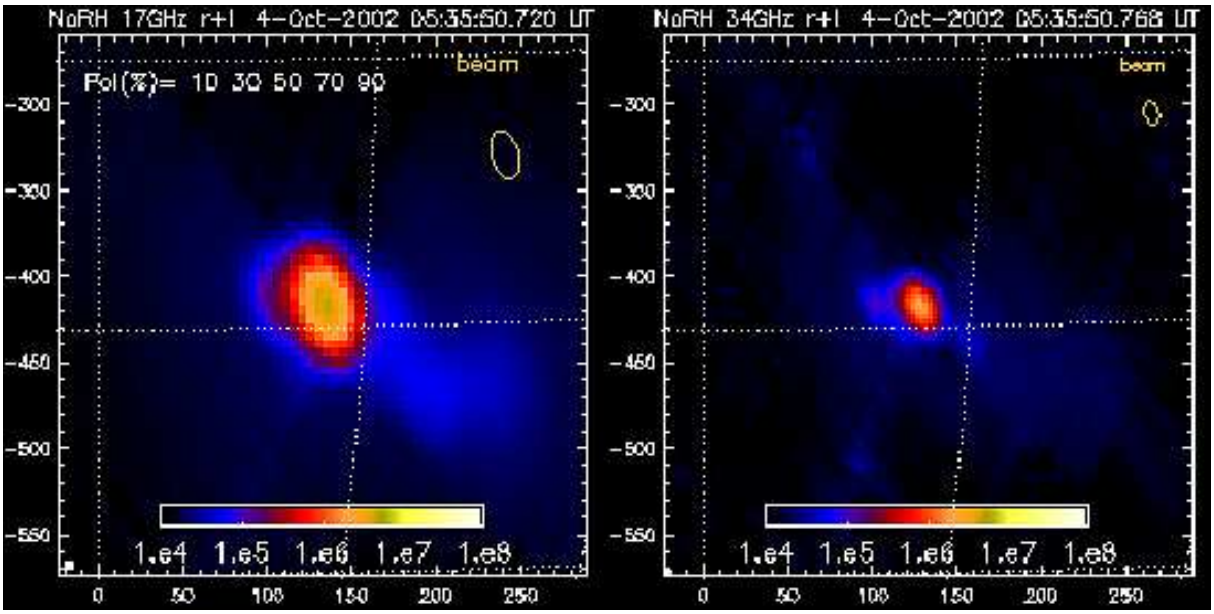

Fig. 2.10: Solar flare observed by the Nobeyama radioheliograph (`NoRH home webpage`) on October 4, 2002. The intensity maps for 17 GHz (left) and 34 GHz (right) frequencies are depicted. The small yellow circle in the upper-right corner indicates the radioheliograph spatial resolution.

Some extension to the radio-spectroscopy represents the *radio spectro-polarimetry*. The radio flux density is recorded as in the radiospectrograph (quasi-)simultaneously on multiple wavelengths, but independently for both left- and right-hand side polarisations. It can bring supplementary information about the radio source itself as well as about the atmospheric inter-layers between the source and the observer.

2.2.2.2 Brightness distribution measurement

As in the case of HXR radiation the spatial resolution of radio-wave observations are low using single receiver only. Hence, some interferometric technique has to be employed to reconstruct the solar radio images. Currently two methods are used for radio brightness distribution measurements (*radioheliography*):

Radioheliograph with scanning beam. Such device is usually constructed as an sparse equidistantly spaced aerial array. The principle is somewhat similar to the optical grating used in spectroscopy: in a given frequency this system would emit radiation into the angular pattern whose dominant part is very narrow central beam. According to reversal theorem known from radio-technique only the radiation coming from the direction of that beam is received. Introducing the phase shifts progressively with the aerial distance in the array the beam can scan across the source. Such a way 2-D brightness distribution is encoded into the time series and the radio image of the Sun is to be subsequently reconstructed. The obvious disadvantage is rather low temporal resolution due to necessity of scanning.

Correlator radioheliograph The correlator method is based on the fact, that instantaneous product of two aerial currents represents (under some plausible conditions) one Fourier component of the brightness distribution. Each aerial pair with independent baseline position vector thus contributes by corresponding component. Image reconstruction is then made simply by inverse Fourier transform. Despite the fact, that this principle is known for a quite long time only the development of fast computing technology has enabled its use in practise recently.

An example of radio image of the solar flare on two frequencies (17 GHz and 34 GHz) is shown in Fig. 2.10. The main limitation of this kind of observation consists, again, in the usual 'escape' of the source from the frequency scope of the device used. This draw-back will perhaps be overcome by the proposed radio telescope of new generation briefly described now.

2.2.2.3 The future

It is obvious, that one has two kinds of incomplete information from the contemporary solar radio observations:

1. Detailed spectral and polarisation measurements of the solar radio flux with high temporal resolution. No positional information about the sources is available, on the other hand.

2. Quite sufficiently resolved brightness distribution measurements, unfortunately in the single frequency only.

As the correlator radiotelescopes have become available, the most natural solution of this unsatisfying state is to extend their observation to multiple frequencies – just to combine the radio spectrograph (or spectropolarimeter) capabilities with the radioheliograph spatial resolution. And really, such device – the Frequency-Agile Solar Radiotelescope (FASR; see `FASR home webpage`) – was already proposed! Its parameters in the decimetric range are very promising: frequency resolution about 1%, image acquisition time on all frequency channels about 0.1 s and spatial resolution 10 arc-sec on the frequency of 2 GHz. The supposed date of observations start is at 2008. It is clear, that whole the solar flare research community may look forward to this revolutionary equipment.

Chapter 3

Elementary radio emission processes in the solar corona

The theory of elementary radiative processes plays a key role in determination of relations between observed data and local parameters in the source everywhere the electromagnetic radiation is used for distant diagnostics of matter. In case of radiation of coronal plasmas on radio-wave frequencies particularly three basic mechanisms are important:

- free-free thermal emission (bremsstrahlung),
- gyro-synchrotron radiation, and
- plasma emission — the process specific especially for the solar corona.

Since all these processes are closely related to properties of waves in plasmas, the elemental theory of plasma wave modes is good starting point before discussing each emission mechanism in particular.

A large amount of literature can be found on this topic – the comprehensive monograph by Melrose (1980) is roughly followed through this chapter.

3.1 Waves in plasmas

It is well known fact that in plasmas (particularly in magnetised one) a couple of wave modes can exist. This broad variety is due to a high complexity of the plasma response to electric or magnetic field perturbations. The electric ($\mathbf{E}$) and magnetic ($\mathbf{B}$) fields in plasmas are described by the system of Maxwell equations:

$$\begin{aligned} \text{rot } \mathbf{E} &= -\frac{\partial \mathbf{B}}{\partial t} \qquad \text{div } \mathbf{E} = \frac{1}{\varepsilon_0}\rho \\ \text{rot } \mathbf{B} &= \mu_0 \mathbf{j} + \frac{1}{c^2}\frac{\partial \mathbf{E}}{\partial t} \qquad \text{div } \mathbf{B} = 0 \end{aligned} \tag{3.1}$$

with $\mathbf{j}$ being the electric current density and ρ the charge density. These two quantities satisfy the charge continuity equation

$$\frac{\partial \rho}{\partial t} + \text{div } \mathbf{j} = 0, \tag{3.2}$$

what implies directly from the set (3.1). For the purpose of formal theory of waves it is convenient to express Maxwell equations in natural basis of harmonic functions. Thus Fourier transforming

the set (3.1) one obtains:

$$\mathbf{k} \times \mathbf{E} = \omega \mathbf{B} \tag{3.3}$$

$$\mathbf{k} \times \mathbf{B} = -i\mu_0 j - \frac{\omega}{c^2} \cdot \mathbf{E} \tag{3.4}$$

$$\mathbf{k} \cdot \mathbf{E} = -\frac{i}{\varepsilon_0}\rho \tag{3.5}$$

$$\mathbf{k} \cdot \mathbf{B} = 0. \tag{3.6}$$

It is clear that the equation (3.6) is redundant since it follows directly from eq. (3.3), but with one exception – in the case of $\omega = 0$, i.e. in the case of static fields, the reduction of the system of equations does not apply. Thus, static fields have to be treated explicitly in further considerations. This is closely related to the well known problem of the fourth Maxwell equation (div $\mathbf{B} = 0$), which should be considered as the initial condition rather than independent relation.

From the set of three remaining equations the final wave equation in the form

$$\mathbf{k} \times (\mathbf{k} \times \mathbf{E}(\mathbf{k}, \omega)) + \frac{\omega^2}{c^2}\mathbf{E}(\mathbf{k}, \omega) = -i\omega\mu_0 \mathbf{j}(\mathbf{k}, \omega) \tag{3.7}$$

can be expressed, where equations (3.3) and

$$\omega\rho(\mathbf{k}, \omega) = \mathbf{k} \cdot \mathbf{j}(\mathbf{k}, \omega),$$

which is just the Fourier transform of continuity equation (3.2), should be considered as definitions of auxiliary quantities $\mathbf{B}$ and ρ in terms of basic quantities $\mathbf{E}$ and $\mathbf{j}$, respectively.

The current density $\mathbf{j}$ consists of two parts:

1. the current caused by induced motion of particles in plasmas under influence of electromagnetic field $\mathbf{j}^{ind}$
2. the extraneous current $\mathbf{j}^{ext}$

In the first approximation the induced part of current is linearly related to electric filed according to generalised Ohms law (in usual tensor notation):

$$j_i^{ind}(\mathbf{k}, \omega) = \sigma_{ij}(\mathbf{k}, \omega) \cdot E_j(\mathbf{k}, \omega) \tag{3.8}$$

where $\sigma_{ij}(\mathbf{k}, \omega)$ is the generalised conductivity tensor and usual Einsteins summation law was applied. For the formal purposes it is much more convenient to use another tensor describing the linear plasma response to electric field perturbation. The dielectric tensor $\varepsilon_{ij}(\mathbf{k}, \omega)$ is defined as:

$$\varepsilon_{ij}(\mathbf{k}, \omega) \equiv \delta_{ij} + \frac{i}{\omega\varepsilon_0} \cdot \sigma_{ij}(\mathbf{k}, \omega) \tag{3.9}$$

with δ_{ij} being the Kronecker delta (the unit tensor) and ε_0 the vacuum permittivity constant. Separating the current density into induced and extraneous parts and using Ohms law (3.8) and dielectric tensor definition (3.9) the wave equation (3.7) is re-expressed in the form:

$$\Lambda_{ij}(\mathbf{k}, \omega) \cdot E_j(\mathbf{k}, \omega) = -\frac{i}{\omega\varepsilon_0} j_i^{ext}(\mathbf{k}, \omega) \tag{3.10}$$

where the dispersion tensor $\Lambda_{ij}(\mathbf{k}, \omega)$ is defined as

$$\Lambda_{ij}(\mathbf{k}, \omega) \equiv \frac{k^2 c^2}{\omega^2}\left(\frac{k_i k_j}{k^2} - \delta_{ij}\right) + \varepsilon_{ij}(\mathbf{k}, \omega). \tag{3.11}$$

The equation (3.10) represents a set of three linear equations with components of the extraneous current density $\mathbf{j}^{ext}(\mathbf{k},\omega)$ as explicit source terms.

Except of this explicit source term there is also an implicit one hidden in the dielectric tensor. The dielectric tensor can be separated into two parts – hermitian and anti-hermitian whose describes different kinds of plasma response to electric field perturbation. While the hermitian part of $\varepsilon_{ij}(\mathbf{k},\omega)$ describes time-reversible component of response[1], the anti-hermitian part causes changes of the wave energy, either positive or negative, representing such a way the effective source of waves. In case of energy decrease the damping of waves occurs, the energy increase means amplification (or negative damping/absorption) of waves.

3.1.1 The general dispersion equation of linear waves

The question arises up what is behaviour of the electric field perturbation in source-free case. Thus, one has to solve homogeneous form of the equation (3.10) with also implicit source term omitted, i.e.

$$\Lambda^h_{ij}(\mathbf{k},\omega)\cdot E_j(\mathbf{k},\omega)=0, \tag{3.12}$$

where $\Lambda^h_{ij}(\mathbf{k},\omega)$ is the hermitian part of the dispersion tensor. Solution of such a system of equations exist only if the relation

$$\Lambda(\mathbf{k},\omega)\equiv \det\Lambda^h_{ij}(\mathbf{k},\omega)=0 \tag{3.13}$$

is fulfilled. The condition (3.13) represents the general dispersion equation for linear non-damped waves in plasmas. To rewrite it to the usual form of the dispersion relation for a specific wave mode one has to express the frequency ω as a function of the wave vector $\mathbf{k}$. This is not unique operation in general however, and many branches

$$\omega^m=\omega^m(\mathbf{k}) \tag{3.14}$$

can be obtained. Each branch $\omega^m(\mathbf{k})$ represents one wave mode m.

Polarisation vectors Inserting relation (3.14) into the homogeneous equation (3.12) a solution for specific wave mode can be found. According to known rules of linear algebra the vector that solves (3.12) has to be the eigen-vector corresponding to the zero eigen-value of the tensor

$$\Lambda^h_{ij}(\mathbf{k})=\Lambda^h_{ij}\left(\mathbf{k},\omega^m(\mathbf{k})\right).$$

Such an eigen-vector is not determined uniquely since its complex amplitude is arbitrary. Therefore it is convenient to choose an unimodular complex vector $\mathbf{e}^m(\mathbf{k})$ as a representative of all solutions of the equation (3.12) for given wave mode. Such vector is called the polarisation vector and besides the dispersion relation (3.14) it is one of the basic characteristics of the specific wave mode[2].

Specific wave modes As an illustration of determination of particular wave mode and its characteristics from the general dispersion equation (3.13) one may choose well known Langmuir, transverse and ion-sound waves in plasmas without ambient magnetic field. The first thing has

[1] The corresponding part of conductivity tensor is anti-hermitian, and thus the time averaged power emitted or absorbed by plasmas $\langle \mathbf{E}\cdot\mathbf{j}\rangle$ is zero

[2] In case of two eigen-values are zeroed simultaneously one obtains two-dimensional space of solutions and the concept of polarisation vector has to be replaced introducing polarisation tensor instead (see `Melrose 1980`)

to be done is calculation of the dielectric tensor. The kinetic approach gives for unmagnetised plasmas following result (according to `Melrose 1980`):

$$\varepsilon_{ij}(\mathbf{k},\omega) = \delta_{ij} + \sum_{\alpha} \frac{q_\alpha^2}{\varepsilon_0 \omega^2} \int \frac{(\omega - \mathbf{k}\cdot\mathbf{v})\delta_{sj} + k_s v_j}{\omega - \mathbf{k}\cdot\mathbf{v} + iO} \cdot v_i \cdot \frac{\partial f_\alpha(\mathbf{p})}{\partial p_s}\ \mathrm{d}^3\mathbf{p}, \tag{3.15}$$

the sum is performed over each particle species α and small imaginary part in the denominator indicates that correct integration path according to Landau prescription has to be used. For isotropic medium the dielectric tensor can be separated into longitudinal(ε^l) and transversal (ε^t) parts as:

$$\varepsilon_{ij}(\mathbf{k},\omega) = \varepsilon^l(k,\omega)\cdot\frac{k_i k_j}{k^2} + \varepsilon^t(k,\omega)\left(\delta_{ij} - \frac{k_i k_j}{k^2}\right) \tag{3.16}$$

and explicit calculation for Maxwellian distribution function gives:

$$\begin{aligned} \varepsilon^l(k,\omega) &= 1 + \sum_{\alpha} \frac{1}{k^2\lambda_{D\alpha}^2}\left[1 - \phi(y_\alpha) + i\sqrt{\pi}y_\alpha \exp(-y_\alpha^2)\right] \\ \varepsilon^t(k,\omega) &= 1 + \sum_{\alpha} \frac{\omega_{p\alpha}^2}{\omega^2}\left[1 - \phi(y_\alpha) + i\sqrt{\pi}y_\alpha \exp(-y_\alpha^2)\right]. \end{aligned} \tag{3.17}$$

Here, $\omega_{p\alpha}$ and $\lambda_{D\alpha}$ are appropriate plasma frequencies and Debye lengths, respectively:

$$\omega_{p\alpha}^2 \equiv \frac{n_\alpha q_\alpha^2}{m_\alpha \varepsilon_0}, \qquad \lambda_{D\alpha} \equiv \frac{V_\alpha}{\omega_{p\alpha}}, \tag{3.18}$$

and the following abbreviations ($V_\alpha \equiv k_B T/m_\alpha$ designates thermal velocity of particles of species α) were used:

$$\phi(y) \equiv 2y\exp(-y^2)\int_0^y \exp(t^2)\mathrm{dt}, \qquad \mathrm{y}_\alpha \equiv \frac{\omega}{\sqrt{2}\mathrm{k}\mathrm{V}_\alpha}.$$

Inserting the hermitian part of the dielectric tensor (i.e. retaining real parts of longitudinal and transversal components only) in the form of (3.16) into the equation (3.12) the equation

$$\left(\mathrm{Re}\left\{\varepsilon^l(k,\omega)\right\}\right)\cdot\left(n^2 - \mathrm{Re}\left\{\varepsilon^t(k,\omega)\right\}\right)^2 = 0 \tag{3.19}$$

is obtained with the refractive index n defined as

$$n \equiv \frac{ck}{\omega}.$$

The anti-hermitian part not considered for present purposes will be taken into account later in the section 3.1.2, paragraph **Absorption coefficient**.

Now, expanding the function $\phi(y)$ into series for the high-frequency limit ($y \gg 1$) and retaining only first few terms of electronic contribution to this function (the contribution of ions is reduced by factor of m_e/m_i relatively to that of electrons) the transversal part of the equation (3.19) becomes

$$n^2 = 1 - \frac{\omega_{pe}^2}{\omega^2}$$

or using the refractive index definition written in more familiar form

$$\omega^2(k) = \omega_{pe}^2 + c^2k^2. \tag{3.20}$$

The just derived equation (3.20) represents the dispersion equation for transversal (electromagnetic) mode.

The longitudinal part of eq. (3.19) gives two wave modes depending on the frequency limit used. For $\omega \gg kV_e$, i.e. $y_e \gg 1$ the expansion of the function ϕ yields dispersion equation

$$\omega^2(k) = \omega_{pe}^2 + 3k^2V_e^2 \tag{3.21}$$

which describes well known Langmuir waves.
On the other hand, expanding formulae for longitudinal part of the dielectric tensor in the limit

$$kV_i \ll \omega \ll kV_e$$

the ion-sound mode with the dispersion equation

$$\omega^2(k) = \frac{k^2c_s^2}{1 + k^2\lambda_{De}^2} \tag{3.22}$$

is found. Here, the ion-sound wave speed c_s is defined by

$$c_s \equiv \omega_{pi} \cdot \lambda_{De}.$$

3.1.2 Energetics in the waves

The electric perturbation in plasma waves induces also the perturbation of magnetic field and, due to medium response, also variations of plasma velocity, stresses and pressure. All these perturbations raise the total amount of energy contained in plasmas and the difference over the equilibrium state can be ascribed to the waves. It is straightforward to compute the electric or magnetic field energy in waves knowing the electric field amplitude. On the other hand, mechanical energy connected with plasma motions and stresses is hard to be identified in general. Nevertheless, the total amount of energy contained in particular wave mode can be, fortunately, related to the electric field energy in this mode independently. Generally speaking, it is done rewriting the dispersion equation

$$\det\Lambda_{ij}(\mathbf{k}, \omega) = 0 \tag{3.23}$$

generalised to the case of weakly damped or growing waves (the anti-hermitian part of the dielectric tensor is included now) into the form of the energy conservation law (for details see `Melrose 1980`). The explicit calculations gives for the ratio R_E^m between the total phase energy density[3] $w^m(\mathbf{k})$ and the phase energy density of the electric field $w_E^m(\mathbf{k})$ in the mode m following expression:

$$R_E^m(\mathbf{k}) \equiv \frac{w_E^m(\mathbf{k})}{w^m(\mathbf{k})} = \left(\frac{1}{\omega}\frac{\partial}{\partial\omega}\left[\omega^2\varepsilon^m(\mathbf{k},\omega)\right]\right)^{-1}_{\omega=\omega^m(\mathbf{k})}, \tag{3.24}$$

where $\varepsilon^m(\mathbf{k}, \omega)$ is abbreviation for

$$\varepsilon^m(\mathbf{k}, \omega) \equiv \overline{e_i^m}(\mathbf{k})e_j^m(\mathbf{k})\varepsilon_{ij}^h(\mathbf{k}, \omega)$$

and the electric field (phase) energy density reads:

$$w_E^m(\mathbf{k}) = \frac{\varepsilon_0|\mathbf{E}^m(\mathbf{k})|^2}{2} \cdot \frac{(2\pi)^3}{V}. \tag{3.25}$$

[3]Phase energy density is the energy of wave mode m contained in elemental volume of phase space – i.e. energy per unit volume and unit cube of $\mathbf{k}$-space

Energy radiated by extraneous current The extraneous current on the R.H. side of the expression (3.10) represents a source term in the wave equation. The wave energy U radiated (or absorbed) by this source is given by the work of the extraneous current against the consistent electric field of the wave, i.e.:

$$U = -\int_{-\infty}^{+\infty}\int_{V}\mathbf{j}^{ext}(\mathbf{r},t)\cdot\mathbf{E}(\mathbf{r},t)\ \mathrm{d}^3\mathbf{r}\ \mathrm{d}t = \tag{3.26}$$

$$= -\int_{-\infty}^{+\infty}\int \mathrm{Re}\left\{\mathbf{j}^{ext}(\mathbf{k},\omega)\cdot\mathbf{E}(\mathbf{k},\omega)\right\}\frac{\mathrm{d}^3\mathbf{k}}{(2\pi)^3}\frac{\mathrm{d}\omega}{2\pi},$$

where the Parcevals power theorem was used. Solution of the wave equation (3.10) can be expressed as

$$E_i(\mathbf{k},\omega) = -\frac{i}{\omega\varepsilon_0}\Lambda_{ik}^{-1}(\mathbf{k},\omega)\cdot j_k^{ext}(\mathbf{k},\omega), \tag{3.27}$$

where the matrix $\Lambda_{ik}^{-1}(\mathbf{k},\omega)$ is the inversion operator to the dispersion tensor (3.11) and according to the tensor algebra rules it is written down using its co-factors (sub-determinants of transposed matrix) λ_{ik} as:

$$\Lambda_{ik}^{-1}(\mathbf{k},\omega) = \frac{\lambda_{ik}(\mathbf{k},\omega)}{\Lambda(\mathbf{k},\omega)}.$$

Now, inserting the particular solution (3.27) into the formula (3.26), the wave energy generated by the extraneous current density $\mathbf{j}^{ext}$ can be computed. Contributions to integral over ω are zero with exceptions of the poles of function in integrand. Such residues have to be treated carefully, and the integration has to be performed over the path in the complex plane according to Landau prescription. Each residue is connected with one zero of $\Lambda(\mathbf{k},\omega)$, and thus each pole represents the energy radiated in one specific wave mode. Explicit calculation gives for energy radiated by extraneous current in wave mode m the expression:

$$U^m = \int \frac{R_E^m(\mathbf{k})}{\varepsilon_0}\left|\overline{\mathbf{e}^m}(\mathbf{k})\cdot\mathbf{j}^{ext}\left(\mathbf{k},\omega^m(\mathbf{k})\right)\right|^2\frac{\mathrm{d}^3\mathbf{k}}{(2\pi)^3},$$

where the bar over the polarisation vector $\mathbf{e}^m(\mathbf{k})$ means complex conjugation as usual. Apparently, the quantity

$$u^m(\mathbf{k}) = \frac{R_E^m(\mathbf{k})}{\varepsilon_0}\left|\overline{\mathbf{e}^m}(\mathbf{k})\cdot\mathbf{j}^{ext}\left(\mathbf{k},\omega^m(\mathbf{k})\right)\right|^2 \tag{3.28}$$

that represents the wave energy generated by current density $\mathbf{j}^{ext}\left(\mathbf{k},\omega^m(\mathbf{k})\right)$ in the mode m per unit cube of k-space, or its time derivative – the radiated power

$$p^m(\mathbf{k}) = \frac{\mathrm{d}u^m(\mathbf{k})}{\mathrm{d}t} \tag{3.29}$$

will be more relevant ones for computation of radiation in particular emission processes, as described in the following section (3.2).

Absorption coefficient The advantage of approach used above allows one to involve also absorption of waves consistently. It can be easily done identifying the extraneous current with the implicit source term caused by anti-hermitian part $\varepsilon_{ij}^a(\mathbf{k},\omega)$ of the dielectric tensor, i.e.:

$$j_i^{ext}(\mathbf{k},\omega) = -i\varepsilon_0\omega\ \varepsilon_{ij}^a(\mathbf{k},\omega)E_j(\mathbf{k},\omega). \tag{3.30}$$

Now, the absorption coefficient

$$\gamma^m(\mathbf{k}) \equiv -\frac{1}{w^m(\mathbf{k})}\ \frac{\mathrm{d}w^m(\mathbf{k})}{\mathrm{d}t} = -\frac{1}{Vw^m(\mathbf{k})}\ \frac{\mathrm{d}u^m(\mathbf{k})}{\mathrm{d}t} \tag{3.31}$$

is computed inserting the current density (3.30) into the relation (3.28). The final result is as follows:

$$\gamma^m(\mathbf{k}) = -2i\omega^m(\mathbf{k})R_E^m(\mathbf{k})\overline{e_i^m}(\mathbf{k})e_j^m(\mathbf{k})\varepsilon_{ij}^a(\mathbf{k},\omega^m(\mathbf{k})). \tag{3.32}$$

The absorption coefficient $\gamma^m(\mathbf{k})$ may reach both positive and negative values depending on the anti-hermitian part $\varepsilon_{ij}^a(\mathbf{k},\omega)$ of the dielectric tensor. Negative values then correspond to self-generation of waves. If the anti-hermitian part $\varepsilon_{ij}^a(\mathbf{k},\omega)$ is identified with that for Maxwellian plasmas expressed by eq. (3.17) the absorption coefficient is positive and corresponding wave energy decrease is known as Landau damping.

When some wave mode experiences absorption (either positive or negative) its frequency $\omega^m(\mathbf{k})$ becomes a complex quantity what reflects changes in wave amplitude. Thus, relation between the imaginary part of frequency $\omega^m(\mathbf{k})$ and the corresponding absorption coefficient defined by eq. (3.31) should be found. Since the electric field amplitude in the wave evolves as $\mathbf{E}(\mathbf{k},t) \propto \exp[-i\omega(\mathbf{k})t]$ and $w(\mathbf{k}) \propto E^2(\mathbf{k})$ these two quantities are related simply as

$$\gamma^m(\mathbf{k}) = -2\mathrm{Im}\{\omega^m(\mathbf{k})\} \tag{3.33}$$

3.2 Specific emission mechanisms

Now, when the general theory of propagation and generation of the waves in plasmas has been reviewed, the extraneous current density and its Fourier transform has to be identified for each specific emission mechanism to calculate the energy or power radiated according to the formula (3.28).

3.2.1 Bremsstrahlung and gyro-synchrotron radiation

It is well known fact from the theory of electromagnetic field that whenever the charged particle changes the vector of its velocity the electromagnetic radiation is emitted. There are two natural kinds of such an accelerated particle motion in plasmas implying two basic emission mechanisms:

1. non-rectilinear motion of electron in the electric field of ion during electron-ion encounters in thermal plasmas – resulting radiation is called bremsstrahlung or free-free emission,

2. spiralling motion of particles (especially electrons) in the magnetic field imposed to plasmas – gyro-radiation or synchrotron radiation is the proper assignation for this radiative process in dependence on the spiralling particle energy (medium or relativistic).

Both emission processes will be now discussed further.

3.2.1.1 Bremsstrahlung

The relevant quantity that is to be found is the power $P(\omega)$ radiated in the electromagnetic mode in unit volume of plasmas per unit frequency interval. To compute this quantity one may to start with determining the energy radiated by single electron during one encounter with single ion, then calculate the power radiated by the electron during multiple (continuous) encounters with ions taking into account the encounter frequency, and finally sum over the electron distribution function.

The energy radiated during single encounter can be found from the equation (3.28) identifying the extraneous current density with that of one moving electron. If the trajectory of the electron

$$\mathbf{r} = \mathbf{r}(t)$$

is determined, the current density connected with this moving (point) charge can be expressed as

$$\mathbf{j}(\mathbf{r},t) = -e\mathbf{v}(t)\delta\left(\mathbf{r}-\mathbf{r}(t)\right)$$

and its Fourier transform is

$$\mathbf{j}(\mathbf{k},\omega) = -e\int_{-\infty}^{+\infty}\mathbf{v}(t)\exp\left[-i\left(\mathbf{k}\cdot\mathbf{r}(t)-\omega t\right)\right]\mathrm{dt}. \tag{3.34}$$

Here, $\mathbf{v}(t) = \dot{\mathbf{r}}(t)$ is the electron instantaneous velocity and $\delta(x)$ is the Dirac delta function. For the electromagnetic mode with the refractive index

$$n(\omega) \equiv \frac{ck}{\omega} \geq 1$$

in isotropic thermal plasmas (see eq. 3.20) and the non-relativistic particle ($v(t) \ll c$) the variation of the term $\mathbf{k}\cdot\mathbf{r}(t)$ is negligible comparing to the second expression ωt in the exponent. Thus, the space-dependent term contribute only by constant factor of complex unity (which can be omitted) to the Fourier transform of the extraneous current. This approximation corresponds to omitting the internal retardation inside the source in classical electromagnetic field theory (dipole approximation). Retaining the time-dependent term only in the exponent one can find for the extraneous current caused by single particle the following expression:

$$\mathbf{j}(\mathbf{k},\omega) = -e\mathbf{v}(\omega) = -\frac{ie}{\omega}\mathbf{a}(\omega), \tag{3.35}$$

with $\mathbf{a}(\omega)$ being the time Fourier transform of the particle acceleration. The total energy radiated by the accelerated charge in the electromagnetic (**T**ransversal) mode

$$U^T = \int u^T(\mathbf{k})\frac{\mathrm{d}^3\mathbf{k}}{(2\pi)^3}$$

can be re-expressed using the relations

$$\omega = \frac{ck}{n(\omega)}, \qquad \mathrm{d}^3\mathbf{k} = k^2\mathrm{dk}\ \mathrm{d}\Omega \tag{3.36}$$

and averaging over the solid angle Ω as the sum of contributions with frequency ω:

$$U^T = \int_0^\infty u^T(\omega)\mathrm{d}\omega = \frac{1}{4\pi\varepsilon_0}\cdot\frac{2\mathrm{e}^2}{3\pi\mathrm{c}^3}\int_0^\infty \mathrm{n}(\omega)\left|\mathbf{a}(\omega)\right|^2\mathrm{d}\omega, \tag{3.37}$$

where formula (3.28) for energy radiated calculation with the extraneous current density (3.35) was used. For radio radiation only the distant encounters with large impact parameter b are important as the characteristic frequency radiated is about $f = v/b$. For such encounters the trajectory $\mathbf{r}(t)$ of the moving electron is only slightly departed from rectilinear motion and for the time Fourier transform of the acceleration $\mathbf{a}(t)$ in the electric field of ion

$$\mathbf{a}(t) = -\frac{e}{m_e}\ \frac{Z_i e}{4\pi\varepsilon_0}\ \frac{\mathbf{r}(t)}{|\mathbf{r}(t)|^3}$$

with the electron trajectory approximated by relation $\mathbf{r}(t) = \mathbf{b} + \mathbf{v}t$ one can write

$$\mathbf{a}(\omega) = -\frac{Z_i e^2}{m_e\ 4\pi\varepsilon_0}\int_{-\infty}^{+\infty}\frac{\mathbf{b}+\mathbf{v}t}{(b^2+v^2t^2)^{\frac{3}{2}}}\cdot\exp(i\omega t)\ \mathrm{dt}. \tag{3.38}$$

Here, **b** is the vector connecting the ion and the closest point on the electron straight-line path (its length is the impact parameter b), Z_i is the (fully ionised) ion proton number and **v** is the electron velocity (constant in present approximation). Computing the integral (3.38) and inserting the result into the equation (3.37) the electromagnetic energy radiated by electron during single encounter into the unit interval of frequency is expressed as:

$$u^T(\omega;b) = \frac{1}{4\pi\varepsilon_0}\frac{8n(\omega)Z_i^2e^6\omega^2}{3\pi c^3m_e^2v^4}\left[K_1^2\left(\frac{b\omega}{v}\right)+K_0^2\left(\frac{b\omega}{v}\right)\right], \tag{3.39}$$

with $K_\nu(z)$ being the MacDonald function of index ν (modified Bessel function of the second kind).

The emission of electromagnetic waves is rather continuous as electron experiences multiple encounters with many ions simultaneously. The power radiated by the single electron will be thus relevant quantity. To compute it, one has to estimate the number of collisions per unit time. Considering various impact parameters the radiated power reads:

$$P^T_{single}(\omega;v) = 2\pi n_i v\int_{b_{min}}^{\infty} u(\omega;b)\ b\ \mathrm{db}. \tag{3.40}$$

The integration has to start with the value $b_{min} > 0$ as for smaller impact parameters the present approach is not valid due to violation of straight-line approximation and/or due to need of quantum mechanic treatment of the problem.

The last step in finding the power $P^T(\omega)$ radiated by bremsstrahlung from the unit volume into unit interval of frequency consists in summing all contributions (3.40) to emitted power by single electrons with velocity v over the electron velocity distribution. Thus,

$$P^T(\omega) = \int P^T_{single}(\omega;v)f(\mathbf{v})\mathrm{d}^3\mathbf{v} \tag{3.41}$$

where for the electron distribution function $f(\mathbf{v})$ the normalisation

$$n_e = \int f(\mathbf{v})\mathrm{d}^3\mathbf{v}$$

was used. According to `Melrose 1980` the explicit computation for the Maxwellian distribution in *CGS* units finally gives

$$P^T(\omega) = \frac{16}{3}\frac{n(\omega)Z_i^2e^6n_in_e}{c^3m_e^2}\left(\frac{2}{\pi}\right)\frac{1}{V_e}\frac{\pi}{\sqrt{3}}\,G(T_e,\omega) \tag{3.42}$$

where the Gaunt factor

$$\frac{\pi}{\sqrt{3}}\,G(T_e,\omega) \approx \Lambda_c$$

approximately equals to the Coulomb logarithm in the classical approximation used here.

3.2.1.2 Gyro-synchrotron radiation

As already mentioned above, the gyromagnetic emission (called synchrotron radiation in case of relativistic electrons) is caused by particles spiralling in the imposed magnetic field. The presence of the field brokes the isotropy of the medium and thus the power radiated into the electromagnetic mode by unit volume into the unit frequency interval and unit solid angle, so called emissivity $\eta^T(\omega,\theta)$, will be the relevant quantity describing efficiency of the gyro-synchrotron radiation.
To estimate it, firstly the extraneous current density corresponding to particle (only electrons

will be considered further) spiralling motion has to be identified. Then, using the essential relation (3.28) and the definition (3.29) the power $p^T(\mathbf{k})$ radiated in electromagnetic mode into the unit volume of $\mathbf{k}$-space by single electron can be computed. Finally, using expression (3.36) for element of $\mathbf{k}$-space in spherical coordinates the emissivity $\eta^T(\omega,\theta)$ due to single electron is computed. Moreover, for highly-relativistic particles several simplifications are allowed in the single-electron emissivity formula and in case of well-chosen, but still realistic, distribution functions the sum over particle velocity distribution can be made analytically. Thus, the expression for emissivity from the unit volume of plasmas due to synchrotron radiation is found.

The first step requires the knowledge of the particle trajectory $\mathbf{r}(t)$ that has to be inserted into the relation (3.34) to find the current density caused by single electron. When the coordinate axes are chosen appropriately (see `Melrose 1980`) the spiral orbit of the electron in the magnetic field B is described by radius-vector with the following components:

$$\mathbf{r}(t) = \Big(R\sin(\Omega t), R\cos(\Omega t), v_{\|}t\Big)$$

with definitions of the gyro-frequency Ω and the Larmor radius R

$$\Omega \equiv \frac{eB}{\gamma m_e}, \qquad R \equiv \frac{v_\perp}{\Omega}$$

used; γ is the Lorentz factor. The goniometric function in the exponent of expression (3.34) is to be expanded into series with the Bessel functions $J_s(z)$ as the Fourier coefficients. Consequently, the Fourier image of the extraneous current density is

$$\mathbf{j}(\mathbf{k},\omega) = -2\pi e \sum_{s=-\infty}^{\infty} \mathbf{V}(s,\mathbf{p},\mathbf{k})\delta(\omega - s\Omega - k_{\|}v_{\|})$$

where $\mathbf{V}(s,\mathbf{p},\mathbf{k})$ expressed in components reads

$$\mathbf{V}(s,\mathbf{p},\mathbf{k}) \equiv \left(v_\perp \frac{s}{z} J_s(z), iv_\perp J_s'(z), v_{\|} J_s(z)\right) \tag{3.43}$$

the relativistic relation for electron momentum

$$\mathbf{p} = \gamma m_e \mathbf{v}$$

was used and the argument of Bessel functions is

$$z \equiv k_\perp R = \frac{k_\perp v_\perp}{\Omega} = \frac{k_\perp p_\perp}{eB}.$$

Inserting this current density into the formula (3.28) and differencing with respect to time the power radiated by single electron into the element of $\mathbf{k}$-space in the polarisation given by the vector $\mathbf{e}^T(\mathbf{k})$ is evaluated as:

$$p^T(\mathbf{k}) = \sum_{s=-\infty}^{\infty} \frac{2\pi}{\varepsilon_0} e^2 R_E^T(\mathbf{k}) \left|\overline{\mathbf{e}^T}(\mathbf{k})\cdot\mathbf{V}(s,\mathbf{p},\mathbf{k})\right|^2 \delta(\omega - s\Omega - k_{\|}v_{\|}). \tag{3.44}$$

Now, using the element of $\mathbf{k}$-space (3.36) expressed in the spherical coordinates the emissivity due to single electron is

$$\eta^T_{single}(\omega,\theta) = \frac{e^2 n^2(\omega,\theta)\omega^2}{4\pi^2\varepsilon_0 c^3} \frac{\partial}{\partial\omega}\left(\omega n(\omega,\theta)\right) R_E^T(\omega,\theta) \left|\overline{\mathbf{e}^T}(\theta)\cdot\mathbf{V}(s,\omega,\theta)\right|^2 \times \tag{3.45}$$
$$\times\delta\left[\omega(1 - n(\omega,\theta)\frac{v}{c}\cos\alpha\cos\theta) - s\Omega\right]$$

with α being the electron pitch angle ($\tan\alpha = p_\perp/p_{||}$) and where θ describes wave-vector inclination with respect to the magnetic field:

$$\cos\theta = \frac{\mathbf{k}\cdot\mathbf{B}}{|\mathbf{k}||\mathbf{B}|}.$$

Synchrotron radiation It is rather difficult to sum the single-electron emissivity (3.45) over the electron velocity distribution to find emissivity per unit volume. However, in case of relativistic energies of radiating particles several approximations can be done. For isotropic power-law in energy distribution function

$$f(E) = K\cdot E^{-a}$$

what is very common case in synchrotron radiation sources, one may for emissivity tensor write (in *CGS*, see `Melrose 1980`):

$$\eta_{ik}(\omega,\theta) = \frac{K(m_e c^2)^{1-a}}{16\pi^2 c}\sqrt{3}e^2\Omega\sin\theta\ H_{ik}(a)\left(\frac{2\omega}{3\Omega\sin\theta}\right)^{1-a}. \tag{3.46}$$

Here, the components of matrix $\mathbf{H}(a)$ are as follows:

$$H_{11} = \frac{2^{\frac{a-1}{2}}}{3(a+1)}\,\Gamma\left(\frac{3a+7}{12}\right)\Gamma\left(\frac{3a-1}{12}\right)$$

$$H_{12} = -H_{21} = \frac{-i\cot\theta}{3}\left(\frac{2\omega}{3\Omega\sin\theta}\right)^{-\frac{1}{2}}\ 2^{\frac{a}{2}}\ \frac{a+2}{a}\,\Gamma\left(\frac{3a+8}{12}\right)\ \Gamma\left(\frac{3a+4}{12}\right)$$

$$H_{22} = \frac{(3a+5)2^{\frac{a-3}{2}}}{3(a+1)}\,\Gamma\left(\frac{3a+7}{12}\right)\ \Gamma\left(\frac{3a-1}{12}\right),$$

a is the power-law spectral index, K the normalisation factor and $\Gamma(z)$ Euler gamma function. Using tensor generalisation of emissivity one is able to describe power radiated in arbitrary polarisation state of synchrotron radiation.

3.3 Plasma emission process

Standard radiative mechanisms – the bremsstrahlung and gyro/synchrotron radiation described above are of use also for solar corona radio emission, particularly for quiet sun radiation and slowly-variable component. Nevertheless, solar radio bursts that often consists of intense narrow-band fine structures hardly could be explained only in terms of these processes, since they have by their nature broad-band emission spectrum. Moreover, there is quantitative disagreement in values of radio flux predicted by formulae e.g. (3.42) or (3.46) using reasonable parameters of coronal plasmas and those observed during the bursts.

On the other hand, very hot and sparse coronal plasmas may, due to lack of collisions, easily be in the state of thermodynamic non-equilibrium with non-Maxwellian distribution function, particularly during solar transient events (e.g. flares or CMEs). Under such circumstances the anti-hermitian part $\varepsilon^a_{ij}(\mathbf{k},\omega)$ of the dielectric tensor (3.15) – or its counterpart for magnetised plasmas – can result to negative values of the absorption coefficient (3.32) in some range of wave-vectors for the specific wave mode m. One than says, that distribution function is unstable with respect to generation of wave mode m within some range of $\mathbf{k}$-space. The negative absorption is also often called *stimulated* or *induced* emission.

Such self-generation of waves in unstable plasmas, similar to light amplification in lasers as will be seen further, represents the basis of so called *plasma emission mechanism.* Since there are many types of distribution functions unstable to large amount of wave modes the term "plasma emission" should be regarded as generic name for all radiative processes based primarily on the negative absorption of particular wave modes.

Unfortunately, for the electromagnetic mode which only can escape from the coronal plasmas and reach Earth radiotelescopes the absorption coefficient (3.32) is always positive with one exception of so called electron-cyclotron maser radiation – see paragraph **Absorption coefficient** in the section 3.3.1.1. Thus, some mechanism of conversion between unstable plasma modes and the electromagnetic one is required. Such mechanism is available due to non-linear coupling among variations of plasma parameters (e.g. electric and magnetic field, electron density etc.) in different wave modes.

To sum up, plasma emission mechanism is generic name for class of radiative processes working usually in the following two stages:

1. the wave mode m unstable in some range of $\mathbf{k}$-space is generated due to deviation of distribution function from equilibrium Maxwellian distribution.

2. this mode m is converted via non-linear coupling into the electromagnetic one that escapes solar corona and can be detected on Earth.

Since the region of unstable waves in $\mathbf{k}$-space is usually limited to small extent and also the wave mode conversion is strongly resonant process as will be seen later, resulting radio emission is narrowband and possibly with fine structures as usually observed during solar radio bursts.

Due to mentioned similarity with radiation amplification in lasers it is convenient to adopt principle of detailed balance between emission and absorption processes used in radiative transfer elementary physics and quantitatively expressed using the Einstein coefficients. The theory built on these axioms will be in usual quantum notation briefly reviewed now.

3.3.1 Weak turbulence theory

Stimulated emission and other induced processes such as wave-particle or wave-wave scattering can be under some assumptions described consistently within the weak turbulence theory. It is based on semi-classical formalism – the particles in states with momentum $\mathbf{p}$ are described by distribution function $f(\mathbf{p})$ while the waves in mode m with wave-vector $\mathbf{k}$ is described by the occupation number $N^m(\mathbf{k})$ (number of quanta of wave mode m in state with momentum $\hbar\mathbf{k}$) defined as:

$$N^m(\mathbf{k}) = \frac{w^m(\mathbf{k})}{\hbar\omega^m(\mathbf{k})} \tag{3.47}$$

Such description brings not only the advantage of uniform treatment of various induced processes from the wave generation point of view, but also it enables consistent estimation of back-reaction of particles to wave radiation or absorption since the principle of energetic balance is imposed on microscopic level here. On the other hand, approach (3.47) to wave distribution disables correct description of coherent processes since the phase information about mode depicted by occupation number is lost. Thus, the assumption that phases of waves are unimportant – so called *random phase approximation* – plays key role in the weak turbulence theory. Coherent processes will be discussed in the next section 3.3.2, however such general theory as in case of incoherent emission has not been available yet.

One may start with subset of this general description applied to stimulated emission of waves due to unstable particle distribution function and its back-reaction to wave generation – so called *quasi-linear theory.*

3.3.1.1 Quasi-linear theory

Transferring wave generation and/or absorption processes onto microscopic level one has to use, according to quantum physics, probabilistic description of each elementary emission/absorption action. This is usually done introducing the Einstein coefficients.

Einstein coefficients Consider two states described by particle momenta $\mathbf{p}$ and $\mathbf{p}^-$. Let the total number of particles in state $\mathbf{p}$ is N_p and N_{p^-} for the state $\mathbf{p}^-$, respectively. According to quantum theory the transition of one particle between states $\mathbf{p}$ and $\mathbf{p}^-$ is accompanied by emission or absorption of quantum of waves with frequency given by condition

$$\hbar\omega = |E(\mathbf{p}) - E(\mathbf{p}^-)|. \tag{3.48}$$

Here, $E(\mathbf{p}^-)$ and $E(\mathbf{p})$ are particle energies in the states $\mathbf{p}^-$ and $\mathbf{p}$, respectively. In case of free particles the energy of the state $\mathbf{p}$ reads in non-relativistic limit

$$E(\mathbf{p}) = \frac{\mathbf{p}^2}{2m} \tag{3.49}$$

with m being the particle mass, components of state vector $\mathbf{p}$ are simply Cartesian components of particle momentum. On the other hand, in magnetised plasmas the classical treatment is not sufficient and relativistic quantum theory gives for the eigen energies the following expression (spin of particle is ignored here, see `Melrose 1980`):

$$E(\mathbf{p}) = \sqrt{m_0^2c^4 + 2n|q|B\hbar c^2 + p_\parallel^2 c^2}. \tag{3.50}$$

Due to periodical motion in perpendicular direction the momentum $\mathbf{p}$ has the perpendicular component discrete – determined by the integer number n. Parallel component is continuous and corresponds to projection of momentum to the magnetic field direction, i.e.:

$$\mathbf{p} \equiv (p_\perp, p_\parallel) = \left(\sqrt{2n\ \hbar\Omega\ m}, p_\parallel\right) \tag{3.51}$$

where Ω is the gyrofrequency already introduced in the section 3.2.1.2.

Now suppose that $E(\mathbf{p}^-) < E(\mathbf{p})$ (see Fig. 3.1) and consider probabilities (transition rates) $\mathrm{w}_{p^-p}^{m,abs}(\mathbf{k})$, $\mathrm{w}_{pp^-}^{m,sp}(\mathbf{k})$ and $\mathrm{w}_{pp^-}^{m,ind}(\mathbf{k})$ of transitions between the states $\mathbf{p}$ and $\mathbf{p}^-$ due to absorption, spontaneous and induced emission of quantum of mode m with wave-vector $\mathbf{k}$ (referred as $(m, \mathbf{k})$ quantum further) per unit time, respectively. The rates $\mathrm{w}_{p^-p}^{m,abs}(\mathbf{k})$, $\mathrm{w}_{pp^-}^{m,sp}(\mathbf{k})$ and $\mathrm{w}_{pp^-}^{m,ind}(\mathbf{k})$ represents Einstein coefficients for transitions $\mathbf{p} \rightleftharpoons \mathbf{p}^-$. The total rate of transitions $\mathbf{p}^- \to \mathbf{p}$ due to absorption is

$$-\frac{\mathrm{d}N^m(\mathbf{k})}{\mathrm{d}t} = \mathrm{w}_{p^-p}^{m,abs}(\mathbf{k}) N_{p^-} N^m(\mathbf{k}) \tag{3.52}$$

while total rate of transitions $\mathbf{p} \to \mathbf{p}^-$ as consequence of spontaneous or induced emission reads

$$\frac{\mathrm{d}N^m(\mathbf{k})}{\mathrm{d}t} = \mathrm{w}_{pp^-}^{m,sp}(\mathbf{k}) N_p + \mathrm{w}_{pp^-}^{m,ind}(\mathbf{k}) N_p N^m(\mathbf{k}). \tag{3.53}$$

The relations between the Einstein coefficients can be obtained in the state of thermodynamic equilibrium but it should be noted, that resulting relations are valid regardless of macroscopic state of plasma-waves system as they are fundamental characteristics of the $\mathbf{p} \rightleftharpoons \mathbf{p}^-$ transitions.

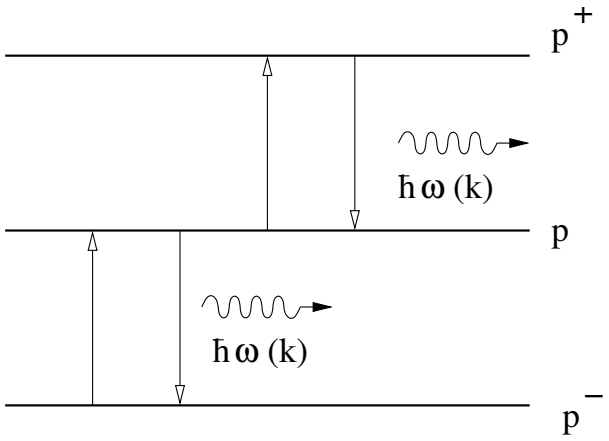

Fig. 3.1: Absorption and emission processes due to $\mathbf{p}^+ \leftrightarrow \mathbf{p}$ and $\mathbf{p} \leftrightarrow \mathbf{p}^-$ state transitions.

In the state of thermodynamic equilibrium adopted principle of detailed balance applies implying that rate of change of occupation number $N^m(\mathbf{k})$ of $(m, \mathbf{k})$ quanta due to absorption and emission processes during $\mathbf{p} \rightleftharpoons \mathbf{p}^-$ transitions together is zero. Thus combining equations (3.52) and (3.53) one obtain

$$\frac{\mathrm{d}N^m(\mathbf{k})}{\mathrm{d}t} = \mathrm{w}^{m,sp}_{pp^-}(\mathbf{k})N_p + \mathrm{w}^{m,ind}_{pp^-}(\mathbf{k})N_p N^m(\mathbf{k}) - \mathrm{w}^{m,abs}_{p^-p}(\mathbf{k})N_{p^-}N^m(\mathbf{k}) = 0. \tag{3.54}$$

In the state of thermodynamic equilibrium the distribution of wave quanta is given by Planck law

$$N^m(\mathbf{k}) = \frac{1}{\exp\left(\frac{\hbar\omega^m(\mathbf{k})}{k_B T}\right)}.$$

Inserting the Planck law into the eq. (3.54) and taking into account that (3.54) has to apply for arbitrarily high temperature T the relation among three Einsteins coefficients is found[4] :

$$\mathrm{w}^{m,abs}_{p^-p}(\mathbf{k}) = \mathrm{w}^{m,sp}_{pp^-}(\mathbf{k}) = \mathrm{w}^{m,ind}_{pp^-}(\mathbf{k}) \equiv \mathrm{w}^m_{pp^-}(\mathbf{k}). \tag{3.55}$$

Quasi-linear equations Using the relations (3.55) the rate the $(m, \mathbf{k})$ quanta are emitted at in the general (non-equilibrium) state due to all transitions that can be taken into account is (see eq. 3.54):

$$\frac{\mathrm{d}N^m(\mathbf{k})}{\mathrm{d}t} = \sum_{p,p^-} \mathrm{w}^m_{pp^-}(\mathbf{k}) \left[N_p + N^m(\mathbf{k})(N_p - N_{p^-})\right]. \tag{3.56}$$

However, the actual number of possible transitions is much less than it seems from eq. (3.56) since the quantum condition

$$\mathbf{p} - \mathbf{p}^- = \hbar\mathbf{k}$$

selects only allowed ones. In particular, the transition rate $\mathrm{w}^m_{pp^-}(\mathbf{k})$ can be expressed as:

$$\mathrm{w}^m_{pp^-}(\mathbf{k}) = \mathrm{w}^m(\mathbf{p}, \mathbf{k}) \cdot \delta(\mathbf{p} - \mathbf{p}^- - \hbar\mathbf{k}). \tag{3.57}$$

Now, one would like to change from discrete notation used hitherto to the continuous one. Thus, the number of particles N_p in the state $\mathbf{p}$ should be replaced by distribution function $f(\mathbf{p})$ and

[4]The relation somewhat differs from that used in classical radiative transfer physics because the occupation number $N^m(\mathbf{k})$ is used here instead of spectral energy density or specific intensity $I^m(\omega, \theta, \phi)$ (θ, ϕ are spherical coordinates) used in radiative transfer

double sum in the equation (3.56) by integration over $\mathbf{p}$ and $\mathbf{p}^-$. Using the expression (3.57) for the transition rate $\mathrm{w}(\mathbf{p},\mathbf{p}^-,\mathbf{k})$, which is now re-interpreted as probability of quantum emission per unit cube of $\mathbf{k}$-space, the integration over p^- is performed trivially due to δ-function. The expression $f(\mathbf{p}-\hbar\mathbf{k})$ appeared in the result can be for $\hbar\mathbf{k} \ll \mathbf{p}$ expanded in Taylor series

$$f(\mathbf{p}\pm\hbar\mathbf{k}) = f(\mathbf{p}) \pm \hbar k_i \frac{\partial f(\mathbf{p})}{\partial p_i} + \frac{1}{2}\,\hbar^2 k_i k_j \frac{\partial^2 f(\mathbf{p})}{\partial p_i \partial p_j} + \dots$$

When only the terms that are meaningful in classical limit $\hbar \mapsto \infty$ (see the paragraph **Transition rates calculation**) are retained, the first quasi-linear equation describing wave generation (or absorption) in plasmas described by distribution function $f(\mathbf{p})$ is finally found:

$$\frac{\mathrm{d}N^m(\mathbf{k})}{\mathrm{d}t} = \int \mathrm{w}^m(\mathbf{p},\mathbf{k}) \left(f(\mathbf{p}) + N^m(\mathbf{k})\hbar\mathbf{k}\cdot\frac{\partial f(\mathbf{p})}{\partial \mathbf{p}} \right) \mathrm{d}^3\mathbf{p} \tag{3.58}$$

As was already mentioned, the advantage of this semi-classical approach consist besides other in possibility of homogeneous description of back-reaction of particle distribution to wave emission/absorption processes. On the microscopic level, each emission or absorption of quantum of waves is connected with transition of particle between two states. Consequently, the time change of number N_p of particles in state $\mathbf{p}$ is given by the difference between net rate the quanta $(m,\mathbf{k})$ are emitted at due to transition $(\mathbf{p}^+ = \mathbf{p}+\hbar\mathbf{k}) \to \mathbf{p}$ and net rate the quanta $(m,\mathbf{k})$ are emitted at due to transition $\mathbf{p} \to (\mathbf{p}^- = \mathbf{p}-\hbar\mathbf{k})$, i.e. (see Fig. 3.1):

$$\frac{\mathrm{d}N_p}{\mathrm{d}t} = \sum_{\mathbf{k}} \mathrm{w}^m_{p^+p}(\mathbf{k}) \left[N_{p^+} + N^m(\mathbf{k})(N_{p^+} - N_p)\right] - \sum_{\mathbf{k}} \mathrm{w}^m_{pp^-}(\mathbf{k}) \left[N_p + N^m(\mathbf{k})(N_p - N_{p^-})\right]. \tag{3.59}$$

Transferring from the discrete notation to the continuous one again and using the Taylor expansion of the transition rate $\mathrm{w}^m(\mathbf{p}^+,\mathbf{k}) = \mathrm{w}^m(\mathbf{p}+\hbar\mathbf{k},\mathbf{k})$ the second quasi-linear equation describing back-reaction of particles distribution to the wave emission/absorption processes reads

$$\frac{\mathrm{d}f(\mathbf{p})}{\mathrm{d}t} = \int \hbar\mathbf{k}\cdot\frac{\partial}{\partial\mathbf{p}} \left[\mathrm{w}^m(\mathbf{p},\mathbf{k}) \left(f(\mathbf{p}) + N^m(\mathbf{k})\ \hbar\mathbf{k}\cdot\frac{\partial f(\mathbf{p})}{\partial\mathbf{p}} \right) \right] \frac{\mathrm{d}^3\mathbf{k}}{(2\pi)^3}. \tag{3.60}$$

In the magnetised case $\mathbf{p}$ has to be interpreted in agreement with equations (3.50) and (3.51) and the wave-vector $\mathbf{k}$ consequently has components:

$$\mathbf{k} \equiv (k_\perp, k_{||}) = \left(\frac{s\Omega}{v_\perp}, k_{||} \right) \tag{3.61}$$

with s being integer number. Using these relations, the quasi-linear equations (3.58) and (3.60) can be rewritten for the case of plasmas with ambient magnetic field – the explicit calculation could be found in `Melrose 1980`.

Transition rates calculation To make equations (3.58) and (3.60) meaningful for practical computation one has to calculate the emission rate $\mathrm{w}^m(\mathbf{p},\mathbf{k})$. It can be done when one re-interprets the power radiated $p^m(\mathbf{k})$ considered in the section 3.1.2 as continuous process to be – according to quantum physics ideas – the series of quanta emissions with emission probability per unit time $\mathrm{w}(\mathbf{p},\mathbf{k})$, i.e.:

$$p^m(\mathbf{k}) = \hbar\omega^m(\mathbf{k})\ \mathrm{w}^m(\mathbf{p},\mathbf{k})$$

Thus, using relations (3.28) and (3.29) the emission rate can be expressed as:

$$\mathrm{w}^m(\mathbf{p},\mathbf{k}) = \frac{\mathrm{d}}{\mathrm{d}t} \left(\frac{1}{\hbar\omega^m(\mathbf{k})} \frac{R^m_E(\mathbf{k})}{\varepsilon_0} \left| \overline{\mathbf{e}^m}(\mathbf{k}) \cdot \mathbf{j}^{ext}(\mathbf{k},\omega^m(\mathbf{k})) \right|^2 \right) \tag{3.62}$$

In the force-free collision-less plasmas particle moves on rectilinear trajectory. Consequently, the extraneous current density in the equation (3.62) is to be identified with that given by equation (3.34) with rectilinear trajectory

$$\mathbf{r}(t) = \mathbf{r}_0 + \mathbf{v}t$$

inserted. Explicit calculation gives

$$\mathrm{w}^m(\mathbf{p},\mathbf{k}) = \frac{2\pi q^2 R_E^m(\mathbf{k})}{\hbar\omega^m(\mathbf{k})\ \varepsilon_0} \left|\overline{\mathbf{e}^m}(\mathbf{k})\cdot\mathbf{v}\right|^2\ \delta\left(\omega^m(\mathbf{k}) - \mathbf{k}\cdot\mathbf{v}\right) \tag{3.63}$$

For the magnetised case with spiral trajectories the result can be obtained directly generalising the relation (3.44) for power radiated by single electron into transversal waves to expression valid for arbitrary mode and particle. An explicit calculation gives:

$$\mathrm{w}^m(\mathbf{p},\mathbf{k}) = \sum_{s=-\infty}^{\infty} \mathrm{w}^m(s,\mathbf{p},\mathbf{k})$$

where $\mathrm{w}^m(s,\mathbf{p},\mathbf{k})$ is abbreviation for

$$\mathrm{w}^m(s,\mathbf{p},\mathbf{k}) = \frac{2\pi q^2 R_E^m(\mathbf{k})}{\hbar\omega^m(\mathbf{k})\ \varepsilon_0} \left|\overline{\mathbf{e}^m}(\mathbf{k})\cdot\mathbf{V}(s,\mathbf{p},\mathbf{k})\right|^2\ \delta\left(\omega^m(\mathbf{k}) - s\Omega - k_{\|}v_{\|}\right) \tag{3.64}$$

with Ω being the gyrofrequency and the quantity $\mathbf{V}(s,\mathbf{p},\mathbf{k})$ defined by relation (3.43) in the section 3.2.1.2.

Absorption coefficient As was already mentioned, the first quasi-linear equation (3.58) expresses the emission or absorption of wave quanta due to medium described by distribution function. The rate of occupation number change can be separated to two parts – one independent of the occupation number itself

$$\left[\frac{\mathrm{d}N^m(\mathbf{k})}{\mathrm{d}t}\right]^{sp} = \int \mathrm{w}^m(\mathbf{p},\mathbf{k})\ f(\mathbf{p})\ \mathrm{d}^3\mathbf{p}$$

and one linearly proportional to it

$$\left[\frac{\mathrm{d}N^m(\mathbf{k})}{\mathrm{d}t}\right]^{ind} = -\gamma^m(\mathbf{k})N^m(\mathbf{k})$$

where $\gamma^m(\mathbf{k})$ reads

$$\gamma^m(\mathbf{k}) = -\int \mathrm{w}^m(\mathbf{p},\mathbf{k})\ \hbar\mathbf{k}\cdot\frac{\partial f(\mathbf{p})}{\partial\mathbf{p}}\ \mathrm{d}^3\mathbf{p}. \tag{3.65}$$

As the superscripts over each part indicate the former part describes spontaneous or thermal wave emission whereas the latter belongs to induced processes. The quantity $\gamma^m(\mathbf{k})$ is absorption coefficient by definition and its sign depend on what process prevails – whether absorption or stimulated emission of waves. In case of negative values also the term *growth rate* is often used.

It is clear from expression (3.65) that in case of positive slope of distribution function $f(\mathbf{p})$ in the direction of wave-vector $\mathbf{k}$ the absorption coefficient $\gamma^m(\mathbf{k})$ can reach negative values implying so self-amplification or instability of waves. The positive slope corresponds to inequality

$$N_{p+\hbar k} > N_p$$

in the formula (3.56), which is only discrete form of the first quasi-linear equation (3.58), and thus inverse population of energetic levels is required (in unmagnetised plasmas) for self-amplification

to work. This feature of the theory of induced processes in plasmas makes it very close to, now already classical, physics of lasers as was already mentioned in the introduction to this section. Probably the most known examples of amplification of waves due to such inverse population of energetic levels in the field of plasma physics are the "Bump-in-Tail" or "Two-stream" instabilities of Langmuir waves. The positive slope of the particle distribution function is reached by energetic particle stream propagating through the thermal background plasmas in this case.

In magnetised case, the momentum $\mathbf{p}$ and the wave vector $\mathbf{k}$ has to be interpreted according to expressions (3.51) and (3.61) and, consequently, the formula (3.65 for the absorption coefficient $\gamma^m(\mathbf{k})$ rewritten for use in magnetised plasmas reads:

$$\gamma^m(\mathbf{k}) = -\sum_{s=-\infty}^{\infty} \int \mathrm{w}^m(s,\mathbf{p},\mathbf{k})\ \hbar \left(\frac{s\Omega}{v_\perp} \frac{\partial}{\partial p_\perp} + k_{||}\ \frac{\partial}{\partial p_{||}} \right)\ f(\mathbf{p})\ \mathrm{d}^3\mathbf{p} \tag{3.66}$$

with emission rate per s-harmonic $\mathrm{w}^m(s,\mathbf{p},\mathbf{k})$ given by the relation (3.64).

The particular importance of the formula (3.66) consist in possibility of direct amplification of electromagnetic mode in process known as *cyclotron maser*. The cyclotron maser works if: 1) conditions for negative absorption are fulfilled in some range of wave-vectors and, 2) generated electromagnetic mode can escape the solar corona. It can be shown, that the absorption coefficient (3.66) with emission rate (3.64) allows such situation under some conditions. It is unlike the unmagnetised case, where components of $\mathbf{k}$-vector is to be interpreted simply as Cartesian components of the wave vector. Then, the resonant condition contained implicitly due to δ-function in the relation (3.63) can be fulfilled only if

$$v \geq v_\varphi \tag{3.67}$$

where $v_\varphi = \omega(\mathbf{k})/k$ is the wave phase velocity. Since refractive index for electromagnetic waves $n^T(\mathbf{k}) < 1$ for all $\mathbf{k}$-vectors, negative absorption of this mode is forbidden in the case of unmagnetised plasmas as a consequence of apparent inequality

$$v < c$$

Hence, the mode conversion between waves that can satisfy the condition (3.67), and their amplification is therefore possible, and the electromagnetic ones is required for plasma emission process to work. Some mechanisms of the mode conversion will be discussed in sections 3.3.1.2 and 3.3.2.2.

Let us finish discussion of the absorption coefficient with legitimate question of relation between the coefficient (3.65) calculated within the quasi-linear theory and that determined classically in the section 3.1.2 by formula (3.32). The answer is, that both quantities are identical provided that for computation of the anti-hermitian part of dielectric tensor in the expression (3.32) the relation valid for collision-less plasmas given by equation (3.15) is used. Thus, for collision-less damping of waves the two approaches are equivalent.

3.3.1.2 Other induced processes

The indubitable advantage of the weak turbulence theory is its microscopic level approach to particles-waves system. This approach allows one to treat homogeneously not only processes where single particle and single wave quantum take part, as described by quasi-linear theory reviewed briefly in the previous section 3.3.1.1, but also multiple quanta-particle or quanta-quanta interactions as well. Among many such processes the two ones are of great importance, particularly for the second stage of plasma emission:

1. the induced scattering of waves on particles
2. the three-wave interactions

as both of them represents an efficient way of mode conversion.

Induced scattering When some wave mode propagates through plasmas the induced motion of particles (i.e. induced current) connected with this mode becomes the source of waves. In the continuum approximation for homogeneous plasmas the same wave mode with the same wave vector and frequency is reproduced only, just in agreement with the Huygens principle, and contributions to different waves mutually cancel out. Nevertheless, this is not exactly true when the discrete character of matter is taken into account. The sum of radiation from each single particle contains besides the initial wave field also component with different wave-vector/frequency or even of different mode. This component of wave field is referred as scattered wave further.

Such scattering of waves by particles is well known from classical electromagnetic field theory and as an illustrative example the Thomson scattering of light on free electrons in the solar corona can be adduced. Nevertheless, this process may have besides its spontaneous version also amplified form. It applies if the absorption coefficient (3.65) of the wave given by the envelope caused by interference between initial and scattered modes is negative. Then this envelope wave is amplified and thus the rate of the scattering process is proportional to initial and scattered wave occupation numbers, as expected for an induced process.

Both, spontaneous and induced contributions to the scattering can be described by set of kinetic equations whose derivation in the scope of the semi-classical formalism used is very similar to that of the quasi-linear equations (3.58) and (3.60) – see `Melrose 1980` for details. For scattering of the $(m,\mathbf{k})$ waves into the $(m',\mathbf{k}')$ ones (the process is usually schematicaly designated as $m \mapsto m'$ in literature) the following relations are found:

$$\frac{\mathrm{d}N^{m}(\mathbf{k})}{\mathrm{d}t} = \int \mathrm{w}^{mm'}(\mathbf{p},\mathbf{k},\mathbf{k}') \times \tag{3.68}$$
$$\times \left(f(\mathbf{p})[N^{m'}(\mathbf{k}') - N^{m}(\mathbf{k})] + N^{m'}(\mathbf{k}')N^{m}(\mathbf{k})\ \hbar(\mathbf{k}-\mathbf{k}') \cdot \frac{\partial f(\mathbf{p})}{\partial \mathbf{p}} \right) \mathrm{d}^3\mathbf{p}\ \frac{\mathrm{d}^3\mathbf{k}'}{(2\pi)^3}$$

and

$$\frac{\mathrm{d}N^{m'}(\mathbf{k}')}{\mathrm{d}t} = -\int \mathrm{w}^{mm'}(\mathbf{p},\mathbf{k},\mathbf{k}') \times \tag{3.69}$$
$$\times \left(f(\mathbf{p})[N^{m'}(\mathbf{k}') - N^{m}(\mathbf{k})] + N^{m'}(\mathbf{k}')N^{m}(\mathbf{k})\ \hbar(\mathbf{k}-\mathbf{k}') \cdot \frac{\partial f(\mathbf{p})}{\partial \mathbf{p}} \right) \mathrm{d}^3\mathbf{p}\ \frac{\mathrm{d}^3\mathbf{k}}{(2\pi)^3}.$$

The first equation describes the rate of change of the occupation number of the initial wave $(m,\mathbf{k})$, similarly the second determines creation/annihilation of the scattered $(m',\mathbf{k}')$ quanta. As a consequence of scattering process the particle distribution also varies. The corresponding equation as well as the explicit expression for the scattering rate $\mathrm{w}^{mm'}(\mathbf{p},\mathbf{k},\mathbf{k}')$ can be found in `Melrose 1980`.

Three-wave interactions Another possibility of the mode conversion is given by non-linear wave-wave interactions. The physical basis of this process for simplest case of coalescence of two waves into the third is as follows: The each wave modes are independent only in the linear approximation. Nevertheless, in reality the wave propagating in plasmas where another wave is present does not see homogeneous medium but that modified by the former wave, and vice versa. As a consequence, the non-linear contribution to current appears and becomes the source of the third wave.

The process just considered above can be also described within the semi-classical formalism of the weak-turbulence theory provided the phases of each quanta are uncorrelated. This is always true in the case of broad-band distributions of waves since the coherence time for the wave mode m can be estimated as

$$\tau_c \approx \frac{1}{\Delta\omega^m(\mathbf{k})}$$

where $\Delta\omega^m(\mathbf{k})$ is the characteristic width of the mode m distribution. The coherent version of this processes is described by *strong-turbulence theory* based on the Zakharov equations and briefly reviewed in the section 3.3.2.2.

For the coalescence process of two quanta $(m', \mathbf{k}')$ and $(m'', \mathbf{k}'')$ into the third $(m, \mathbf{k})$ (and simultaneously running decay of the final quanta $(m, \mathbf{k})$ into the initial ones – schematically $m' + m'' \rightleftharpoons m$) the following set of equations can be found in the weak-turbulence approach (see `Melrose 1980`):

$$\frac{\mathrm{d}N^m(\mathbf{k})}{\mathrm{d}t} = \int \mathrm{u}^{mm'm''}(\mathbf{k}, \mathbf{k}', \mathbf{k}'') \times \tag{3.70}$$
$$\times \left(N^{m'}(\mathbf{k}') N^{m''}(\mathbf{k}'') - N^m(\mathbf{k}) N^{m'}(\mathbf{k}') - N^m(\mathbf{k}) N^{m''}(\mathbf{k}'') \right) \frac{\mathrm{d}^3\mathbf{k}'}{(2\pi)^3} \frac{\mathrm{d}^3\mathbf{k}''}{(2\pi)^3}$$

for the coalesced wave occupation number rate of change and

$$\frac{\mathrm{d}N^{m'}(\mathbf{k}')}{\mathrm{d}t} = -\int \mathrm{u}^{mm'm''}(\mathbf{k}, \mathbf{k}', \mathbf{k}'') \times \tag{3.71}$$
$$\times \left(N^{m'}(\mathbf{k}') N^{m''}(\mathbf{k}'') - N^m(\mathbf{k}) N^{m'}(\mathbf{k}') - N^m(\mathbf{k}) N^{m''}(\mathbf{k}'') \right) \frac{\mathrm{d}^3\mathbf{k}}{(2\pi)^3} \frac{\mathrm{d}^3\mathbf{k}''}{(2\pi)^3}$$

and

$$\frac{\mathrm{d}N^{m''}(\mathbf{k}'')}{\mathrm{d}t} = -\int \mathrm{u}^{mm'm''}(\mathbf{k}, \mathbf{k}', \mathbf{k}'') \times \tag{3.72}$$
$$\times \left(N^{m'}(\mathbf{k}') N^{m''}(\mathbf{k}'') - N^m(\mathbf{k}) N^{m'}(\mathbf{k}') - N^m(\mathbf{k}) N^{m''}(\mathbf{k}'') \right) \frac{\mathrm{d}^3\mathbf{k}}{(2\pi)^3} \frac{\mathrm{d}^3\mathbf{k}'}{(2\pi)^3}$$

for the initial wave quanta rates. The specific conversion rate[5] $\mathrm{u}^{mm'm''}(\mathbf{k}, \mathbf{k}', \mathbf{k}'')$ can be determined expanding the current density $\mathbf{j}^{ind}(\mathbf{k}, \omega)$ induced in plasmas into series of powers of the electric field $\mathbf{E}(\mathbf{k}, \omega)$ and the resulting expression is to be found in `Melrose 1980`. Note only, that as the consequence of momentum and energy conservation on microscopic level

$$\hbar\mathbf{k}' + \hbar\mathbf{k}'' = \hbar\mathbf{k} \qquad \hbar\omega^{m'}(\mathbf{k}') + \hbar\omega^{m''}(\mathbf{k}'') = \hbar\omega^m(\mathbf{k})$$

the specific coalescence rate $\mathrm{u}^{mm'm''}(\mathbf{k}, \mathbf{k}', \mathbf{k}'')$ contains delta-functions in its expression, in particular

$$\mathrm{u}^{mm'm''}(\mathbf{k}, \mathbf{k}', \mathbf{k}'') \propto \delta(\mathbf{k} - \mathbf{k}' - \mathbf{k}'') \times \delta[\omega^m(\mathbf{k}) - \omega^{m'}(\mathbf{k}') - \omega^{m''}(\mathbf{k}'')],$$

what indicates that three-wave interactions are strongly resonant processes.

[5] The probability that quantum from the unit cube of $\mathbf{k}$-space around the wave-vector $\mathbf{k}'$ coalesce per unit time with the quantum from the unit cube of $\mathbf{k}$-space around the wave-vector $\mathbf{k}''$ to result in the quantum from the unit cube of $\mathbf{k}$-space around the wave-vector $\mathbf{k}$

3.3.2 Coherent processes

The weak-turbulence theory just reviewed in the previous section is capable to describe homogeneously many types of particle-wave or wave-wave interactions, provided that wave field is sufficiently described by occupation numbers – i.e. that wave phases are unimportant. As was shown, such condition is fulfilled in case of broad-band wave distributions as after the coherence time τ_c the phases of waves are completely mixed. Nevertheless, sometimes the region of unstable waves in the **k**-space is so narrow, that before the phase mixing state is reached the waves have grown up substantially.

For such cases the weak-turbulence theory is inapplicable and its departure from the reality can be separated into two kinds of problems:

- the theory predicts qualitatively some process (e.g. instability) to be running, but further quantitative analysis gives wrong results – usually predicted growth rates of unstable waves are lower than in reality.
- the weak-turbulence version of coherent process does not exist at all.

Hence, processes where also wave phases are important have to be treated another way. Unfortunately, the general theory of coherent processes – as a counterpart of the weak-turbulence theory – has not been established yet. Two particular cases will be discussed in the following.

3.3.2.1 Two-stream instability

The two-stream (sometimes also, and more pertinently, designated as bump-in-tail) instability represents an example of such kind of process whose coherent as well as weak-turbulence (just quasi-linear in this case) versions exist. Usually this term is used for the situation, when thermal Maxwellian distribution (the main stream) is perturbed by low-density beam of energetic particles giving raise to unstable Langmuir waves.

Generally, the specific dispersion relation for Langmuir waves propagating through such perturbed plasmas can be found including the beam-contributed part of dielectric tensor into the general dispersion equation (3.23). For unmagnetised plasmas the separation (3.16) of the dielectric tensor into the longitudinal and transversal parts applies. The Maxwellian beam of electrons

$$f_b(\mathbf{v}) = \frac{n_b}{(\sqrt{2\pi}\Delta V_b)^3} \exp\left[-\frac{(\mathbf{v}-\mathbf{U}_b)^2}{2(\Delta V_b)^2}\right]$$

contributes to the longitudinal component by value (according to `Melrose 1980`):

$$\Delta\varepsilon^l(\mathbf{k},\omega) = \left(\frac{\omega_{pb}}{k\Delta V_b}\right)^2 [1-\phi(y_b)+i\sqrt{\pi}y_b\exp(-y_b^2)], \tag{3.73}$$

where n_b is the beam electron density, $\mathbf{U}_b$ and ΔV_b the mean beam velocity and the beam velocity spread, respectively; the beam plasma frequency is defined as

$$\omega_{pb} \equiv \sqrt{\frac{n_b e^2}{m_e \varepsilon_0}},$$

the y_b is the abbreviation for

$$y_b = \frac{\omega - \mathbf{k}\cdot\mathbf{U}_b}{\sqrt{2}k\Delta V_b}$$

and the function $\phi(y)$ was introduced in the eq. (3.17). The equation (3.19) generalised for case of damped/growing waves thus gives for longitudinal (electrostatic) waves in presence of the electron beam relation

$$\varepsilon_0^l(\mathbf{k},\omega) + \Delta\varepsilon^l(\mathbf{k},\omega) = 0 \tag{3.74}$$

where $\varepsilon_0^l(\mathbf{k},\omega)$ is the background plasma contribution to the longitudinal part of the dielectric tensor given by the relation (3.17). The presence of the low-density electron beam may be regarded as a perturbation and hence the specific dispersion relation for Langmuir waves $\omega = \omega^L(\mathbf{k})$ only slightly differs from that obtained in the unperturbed case $\omega_0^L(\mathbf{k})$ and given by relation (3.21), i.e.

$$\omega^L(\mathbf{k}) = \omega_0^L(\mathbf{k}) + \Delta\omega^L(\mathbf{k}).$$

In the first order approximation the equation (3.74) can be rewritten into the form:

$$\Delta\omega^L(\mathbf{k}) \left.\frac{\partial\varepsilon_0^l(\mathbf{k},\omega)}{\partial\omega}\right|_{\omega=\omega_0^L(\mathbf{k})} + \Delta\varepsilon^l(\mathbf{k},\omega) = 0$$

from which the frequency difference $\Delta\omega^L(\mathbf{k})$ can be further expressed using the relation (3.24) as

$$\Delta\omega^L(\mathbf{k}) = -\omega_0^L(\mathbf{k}) R_E^L(\mathbf{k}) \Delta\varepsilon^l(\mathbf{k},\omega). \tag{3.75}$$

Now, when wave growth/damping is included, the function $\phi(y)$ contained in the dielectric tensor perturbation (3.73) needs to be regarded as a function of complex variable y_b. This fact brings some difficulty with expansion of the function $\phi(y)$ into series, as this expansion is not unambiguous for physically relevant case $|y_b| \gg 1$ and depends on ratio between real and imaginary part of frequency ω. In fact, only two limiting cases can be treated analytically using expansion of the function $\phi(y)$; both of them will be now briefly discussed.

1. Im[y]≫1 As a consequence of the y_b definition this limit implies the condition

$$\mathrm{Im}\{\omega\} \gg k\Delta V_b. \tag{3.76}$$

Since the bandwidth of waves unstable due to presence of the beam can be estimated by the parameter $k\Delta V_b$, the condition (3.76) means that wave growth rate is much greater then wave distribution bandwidth. In such a case the wave phases are not mixed during one growth period and become important for the process of instability. The expansion of the function $\phi(y)$ gives for this limit the following expression:

$$\Delta\varepsilon^l(\mathbf{k},\omega) \approx -\frac{\omega_{pb}^2}{(\omega - \mathbf{k}\cdot\mathbf{U}_b)^2}.$$

Inserting it into the equation (3.75) together with approximations $\omega_0^L(\mathbf{k}) \approx \omega_p$ and $R_E^L(\mathbf{k}) \approx \frac{1}{2}$ the cubic equation for the frequency difference $\Delta\omega^L(\mathbf{k})$ is obtained

$$\Delta\omega^L(\mathbf{k}) = \frac{1}{2}\,\frac{\omega_p\omega_{pb}^2}{\left(\Delta\omega^L(\mathbf{k}) + \omega_p - \mathbf{k}\cdot\mathbf{U}_b\right)^2}$$

whose solution (one of three) reads

$$\Delta\omega^L(\mathbf{k}) = \left(\frac{n_b}{n}\right)^{1/3} (\alpha + i\beta)\ \omega_p \tag{3.77}$$

with real constant α and β of order of unity (detailed result can be found in `Melrose 1980`). Hence, the growth rate of the coherent version of the two-stream instability can be estimated as

$$\gamma^L(\mathbf{k}) \approx \left(\frac{n_b}{n}\right)^{1/3} \omega_p$$

and it applies in the low-velocity-spread limit

$$\left(\frac{n_b}{n}\right)^{1/3} \omega_p \gg k\Delta V_b.$$

2. Re[y]$\gg$ 1 In this limit the expansion of $\phi(y)$ in the first order approximation gives:

$$\Delta\varepsilon^l(\mathbf{k},\omega) \approx -\frac{\omega_{pb}^2}{(\omega_0^L(\mathbf{k}) - \mathbf{k}\cdot\mathbf{U}_b)^2} + \frac{i\omega_{pb}^2}{(k\Delta V_b)^2}\sqrt{\pi}\; y_b \exp(-y_b^2). \tag{3.78}$$

Since imaginary part is small now due to the exponential factor $\exp(-y_b^2)$ one could expect randomisation of wave phases in times less then one growth period and, thus applicability of the weak-turbulence theory. And really, inserting the expansion (3.78) into the relation (3.75) and using obvious simplifications $\omega_0^L(\mathbf{k}) \approx \omega_p$, $R_E^L(\mathbf{k}) \approx \frac{1}{2}$ the imaginary part of $\Delta\omega^L(\mathbf{k})$ can be expressed as

$$\mathrm{Im}\{\Delta\omega^L(\mathbf{k})\} = \frac{\omega_p\omega_{pb}^2}{(\sqrt{2}k\Delta V_b)^3}\sqrt{\pi}\;(\mathbf{k}\cdot\mathbf{U}_b - \omega_p)\exp\left(-\frac{(\mathbf{k}\cdot\mathbf{U}_b - \omega_p)^2}{(\sqrt{2}k\Delta V_b)^2}\right).$$

This result can be directly compared with that obtained from quasi-linear theory using say equation (3.65). Both results are found to be identical when relation (3.33) is used.

Finally, let us note that terminology on this topic has not been unified yet and various terms designating the coherent and incoherent (quasi-linear) version of the two-stream (bump-in-tail) instability are used in the literature. The coherent instability is also frequently termed as *reactive* or, particularly in Russian literature, *of fluid type*, while for its quasi-linear version the designations *resistive* or *of kinetic type* are used as well.

3.3.2.2 Strong wave turbulence

Strong wave turbulence is generic term for non-linear wave-wave interactions that can not be sufficiently described within the weak-turbulence theory just due to great importance of wave phases for processes involved. The first description of coherent wave-wave interactions is that by Zakharov (`1972`) who treated the non-linear interaction between Langmuir and ion-sound waves. His approach was roughly as follows:

Firstly, let us consider linear Langmuir and ion-sound waves in homogeneous plasmas. The time evolution of plasma parameters variations in these waves can be derived most simply within the plasma two-fluid theory or alternatively they can be guessed Fourier transforming the dispersion relations (3.21) and (3.22) for relevant waves into the coordinate space. Hence, the electric field variation in Langmuir waves is governed by equation

$$\frac{\partial^2\mathbf{E}}{\partial t^2} - 3V_e^2\triangle\mathbf{E} + \omega_{pe}^2\mathbf{E} = 0 \tag{3.79}$$

and similarly the electron density variation n in the ion-sound waves fulfils (for wavelengths $\lambda \ll \lambda_{De}$) relation

$$\frac{\partial^2 n}{\partial t^2} - c_s^2\triangle n = 0. \tag{3.80}$$

Now suppose that both wave modes propagate through plasma simultaneously. Due to ion-sound wave the electron density is now distributed non-uniformly and as a consequence of the plasma frequency definition (3.18) the last term $\omega_{pe}^2\mathbf{E}$ in the eq. (3.79) depends explicitly on time and space. Hence, the equation (3.79) can be rewritten in the form

$$\frac{\partial^2\mathbf{E}}{\partial t^2} - 3V_e^2\triangle\mathbf{E} + \omega_{pe}^2\mathbf{E} = -\omega_{pe}^2\frac{n(\mathbf{r},t)}{n_0}\mathbf{E} \tag{3.81}$$

where the plasma frequency ω_{pe} is now re-interpreted as that connected with the background average density n_0. Equation (3.81) describes Langmuir wave electric field evolution under the influence of ion-sound density perturbation. The effect of density distribution can be estimated qualitatively even without solving it by analogy with the Schrödinger wave equation describing an electron inside the crystal lattice (c.f. equation 3.84). Identifying the total density n_0+n with crystal single-electron potential one finds, that the Langmuir electric field tends to concentrate itself in the density holes, similarly as electron probability density in the crystal is high in places of low potential (in the vicinity of ions locations).

On the other hand, non-homogeneous (averaged over wavelength) electric field influences density distribution due to non-linear ponderomotive force F_{NL} whose volume density is (e.g. `Chen 1984`):

$$\mathbf{f}_{NL} = -\frac{\omega_{pe}^2}{\omega^2}\,\mathbf{grad}\,\frac{\varepsilon_0\langle E^2\rangle}{2}. \tag{3.82}$$

where $\langle\ \rangle$ denotes the fast-time (on scales of several plasma period) averaging. As a consequence, a source term has to appear on the R.H. side of equation (3.80), i.e.

$$\frac{\partial^2 n}{\partial t^2} - c_s^2\triangle n = \frac{1}{m_i}\ \mathrm{div}\ \mathbf{f}_{NL}. \tag{3.83}$$

Since changes of electric field amplitude and ion-sound density variations are slow in comparison with plasma frequency it is convenient to separate the instantaneous Langmuir electric field time evolution into the fast (on plasma frequency) variations and the slowly varying complex amplitude

$$\mathbf{E}(\mathbf{r},t) = \frac{1}{2}\left[\mathcal{E}(\mathbf{r},t)\cdot\exp(-i\omega_{pe}t) + \overline{\mathcal{E}}(\mathbf{r},t)\cdot\exp(+i\omega_{pe}t)\right]$$

Using this separation and relation (3.82) for ponderomotive force, further omitting the second derivative of slowly changing complex amplitude $\mathcal{E}(\mathbf{r},t)$ the equations (3.81) and (3.83) can be rewritten in the form (see e.g. `Zakharov 1972`, `Robinson 1997`):

$$i\frac{\partial\mathcal{E}}{\partial t} + \frac{3V_e^2}{2\omega_{pe}}\triangle\mathcal{E} = \omega_{pe}\frac{n}{2n_0}\mathcal{E} \tag{3.84}$$

$$\frac{\partial^2 n}{\partial t^2} - c_s^2\triangle n = \frac{\varepsilon_0}{4m_i}\ \triangle|\mathcal{E}|^2. \tag{3.85}$$

The relations (3.84, 3.85) are known as set of Zakharov equations and describe coherent non-linear interactions of Langmuir and ion-sound waves.

Since Zakharov early work (`Zakharov 1972`) further generalisations of theses equations were made. The most natural one is including the electromagnetic terms into the eq. (3.81) – see e.g. `Zakharov et al. 1985`. The second Zakharov equation (3.85) was modified as well since in its original fluid-theory formulation was not applicable in some (particularly short-wavelength) limit – this drawback was solved using kinetic approach. Both generalised equations are explicitly written down (see equations 5.1) and used extensively further in the Chapter 5.

Let us now turn to particular non-linear wave processes described by equations (3.84, 3.85) – or their generalised version (5.1) – and known also as *parametric instabilities.*

Three-wave interactions Among three wave interactions belong coalescence of two waves into the third or decay of one pump wave into two daughter modes. Generally both these processes can be schematically written as

$$m' + m'' \rightleftharpoons m$$

where symbols m, m' and m'' may be one of L, S or T for **L**angmuir, ion-**S**ound or **T**ransversal (electromagnetic) modes if the generalised Zakharov equations (5.1) are used. The processes described here represent coherent – and therefore more efficient – version of three-wave interactions discussed in the section 3.3.1.2. In that section also the physical mechanism of the coalescence process was described. Explanation of parametric decay can be seen more clearly just in its coherent variant:

Let us suppose plane Langmuir wave (for instance) propagating through plasmas where also plane ion-sound wave is present. The density pattern formed by the ion-sound wave represents – according to the first Zakharov equation – a system of semi-reflecting mirrors for the Langmuir wave. Hence, very similarly to the Bragg reflections of X-rays in crystalline materials – but, with the Doppler shift (and/or mode change) given by motion of density pattern – the Langmuir wave is partly reflected. On the other hand, the total electric field given by the sum of both incident and reflected waves causes by means of ponderomotive force (3.82) amplification of the ion-sound wave. This amplification further leads to more efficient reflections of parent Langmuir wave and thus the positive feedback is established. The instability grow until non-linear effects of higher order will take place.

For use in solar coherent radio emission theory particularly following processes are most often considered:

$$L \rightarrow L' + S, \quad L' + S \rightarrow T$$

or

$$L \rightarrow T + S$$

for radiation on the frequency $\approx \omega_{pe}$ and

$$L' + L \rightarrow T$$

for the second harmonic ($\approx 2\omega_{pe}$) emission.

Modulational instabilities Unlike the three-wave processes discussed above the modulational instability has no weak-turbulence counterpart since coherence of waves is essential in this process. There are four waves taking part in the instability and physical mechanism is as follows:

Suppose plane Langmuir wave again propagating, for simplicity, in direction parallel to that of weak plane ion-sound wave. Due to the first Zakharov equation the Langmuir electric field tends to concentrate near density minima of ion-sound wave. Hence, the electric field of parent Langmuir wave becomes slightly modulated:

$$E^L(x) = E_0 \cos(kx) \cdot (1 + m\cos(Kx))$$

where k and K are Langmuir and ion-sound wave wave-numbers, respectively and m is small parameter of order $m \approx n/n_0$ describing modulational effect of density pattern onto Langmuir wave. The essence of the instability consist in the simple mathematical relation

$$\cos(kx)\cos(Kx) = \frac{1}{2} \ (\cos[(k+K)x] + \cos[(k-K)x])$$

indicating that side-band Langmuir waves with wave-numbers $k + K$ and $k - K$ are excited as well. As in the previous case, the ponderomotive force given by the total electric field by all three Langmuir waves causes increase of density variations what on the other hand makes the modulation deeper. Finally let us note, that in case of non-parallel mutual propagation of parent Langmuir wave and ion-sound density variation the growing side-band(s) may be radiated in the electromagnetic mode (hybrid instability) giving such also an effective way of plasma wave conversion into the radio radiation.

Both three-wave and four-wave interactions with respect to possible applications to solar flares radio radiation are further studied in the Chapter 5, section 5.1.

Chapter 4

Interpretation of observed radio spectra

Information coming from dynamic radio spectra is basically of two kinds. Firstly, the time evolution of instantaneous spectrum, manifested as traces of various shapes in frequency-time plane, corresponds to time evolution of relevant physical parameters (e.g. electron density or magnetic field strength) in the local reference frame of the radio source. By qualitative interpretation of radio spectrum will be meant identification of processes in the solar atmosphere causing such time variation of source parameters leading to observed **patterns** in the dynamic spectrum, together with determining of elementary emission mechanism. The second type of information which can be obtained from the spectrum, provided that the first step just described above was successfully completed, concerns quantitative determination of some coronal parameters from observed **values** of radio flux for some frequency and time. This chapter deals with the qualitative interpretation (furthermore referred as interpretation only), while some preliminary steps needed for converting radio flux to values of coronal parameters are described in the next one (5).

It was found very soon after the first radio spectrograph was built by Wild and McCready (1950), that observed radio spectra can be divided to relatively little number of distinct basic types according to shapes they form in frequency–time plane. Several of these types were interpreted later and it was shown, that each type is caused by specific process in the solar corona, and thus such classification is not only morphological but has deeper physical meaning.

Type III and type II bursts Type III (or its counterpart on decimetric range — Fast Drift Burst) and type II bursts represents two typical examples from this classification. They are unambiguously interpreted now, at least what concerns of processes changing physical parameters in local frame of radio source (see Wild 1950; Ginzburg & Zheleznyakov 1958, and Mc Lean & Labrum 1985 and references therein). An example of type III spectrum is shown on Fig. 4.1. It consists from nearly vertical narrow lines. Such a high frequency drift[1] indicates very rapid changes of parameters influencing radiation as seen by the source. Since instantaneous spectra show only narrow emission lines and estimated brightness temperature reaches values up to 10^{12}K there is no doubt that radio radiation is cased by plasma emission. Thus the relevant parameter rapidly changing in the source reference frame is the electron density. Provided some model of the distribution of the electron density in the corona (e.g. Newkirk 1967, Saito 1970) such time variation is naturally explained by movement of the source through the solar atmosphere. The speed of the source determined using models referenced above is of order 10^5km s^{-1} and corresponds well with the speed of particles (especially electrons) accelerated during solar flares (see the section 1.2.2). Such fast (charged) particles can radiate by plasma emission as shown in the Chapter 3 and, thus to conclude, type III burst can be interpreted as plasma radiation of accelerated particle beam travelling through the solar atmosphere.

Type II burst (see Fig. 4.2) shows much less value of frequency drift on the other hand, indicating more slow changes of source local parameters. High brightness temperature and relatively narrow bandwidth of the instantaneous emission favour plasma radiation mechanism, again. Thus, supposing source moving through the solar

[1] The frequency drift is defined as the change of frequency of the emission line per unit time

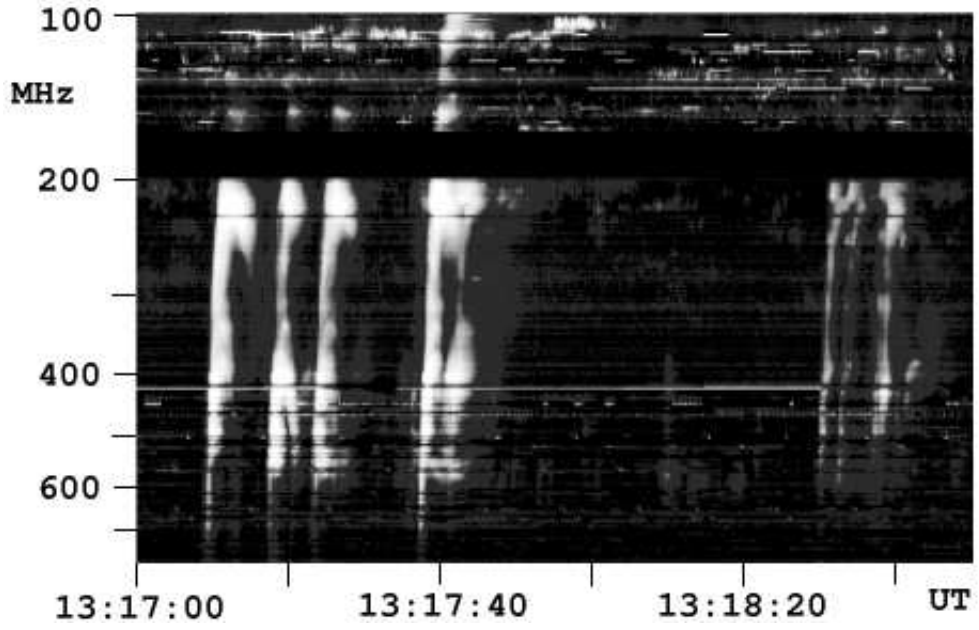

Fig. 4.1: Type III solar radio burst observed at Tremsdorf Observatory, Germany on May 17, 1999 (see `OSRA Tremsdorf homepage`).

corona similarly as in case of type III burst, the velocity of the source corresponding to observed frequency drift is of order 10^3km s^{-1}. Such value was also confirmed by position measurements and corresponds with the speed of MHD shocks. Although details of the emission mechanism are still unclear and there are several competitive proposals (`Ginzburg & Zheleznyakov 1958; Zaitsev 1966; Melrose 1975`), the type II burst is commonly interpreted as a radiation from moving shock wave as suggested already by Uchida (`1960`) and Wild (`1962`).

A lot of types of bursts, mainly on metric wavelengths have already been interpreted this way, however sometimes not unambiguously. Such interpretation of radio spectra is meaningful itself for understanding processes in solar flares, moreover it yields us a set of diagnostic tools. Some essential physical parameters of solar atmosphere such as magnetic field strength, density or temperature can be estimated at the source position measuring frequency of emission lines, their frequency drift or decay time at given frequency channel, especially if corresponding position measurements are supplied.

Nevertheless, not all of radio spectra have been explained up today, and even further new types were recognised since the capabilities of spectrographs had enhanced. It concerns especially of bursts in the decimetric range, formerly considered as structure-less. Since the primary energy release sites in solar flares are supposed to have local plasma frequency just in this band, interpretation of decimetric bursts aimed to obtaining new diagnostic tools is very important. In the following, two types of the decimetric radio bursts are studied: the recently discovered burst with rapid frequency variations — lace burst, and narrow-band decimetric spikes.

4.1 Lace burst

The Ondřejov radiospectrograph operating in the 0.8-2.0 GHz frequency range recorded in recent years (1998-2000), three (August 8, 1998; August 17, 1999; June 27, 2000) unique bursts with rapid frequency variations lasting for several minutes. They were recognised as a new type of decimetric radio emission and called "lace bursts". On August 17, 1999, the same burst was recorded simultaneously by the Brazilian Solar Spectroscope in the 1.0-2.5 GHz frequency range.

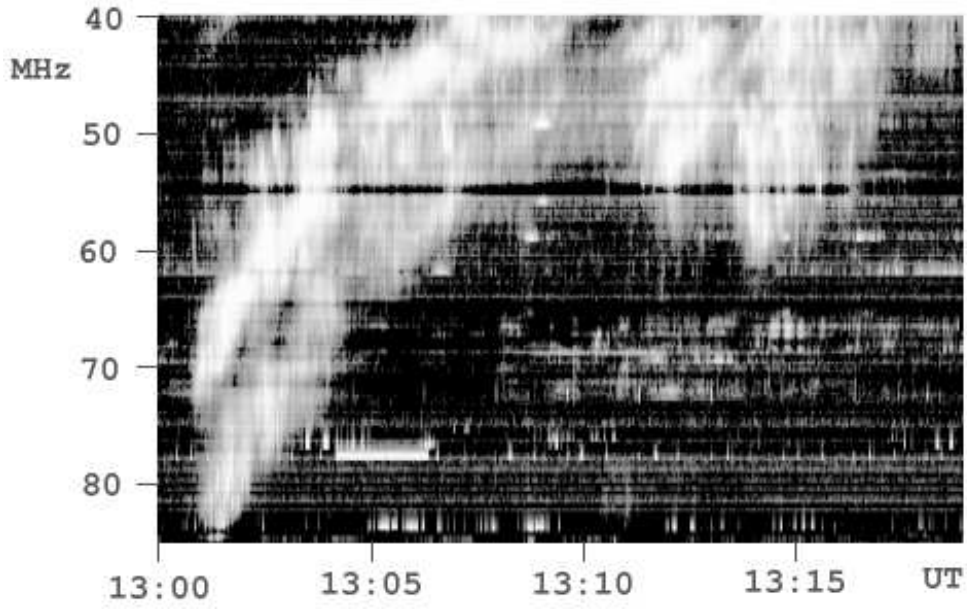

Fig. 4.2: Dynamic spectrum of type II solar radio burst observed at Tremsdorf Observatory on October 22, 1999 (`OSRA Tremsdorf homepage`)

The frequency variations of these bursts in four time intervals were studied using the Fourier analysis. Power-law spectra with spectral indices close to -2 ranging over the 0.01-3.0 Hz interval were found. Such spectra indicate fast changes of plasma parameters caused by turbulent state inside the radio source.

Since lace bursts do not show any global drift on dynamic spectra one can imagine that reducing turbulence in the source would lead to line emission on nearly constant frequency. Due to the similarities in the line features of these bursts with zebra pattern lines, a model similar to that of the zebra pattern was suggested (see also paper by Karlický et al. (`2001`)). The artificial radio spectra, computed using this model with a turbulent state of the solar flare atmosphere, are similar to those observed by the radiospectrographs. Provided that this interpretation of lace bursts is correct, there is unique opportunity to direct studies and diagnostics of turbulent flaring region for the first time.

4.1.1 Observations

Examples of bursts with rapid frequency variations (because of their appearances called also "lace bursts" - see `Jiřička et al. 2001`) in the range above 1 GHz were shown in the catalogue of the Brazilian Solar Spectroscope (`Sawant et al. 2001`). Similar fine structures can be recognised in Figs. 26 and 29 of the 1–3 GHz catalogue of Isliker & Benz (`1994`). From 1992 to 2000 the radiospectrograph at the Ondřejov Observatory (`Jiřička et al. 1993`, `Ondřejov solar radiodata webpage`) recorded 681 radio events in the frequency range of 0.8-2.0 GHz exhibiting various fine structures. In three cases only (August 10, 1998; August 17, 1999; and June 27, 2000), radio bursts with rapid frequency variations (the changes are of the order of fractions of seconds) were observed. In one case (August 17, 1999) the burst was observed also by the BSS, but the others could not be confirmed due to lack of observations on the respective dates.

An example of a burst with rapid frequency variations (lace burst), observed on August 17, 1999

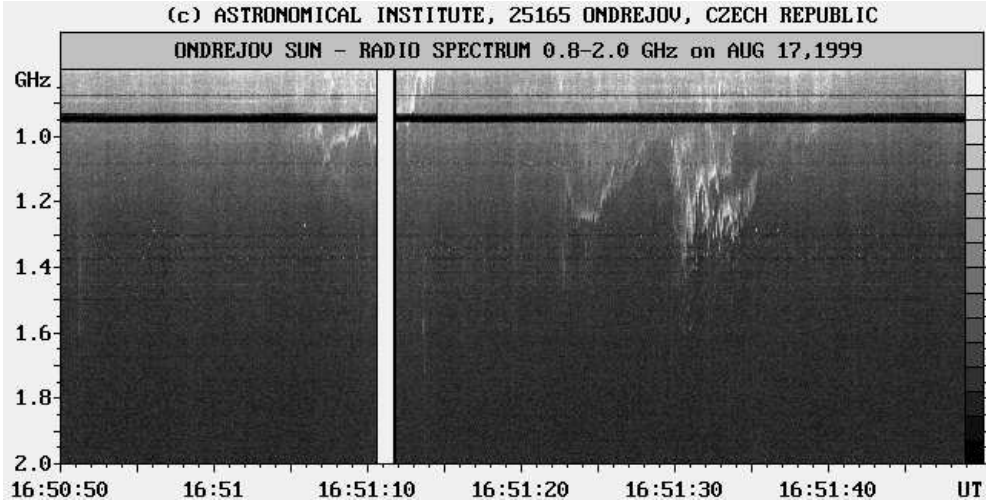

Fig. 4.3: The burst with rapid frequency variation observed in August 17, 1999 at 16:50:50 – 16:51:50 UT by the 0.8-2.0 GHz Ondřejov radiospectrograph (`Ondřejov solar radiodata webpage`).

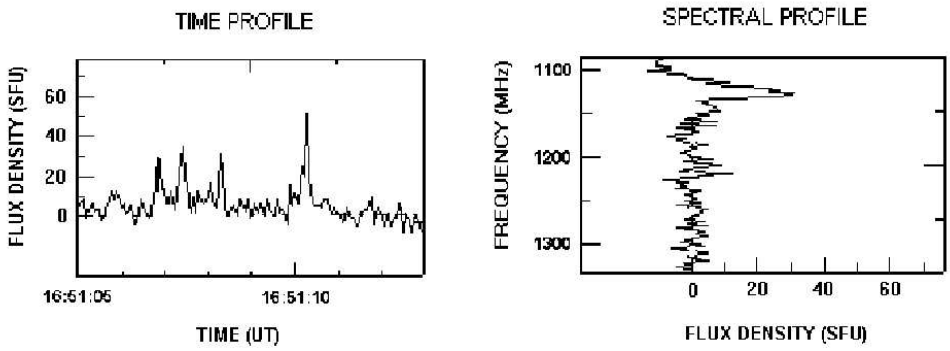

Fig. 4.4: The time profile on 1.11 GHz and instantaneous spectrum at 16:51:07 UT of August 17, 1999 event.

by the Ondřejov radiospectrograph, is shown in Fig. 4.3. The burst appears usually as a very narrow-band (about 50 MHz) line with strongly variable frequency and intensity. These lines are sometimes, especially at their low-frequency ends, mutually superimposed and accompanied by continua, forming thus a lace burst in the radio spectrum. The frequencies and intensities change in fractions of second - see Fig. 4.4, where the time and frequency profiles of one burst line are shown (compare with the radio spectrum - Fig. 4.3).

In other cases, especially in those lasting longer, these bursts are even more complex, with lines and continua mutually superimposed, giving thus the impression that they correspond to different radio sources (Fig. 4.6, upper part). These complex structures can also be seen in Fig. 4.5, where the time (1 minute interval) and frequency profiles of the radio spectrum (see also Fig. 4.6, upper part) are depicted. For example, the simple peak at 15:08:15.5 UT lasts about 1.3 s and its bandwidth is about 140 MHz. On the other hand, the time profiles of other peaks are more complex, e.g. at 15:08:00-15:08:04 UT.

In all the three observed events these bursts are part of long lasting pulsations in the 0.8-2 GHz frequency range. The flare activity associated with these bursts is summarised in Table 4.1.

		Aug. 10, 1998	Aug. 17,1999	Jun. 27, 2000
GOES	Start	8:35	14:28	12:40
	Max	8:40	16:02	12:55
	End	8:42	17:54	13:21
	Class	B7.6	C5.9	C9.3
H_α	Start	8:35	15:05	12:49
	Max	8:40	15:22	12:54
	End	8:54	16:34	13:42
	Importance	SF	SF	2N
	Position	S23W18	N24E37	S17E48
	NOAA AR	8293	8668	9062
Radio 1–2 GHz	Start	8:45	14:47	12:52
	End	9:19	17:04	13:04

Tab. 4.1: The basic characteristics of flares during which the lace bursts were observed (all times are in UT)

4.1.2 Data analysis

From the three observed bursts, four long-lasting (several minutes) time intervals (see Table 4.2) were selected for analysis. The example of one selected part (August 17,1999, 15:07:30 – 15:08:30 UT) is shown in Fig. 4.6, where in its bottom part the line corresponding to the high-frequency boundary of the burst is drawn. The high-frequency boundary defines frequency of the instantaneous radio emission best way because of its sharpness. Obtained frequency variations are then analysed by the Fourier method. The results for the four selected intervals from Table 4.2 are shown in Fig. 4.7. For comparison, straight lines expressing slopes corresponding to the best fitted power-law indices (see Table 4.2) are added. All the found power-law indices are close to -2. The Fourier power spectra show the presence of frequency variations ranging over the interval of about 0.01-3.0 Hz. According to plasma emission model considered here as a radiation mechanism it is supposed that these variations correspond to changes of plasma parameters (electron density, magnetic field strength) in the radio source.

Part	Date	Start [UT]	Duration [s]	Freq. Range [Hz]	Power-law Index
a	Aug. 10, 1998	08:51:59	120	0.008-5	-2.00 ± 0.04
b	Aug. 10, 1998	08:59:50	120	0.008-5	-1.91 ± 0.04
c	Aug. 17, 1999	15:01:00	300	0.003-5	-1.88 ± 0.03
d	Aug. 17, 1999	15:07:00	120	0.008-5	-2.13 ± 0.04

Tab. 4.2: List of analysed parts of the bursts with the frequency variations, Fourier frequency ranges, and Fourier power-law indices.

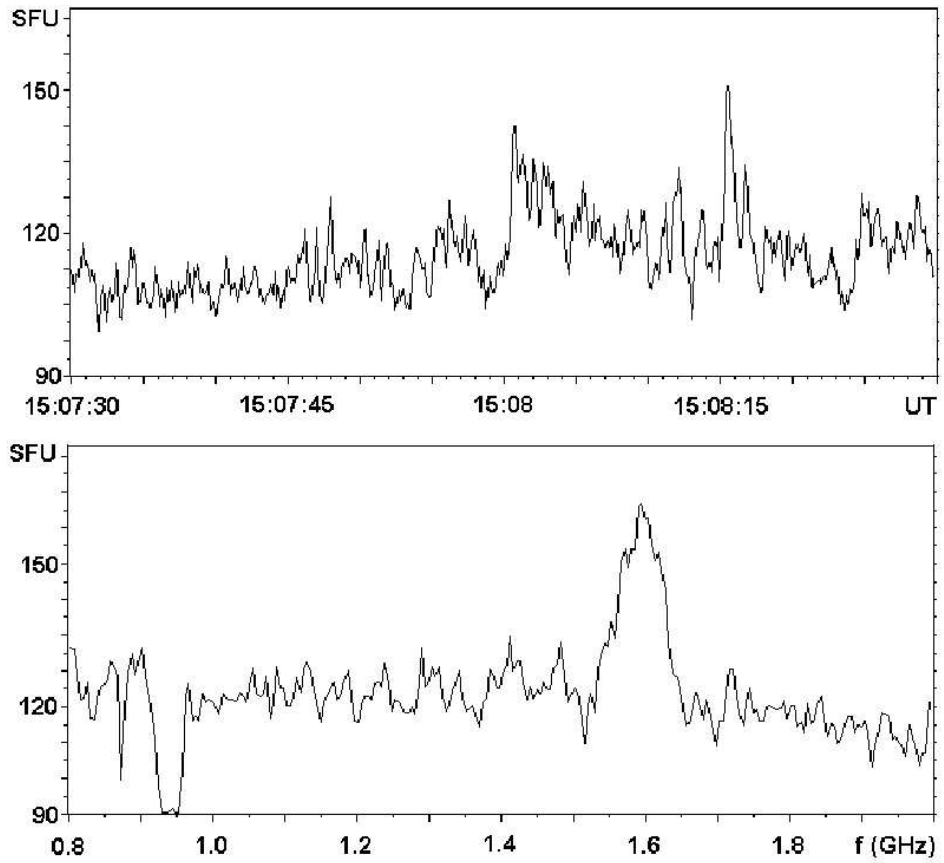

Fig. 4.5: The time profile on 1.6 GHz and the instantaneous spectrum at 15:08:15.5 UT of August 17, 1999 event.

4.1.3 Model radio spectrum

Basic ideas The very narrow bandwidth of the burst lines indicates the strong resonance process. Thus some kind of plasma emission is required as a radiation mechanism. Since the lace bursts are (especially in the case of low level of turbulence in the source) similar to individual zebra lines, the concept of "double resonance" used for zebra patterns by Zheleznyakov & Zlotnik (1975) and Ledenev et al. (2001) was suggested as elementary radiative process. As seen in the chapter 3 plasma emission requires the electron distribution function to be unstable for some wave mode. In the double-resonance concept the loss-cone distribution or the bi-Maxwellian function with $T_{||} \ll T_{\perp}$ are unstable with respect to upper-hybrid waves growth. In the realistic case of Maxwellian distribution function perturbed by bi-Maxwellian beam with relative electron density $\alpha = n_{beam}/n_0$ the growth rate of the instability can be expressed as (see Mikhailovski 1975, c.f. also eq. 3.66):

$$\gamma(\mathbf{k}) = -\frac{\sqrt{\pi}\alpha\omega^3}{v_{Te||}^3 \mathbf{k}^2 \mid k_{||} \mid} \times \sum_{s=-\infty}^{\infty} \left(I_s \exp(-z_{\perp}) \exp\left[-\left(\frac{\omega - k_{||}v_{||} - s\omega_{Be}}{k_{||}v_{Te||}} \right)^2 \right] \times \left[\omega - k_{||}v_{||} - s\omega_{Be}\left(1 - \frac{T_{||}}{T_{\perp}}\right) \right] \right), \qquad (4.1)$$

where $v_{Te||}$ is the thermal electron velocity along the magnetic field, $\mathbf{k}$ is the wave vector, $I_s(k_{\perp}v_{\perp}/\omega_{Be})$ is the modified Bessel function, $z_{\perp} = k_{\perp}^2 k_B T_{\perp}/m_e\omega_{Be}^2$, m_e is the electron mass,

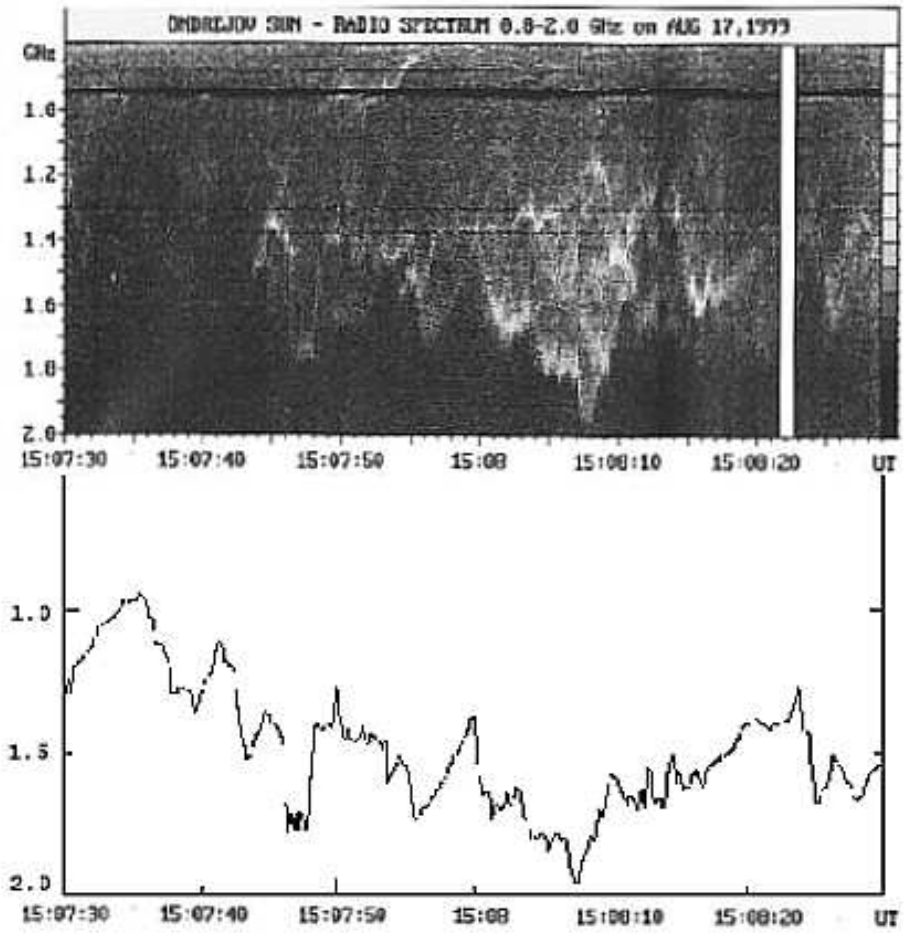

Fig. 4.6: The burst with rapid frequency variations observed in August 17, 1999 at 15:07:30 – 15:08:30 UT by the 0.8-2.0 GHz Ondřejov radiospectrograph (top) and the corresponding high-frequency boundary outline (bottom).

$k_\perp$ is the transverse component of the wave vector, and

$$\omega(\mathbf{k}) = \sqrt{\frac{\omega_{UH}^2 + \sqrt{\omega_{UH}^4 - 4\omega_{Be}^2\omega_{pe}^2 \cdot \frac{k_\parallel^2}{k_\parallel^2+k_\perp^2}}}{2}} \tag{4.2}$$

is the real-part of the frequency of generated waves. Let us note, that such the anisotropic beam can be easily developed by expansion of hot plasmas into colder environment along magnetic field lines, as described in paragraph "Anisotropic beam formation" below. It can be seen that the growth rate is inversely proportional to $k_{||}$. Such a way the most effectively excited longitudinal waves are for $k_{||} \ll k_\perp$. Thus, the resonance condition can be expressed as

$$\omega_{UH} = (\omega_{pe}^2 + \omega_{Be}^2)^{1/2} = s\ \omega_{Be}, \tag{4.3}$$

where ω_{UH}, ω_{pe}, and ω_{Be} are the upper hybrid, electron plasma and cyclotron frequencies, and s is the integer harmonic number. Unstable waves are thus generated only in the vicinity of

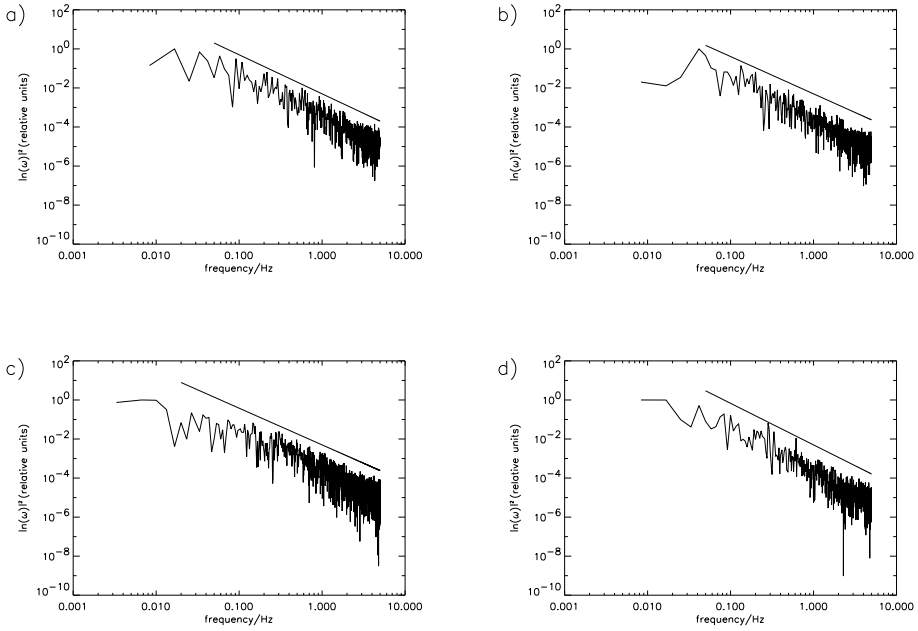

Fig. 4.7: The Fourier spectra of four selected parts (Table 4.2) of the bursts with the rapid frequency variations. Straight lines correspond to the best fitted power-law indices.

places, where the resonant condition (4.3) is at least approximately fulfilled.

According to the plasma emission model the generated upper-hybrid waves are then transformed into the electromagnetic ones. This rather phenomenological model aimed to qualitative interpretation of observed burst does not deal with wave conversion, instead of that it is simply supposed, that radio flux is proportional to the upper-hybrid wave energy and the emitted frequency $\omega_{elmg} \approx \omega_{UH}$. An attempt to estimate the conversion efficiency on the background of the MHD turbulence will be made further in the Chapter 5, section 5.2.

Processes described above are assumed to be running in the MHD turbulent plasma. The turbulence in the source changes values of eigen-frequencies of plasmas ω_{UH}, ω_{pe}, and ω_{Be} shifting such a way the point, where resonance condition (4.3) is matched, chaotically over the source region. The situation is schematically depicted by Fig. 4.16.

Anisotropic beam formation As mentioned above, the beam with the temperature anisotropy $T_{\parallel} \ll T_{\perp}$ can be formed by a propagation of electrons along magnetic field lines with the strength of B_0. Here, an expansion of a hot electron gas from a localised region to relatively cold surrounding plasma was studied solving the linearized Vlasov equation for the electron distribution function in the form

$$\frac{\partial f}{\partial t} + \mathbf{v} \cdot \frac{\partial f}{\partial \mathbf{r}} - \frac{e}{m_e} \cdot (\mathbf{v} \times \mathbf{B}_0) \cdot \frac{\partial f}{\partial \mathbf{v}} = 0. \tag{4.4}$$

In the present approximation the electric field caused by propagating electrons is neglected as well as a possible return current. An initial electron distribution function was chosen as

$$f(\mathbf{r}, \mathbf{v}, t = 0) = n_0 \left(\frac{m_e}{\pi E_{th}(\mathbf{r})} \right)^{\frac{3}{2}} \exp \left(\frac{-m_e v^2}{E_{th}(\mathbf{r})} \right), \tag{4.5}$$

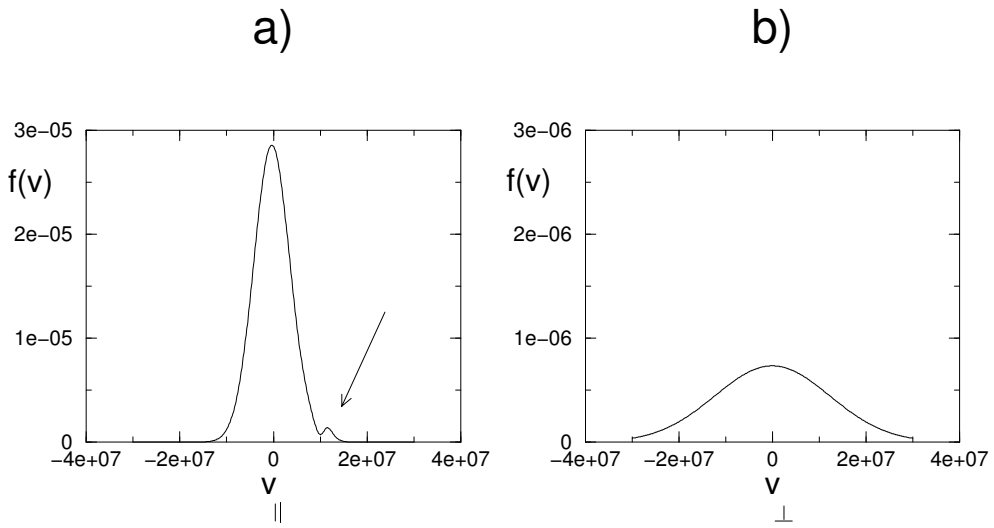

Fig. 4.8: The beam formed by a propagation of hot electrons along the magnetic field lines: **a)** the electron parallel velocity distribution for $v_\perp = 0$ m s^{-1}, and **b)** the electron perpendicular velocity distribution for $v_\parallel = 10^7$ m s^{-1}. All quantities are displayed in SI units.

where

$$E_{th}(\mathbf{r}) = 2k_B \left[T_c + (T_h - T_c) \cdot L(\mathbf{r})\right]$$

and the localisation function

$$L(\mathbf{r}) = \frac{a^2}{a^2 + x^2} \otimes 1(y) \otimes 1(z)$$

describes the 1-D temperature distribution over the hot region, T_h and T_c are the electron temperatures of hot and cold plasmas, respectively. Such an initial distribution simply represents a slab of the hot plasma (with the characteristic thickness a) surrounded by a colder environment. The equation (4.4) can be easily solved using the transformation to the Lagrangian coordinates. The result is:

$$f(x, v_\parallel, v_\perp, t) = n_0 \left(\frac{m_e}{\pi E_{th}(z - v_\parallel t)}\right)^{\frac{3}{2}} \times \exp\left(\frac{-m_e v^2}{E_{th}(z - v_\parallel t)}\right), \tag{4.6}$$

where $v_\parallel \equiv v_x$ is the velocity component parallel to the magnetic field $\mathbf{B}_0$. The results are shown in Fig. 4.8. The part a) represents the cut of the electron distribution function along the $v_\parallel$ for $v_\perp = 0$. An arrow points to the beam formed. The part b) shows the cut of the electron distribution function along the $v_\perp$ for $v_\parallel = 10^7$ m s^{-1}, which is near the centre of the beam parallel velocity distribution. The temperature anisotropy of the beam can be seen. Both cuts were made for $x = 10^7$ m and $t = 1.0$ s. The temperatures of hot and cold plasmas are 10^6 K and 10^7 K, respectively, and the width of the hot region is $a = 10^6$ m.

The model Based on these ideas the following simplified model was built: Provided that shortest time-scale of chaotically varying plasma parameters is much longer than typical growth time of unstable waves, the saturated state is reached and the instability can be described as

two oscillators with frequencies ω_{UH} and $s \cdot \omega_{Be}$, coupled by positive feedback. Then, the time evolution of the electric field $\mathbf{E}$ in upper hybrid oscillations can be described by equation

$$\frac{\mathrm{d}^2\mathbf{E}}{\mathrm{d}t^2} + \nu\frac{\mathrm{d}\mathbf{E}}{\mathrm{d}t} + \omega_{UH}^2\mathbf{E} = C\cos(s \cdot \omega_{Be}t), \tag{4.7}$$

where coefficient C describes a measure of coupling between oscillators and ν is the damping of the upper hybrid waves. As a foregoing remark let us note, that the more general approach for arbitrary fast plasma parameters changes is presented in section 4.2.2.

Solving equation (4.7) for $\mathbf{E}$ assuming solution in the form $\mathbf{E}(t) = \mathbf{E}_0 \cdot \exp(i \cdot s\omega_{Be}t)$ the resulting radio flux F should be

$$F \propto \frac{1}{(\omega_{UH}^2 - s^2\omega_{Be}^2)^2 + \nu^2 s^2 \omega_{Be}^2}, \tag{4.8}$$

where the flux proportional to the square of modulus of complex amplitude $\mathbf{E}_0$ of the upper hybrid waves is assumed. It is clear from this formula, that flux has maximum when resonance condition (4.3) is exactly fulfilled, and strongly decreases to zero, as frequency mismatch become important.

The processes are considered in a 1-D source model with the stationary mean electron density decreasing slowly in space as

$$n(x) = n_0\left(1 - \frac{x}{L}\right), \qquad x \in (0; L)$$

and the magnetic field in the solitary magnetic flux-tube as:

$$B(x) = B_0\left(1 - \frac{x}{\sqrt{x^2 + b^2}}\right).$$

Here parameters L and b with dimensions of length represent typical scales on which the magnetic field B and the electron density n vary. Then, on this stationary mean density profile the chaotically varying (in space and time) density and magnetic field perturbations are superimposed. Perturbed frequencies ω_{UH} and ω_{Be} are computed at fixed time t at each point x of the source and using formula (4.8) also contributions to the radio flux in relative units are also determined. Contributions to the flux from each element of the source are divided into frequency channels according to radiation frequency ω. This frequency is given by frequency of the forcing, i.e. $\omega = s \cdot \omega_{Be}$. Contributions to the flux, belonging to an appropriate channel are integrated over the source length. Thus, the instantaneous spectrum at given fixed time is obtained. Repeatedly using this algorithm for subsequent times whole artificial dynamic spectrum is computed.

The image of the source just presented here corresponds well to the reconnection out-flow jet in solar flare (c.f. section 1.2.2). The turbulence is easily produced by the material expelled from reconnection at high speeds in such jets, and the anisotropic electron beam can be constituted either by propagation of the "hot" electrons from reconnection core along the field lines or by other acceleration mechanism considered in reconnection process (i.e. acceleration by waves or by electric field). Thus, it can be believed, that the lace burst represents the radio manifestation of the turbulent processes in the reconnection out-flow jets (see Fig. 4.14).

4.1.4 Modelled to observed data relation

Using this model, the artificial radio spectrum, showing one burst line with the rapid frequency variation, was computed (Fig. 4.10). Parameters used in this case are: $n_0 = 3 \times 10^{16} m^{-3}$, $B_0 =$

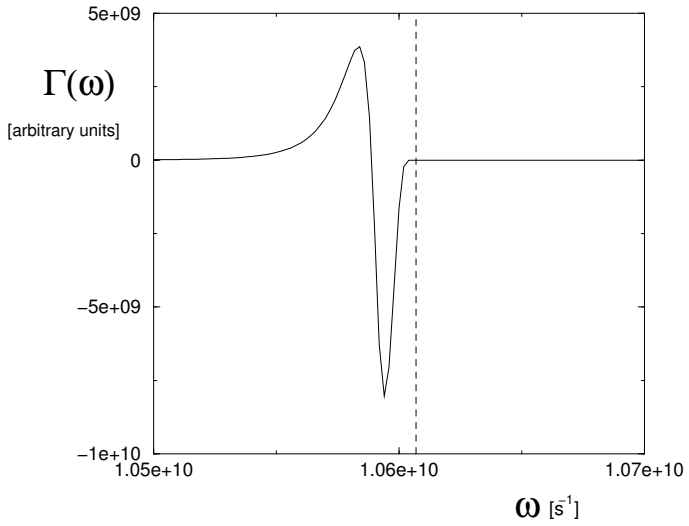

Fig. 4.9: The growth rate of the double-resonance instability vs. the angular frequency of generated waves. Formulae (4.1) and (4.2) were used to construct this illustrative picture. The following parameters were considered:$\omega_{pe} = 10^{10}s^{-1}, \omega_{Be} = 3.53 \times 10^{10}s^{-1}, T_{||} = 10^3K, T_{\perp} = 10^7K, s = 3$. The relative frequency mismatch $\Delta\omega = |\omega_{UH} - s \cdot \omega_{Be}|/\omega_{UH}$ was 10^{-3}, dashed vertical line indicates position of the upper-hybrid frequency ω_{UH}. Negative values of the growth rate corresponds to collision-less (Landau-like) absorption.

$0.02T, L = 1 \times 10^6m, b = 5 \times 10^5m$. The radio emission is considered on the $s = 4$ harmonic. The magnetic field variations are set to zero, the density variations have the following spatial characteristics: a) the power spectrum is a power-law function with the power-law index -2 for the wave numbers greater than $5 \times 10^{-7}m^{-1}$, b) the r.m.s. of the density perturbation is $0.1n_0$, and c) the phases are random. For the sake of simplicity these density variations are assumed propagating coherently with the out-flow speed $v_{outflow} = 1.0 \times 10^5ms^{-1}$ through the flaring atmosphere. Rather high gradients of the electron density and magnetic field were chosen with respect to considered source location inside reconnection jet (see Fig. 4.14).

Comparing this modelled radio spectrum with the lace burst of August 17, 1999 at 16:51:06-16:51:12 UT (Fig. 4.6 upper part), similarities between the two spectra are evident.

Figure 4.11 shows comparison between complex lace burst and corresponding zebra pattern artificial spectra, both obtained using this model. For the lace burst the same parameters as in case of spectrum in Fig. 4.10 were used, complexity is reached by simultaneous radiation on three harmonics: s=3, 4 and 5. The zebra pattern was for comparison computed the same way, only the density turbulence was reduced to zero.

It is clear, that the modelled and observed spectra are similar for the first look. Moreover, there are other evidences in favour of this model:

- The diffusion observed on low-frequency side of emission lines is clearly seen on observed data in contrast with the high-frequency cut-off. However not presented on modelled spectra as a consequence of symmetrical line profile (see formula (4.8)) used in this rough approach, it can be explained on the basis of expression (4.1) for the upper-hybrid waves growth rate. The last term in brackets ensures, that growth rate is positive only if the frequency of generated waves is less then some critical frequency (slightly less then cyclotron frequency, depending on amount of temperature anisotropy). See Fig. 4.9 for further explanation.

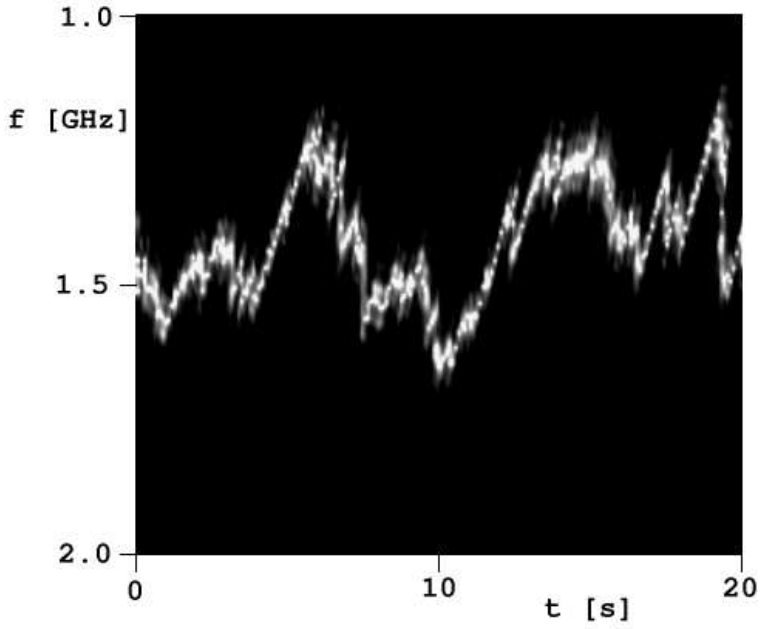

Fig. 4.10: The modelled spectra of the bursts with the rapid frequency variations.

- As seen on Fig. 4.11 complexity of the lace burst can be easily reached by simultaneous radiation on several harmonics. Multiple sources along various field lines with slightly different conditions represent the other possibility.
- It is commonly believed in physics, that complex variety of observational facts can usually be explained by essentially lower number of basic physical processes. Such an idea, however somewhat speculative, supports presented model since it naturally unifies two (even at least three – see the section 4.2.2) types of observed bursts.

The model explains all observed features of the lace bursts and conditions needed for this radiation mechanism to work are also consistent with the standard image of flaring atmosphere (Fig. 4.14). Thus, it can be considered as a correct and its consequences can be used for plasma diagnostics.

4.1.5 Plasma diagnostics using the model

According to the model it is for the first time we have an opportunity of the direct analysis of turbulent processes in solar flares. Very useful tools for such an analysis are the Fourier power spectra of the emission frequency changes such as in Fig. 4.7. As the static electron density variation is much more flatten along the field line then magnetic field strength, observed frequency changes are mainly due to electron density perturbation. For small perturbations the relation

$$\frac{\Delta n}{n_0} = 2\frac{s^2}{s^2-1}\frac{\Delta f}{f}$$

derived differencing the resonance condition (4.3) is valid. Since for harmonic number $s \geq 3$ fraction $s^2/(s^2-1) \approx 1$, the power spectrum (the spectrum of the square of modulus) of the density perturbations is obtained from power spectrum of frequency changes Δf simply multiplying it by factor of 4 ($=2^2$).

From the power spectrum several kind of information can be obtained:

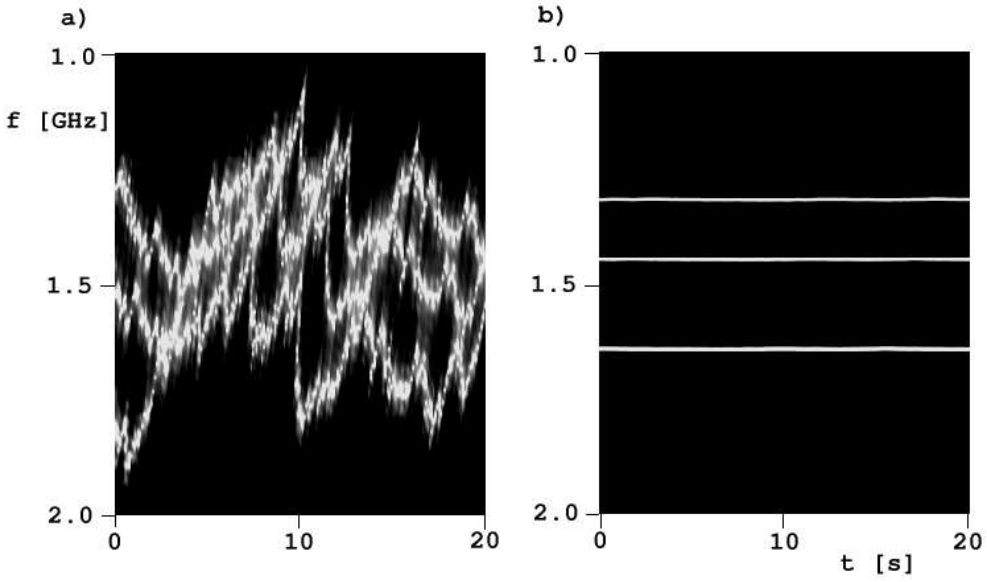

Fig. 4.11: Comparison between the lace burst (a) and zebra lines (b) modelled with the same set of static parameters. For the zebra lines the density turbulence r.m.s. was reduced to zero.

1. The turbulence level. It can be estimated from the power spectrum of the density perturbations provided, that essential part of its support is covered by data. There are two ways to make such an estimation:

   (a) According to Parsevals theorem the r.m.s. of density turbulence can be expressed as:

   $$\langle \Delta n^2(t) \rangle \equiv \frac{1}{T} \int |\Delta n(t)|^2 \mathrm{dt} = \frac{1}{\mathrm{T}} \int |\Delta \mathrm{n}(\omega)|^2 \mathrm{d}\omega$$

   with T beeing the lace burst total duration. Thus, integrating the power spectrum over its support the r.m.s. of density turbulence is computed directly.

   (b) Another way to estimate the turbulence level is fitting modelled to observed data. As mentioned above value of $\sqrt{\langle \Delta n^2(t) \rangle} = 0.1$ corresponds very well with radio measurements. Thus, supposing radio source of this burst in reconnection out-flows jet, the turbulence level at these jets can be estimated to this rather high value.

2. Another data that can be obtained from the Fourier analysis concern the typical length scales of out-flow jets. To make it possible, the time scale in observed power spectra have to be converted to the length scale some way. The most simple approximation for this purpose, used also for artificial spectra computation (see previous subsection), is the coherent propagation of chaotic structure along the field lines with the out-flow velocity. Then between wavenumbers k and frequencies ω the simple relation

   $$k = \frac{1}{v_{outflow}} \cdot \omega$$

   is straightforwardly derived. Now, the analogy with hydrodynamic turbulence in liquids will be used to make some estimations. The typical power spectrum of hydrodynamic turbulence in liquids (see Fig. 4.12) is well understood (`Sreenivasan 2000`). In log–log coordinates it can be schematically approximated by broken straight line. Maximum of this function corresponds to scale of energy input into the turbulent cascade and in case

of liquid flow inside a tube it roughly equals to the diameter of the tube. Thus, by the analogy such maximum, if found, in the power spectrum of density perturbations should correspond with the diameter of the jet confined by magnetic field in the source of the lace burst location.

3. Energetic balance of the recconection process can be studied in following way: From the maximum toward to shorter length scales the so called inertial range follows in fluid turbulence. The self-similarity law is valid in this region of length-scales and corresponding part of power spectrum is of power-law course (the linearly decreasing part in log–log graph 4.12). The inertial range is finished by rather sharp fall-off at length

$$L_c = \left(\frac{\epsilon}{\nu}\right)^{\frac{1}{4}}.$$

Here, ϵ is the energy dissipation rate (energy dissipated by mass unit per second) and ν is the kinematic viscosity. As dissipation in case of MHD turbulence works rather by resistivity than by viscous mechanism the kinematic viscosity ν should be replaced (see e.g. `Moffat 2000`) by magnetic diffusivity $\kappa = \eta/\mu_0$, where η is the (anomalous) resistivity and μ_0 the vacuum permeability, as usual. Thus, estimating some way the electric resistivity η, the energy dissipation rate is obtained provided that the dissipation scale can be determined from the power spectrum high-frequency cut-off. In the state of statistical equilibrium the energy input and dissipation in the jet equals and such the way the power converted to the jet kinetic energy in reconnection process can be estimated if: 1) observed energy dissipation rate can be considered as typical value over the jet and, 2) the characteristic volume of the jet is determined independently.

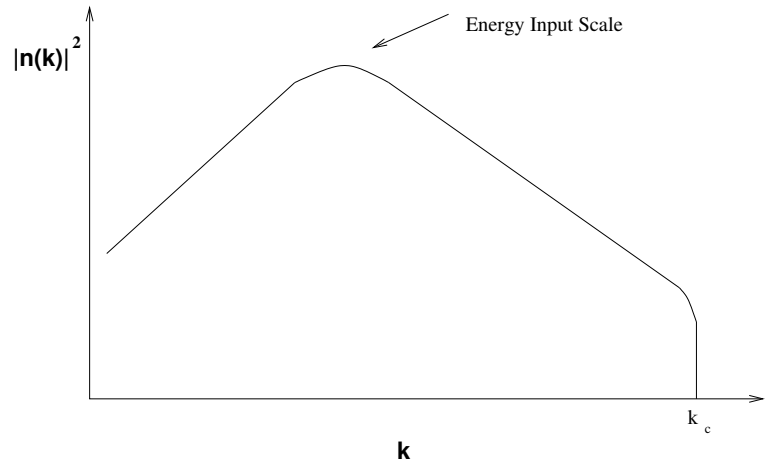

Fig. 4.12: The power spectrum of the hydrodynamic turbulence in log – log coordinates (schematically depicted).

It was clearly shown above, what powerful tools in plasma diagnostics the qualitative interpretation of radio burst and following analysis can yield. It can be believed in the particular case of the lace burst, that all such diagnostic possibilities have not been exploited yet. For example, the spectral index in the inertial range can tell us something about the dimensionality of the turbulent process, the correlation between individual lace lines seen on Fig. 4.11 if found on observed data will give information about advection in out-flow jet etc. Such still unrecognised methods as well as the verification of predictions made above should be subjected to future studies.

4.2 The decimetric spikes

The narrowband dm-spikes attract attention, mainly due to their exceptionally high brightness temperatures ($T_b \approx 10^{15}$ K) and their short durations (≤ 0.1 s, see the review by Benz (1986)). They have been studied in many papers (see for example Slotje 1981, Karlický 1984, Fu et al. 1985, Stahli & Magun 1986, Güdel 1990 or Aschwanden 1990) and two classes of models have been suggested: a) based on the plasma emission mechanism (e.g. Kuijpers et al. 1981, Tajima et al. 1990, Wentzel 1991, Stepanov et al. 1999), and b) based on the electron-cyclotron maser mechanism (e.g. Wu & Li 1979, Holman et al. 1980, Melrose & Dulk 1982, Vlahos & Sharma 1984, Winglee et al. 1988, Aschwanden 1990, Fleishman & Yastrebov 1994, Willes & Robinson 1996, Fleishman & Melnikov 1998).

In the recent studies by Karlický et al. (1996, 2000) the stratified atmosphere with certain scale heights was assumed. Authors then transformed the frequency scales into heights of the solar atmosphere and using a Fourier analysis they found the power-law spectra with power-law indices in the range of -0.80 – -2.85. Similar results were found also by Messmer & Benz (2000). In several events the power-law indices were close to -5/3, therefore it was suggested that the narrowband dm-spikes are generated by superthermal electrons in the MHD turbulence forming in the magnetic reconnection plasma out-flows (Karlický et al. 1996, Zlobec & Karlický 1998). Moreover, the statistical methods (see Schwarz et al. 1993) applied to spike events show that the spectral structure of spikes is not stochastic and that neighbouring spikes are correlated.

Summarising all these facts, a new model have to be built, since the models referred above, however successfully explaining the individual spike characteristics, do not take into account these global spectral properties at all. The correlation between individual spikes can be easily explained in terms of some kind of interrupted line emission. As turbulent spectra of electron density variations were found and high brightness temperature as well as narrow bandwidth manifest strong resonance processes, the same mechanism as in the case of lace burst was proposed – see also the paper by Bárta & Karlický (2001). The difference between these two types of bursts relies in presence of short time-scale turbulent variations in case of dm-spikes. This fast variations cause the emission interruption by means of nonlinear damping of upper-hybrid waves.

In the following, first, the structural features of the narrowband dm-spikes are summarised. Then their model is presented. Finally, examples of artificial radio spectra with narrowband dm-spikes are shown and global as well as individual spike properties are discussed with emphasis to model-observation relations.

4.2.1 An example of the narrowband dm-spikes

During the impulsive phase of the July 12, 2000 flare, superimposed on the broad-band drifting pulsation structure, a cloud of narrowband dm-spikes was observed (Fig. 4.13). Here, several features typical of narrowband dm-spikes can be seen: a) the spikes are clustered in time in broad-band pulses lasting several seconds, b) there are also clusters of spikes in the frequency bands (e.g. in the 1.3-1.6 GHz range), c) some spikes form drifting chains (see Fig. 4.13, the 1.0-1.3 GHz range, 10:34:20-10:34:50 UT), and d) after clouds of narrowband dm-spikes at 10:34:53-10:35:03 UT, a unique and very narrowband line was observed in the 1.20-1.34 GHz range. After this event, at 10:36:15-10:36:22 UT in the 1-2.6 GHz range the zebra pattern was observed. It is reminiscent of the well-known observations of 26 June 1978, presented in the paper by Kuijpers et al. (1981), where the spikes changed continuously into braided zebra patterns. Further observational facts concerning the narrowband dm-spikes can be found in papers by Benz 1986, Güdel & Benz 1990, Aschwanden et al. 1998, Fleishman & Melnikov 1998

and Meszárosová et al. 2000. For example, time profiles of individual spikes exhibit an exponential decay with rates in the range of the collisional plasma damping. Their polarisation is found in a broad range from non-polarised up to fully polarised events, and so on.

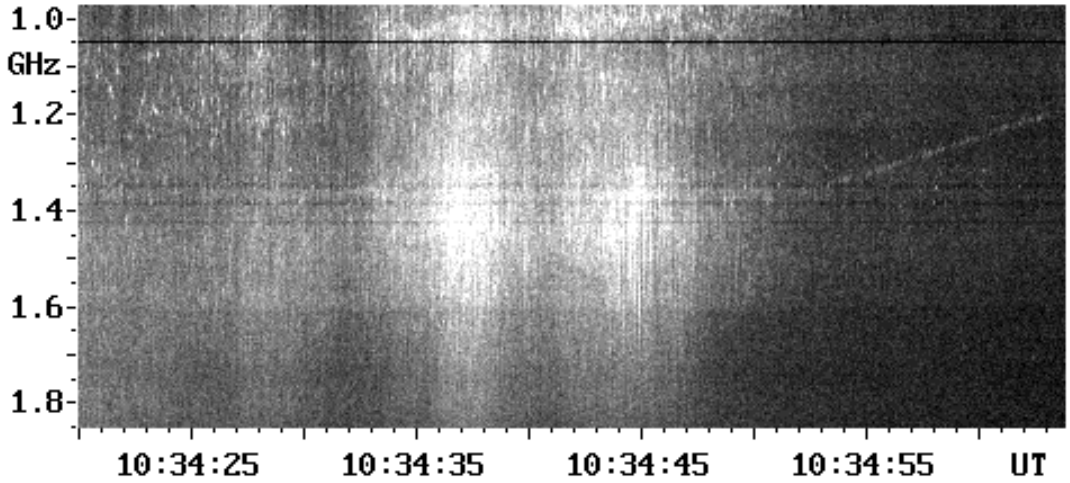

Fig. 4.13: The 1.0-1.8 GHz radio spectrum observed at 10:34:20-10:35:04 UT, July 12, 2000 by the Ondřejov radiospectrograph (Jiřička et al. 1993, Ondřejov solar radiodata webpage).

4.2.2 Model of the narrowband dm-spikes

Basic concept Due to a global structure of clouds of the narrowband dm-spikes (drifting chains and very narrowband lines, their clustering in the frequency bands, turbulent spectra of density variations etc. - see section 4.2.1) the same concept was adopted as for the lace burst in previous section 4.1 (see also paper by Karlický et al. (2001)). According to this approach the upper-hybrid waves are generated by instability of anisotropic beam in locations, where the resonance condition 4.3 is approximately fulfilled. The anisotropic beam is easily formed by propagation of electrons accelerated some way in the reconnection area along the field lines (see paragraph "Anisotropic beam formation" in the section 4.1). This instability is supposed to be running in the turbulent environment of reconnection out-flow jets (see Fig. 4.14).

The difference between the lace burst and the decimetric spikes according to this model is only in the presence of very fast variations of plasma parameters in case of dm spikes. These fast changes affects strongly the instability. Particularly, when their time-scales are comparable with the grow time of upper-hybrid waves, the instability can be totally suppressed. Under these circumstances the coupled-oscillators approximation (4.7) used for the lace burst modelling is no longer valid. Instead of that the time evolution of each wave mode in **k**-space have to be computed:

$$E(\mathbf{k}, t + \Delta t) = E(\mathbf{k}, t) \cdot \exp[(\gamma(\mathbf{k}) - \nu) \cdot \Delta t]. \tag{4.9}$$

Here ν designates the collisional damping of waves, independent of the wave vector and the growth rate $\gamma(\mathbf{k})$ is given by formula (4.1). Note, that according the formula the growth rate can be both positive or negative. The negative value represents Landau-like absorption of upper-hybrid waves that can stop the emission on given frequency channel very effectively. The described mechanism of radiation interruption is preferred here to quasi-linear relaxation of unstable distribution function proposed by other authors.

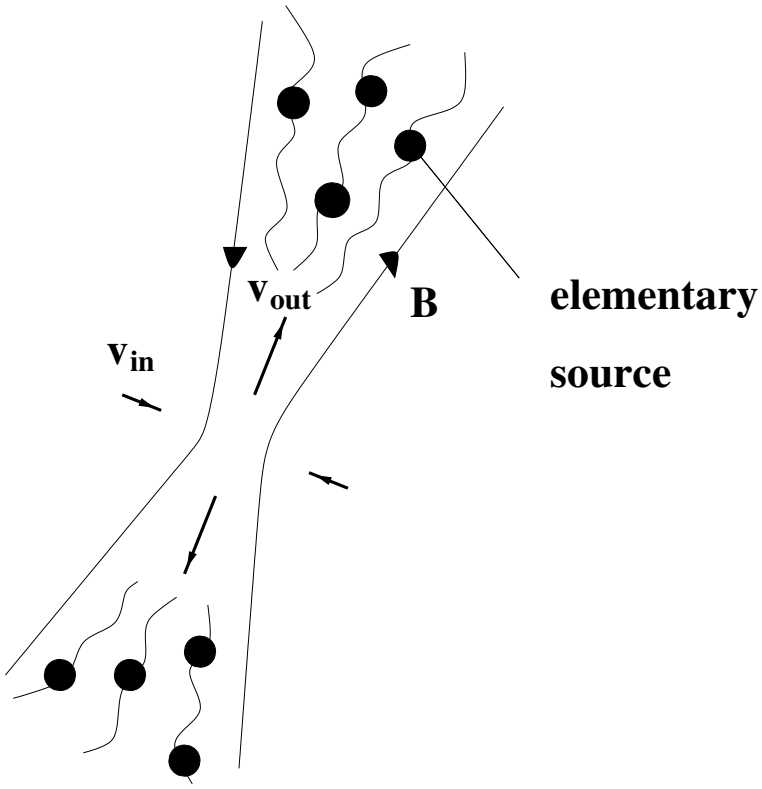

Fig. 4.14: The scenario of the lace burst or the narrowband dm-spikes generated in the plasma reconnection out-flows (cf. Fig. 1.10 in the Chapter 1).

Source model Suppose again, that the atmosphere in the source region (in the reconnection out-flow - see Fig. 4.14.) can be described as a bunch of solitary magnetic flux tubes, along which the magnetic field strength B and electron density n slowly decrease as:

$$n(x) = n_0 \left(1 - \frac{x}{L_N}\right), \qquad x \in (0; L) \tag{4.10}$$

$$B(x) = B_0 \left(1 - \frac{x}{\sqrt{x^2 + L_B^2}}\right). \tag{4.11}$$

Here parameters $L_B = B(dB/dl)^{-1}$ and $L_N = 2N(dN/dl)^{-1}$ are the characteristic scales of the magnetic field and electron density in radio sources and x is the length measured along the flux tube. The magnetic field strength and density at the base (x=0) of each flux tube B_0 and n_0, respectively, as well as scale parameters L_N and L_B are considered to be in some intervals for all the flux tubes.

As mentioned in the section 4.1, this type of model was used also for zebra pattern interpretation. In these models the radio sources of individual zebra lines are spatially separated. The distance between neighbouring levels of the resonance can be written (see `Zheleznyakov & Zlotnik 1975`):

$$\Delta l \approx \frac{L_B L_N}{s L_B - (s+1) L_N}, \tag{4.12}$$

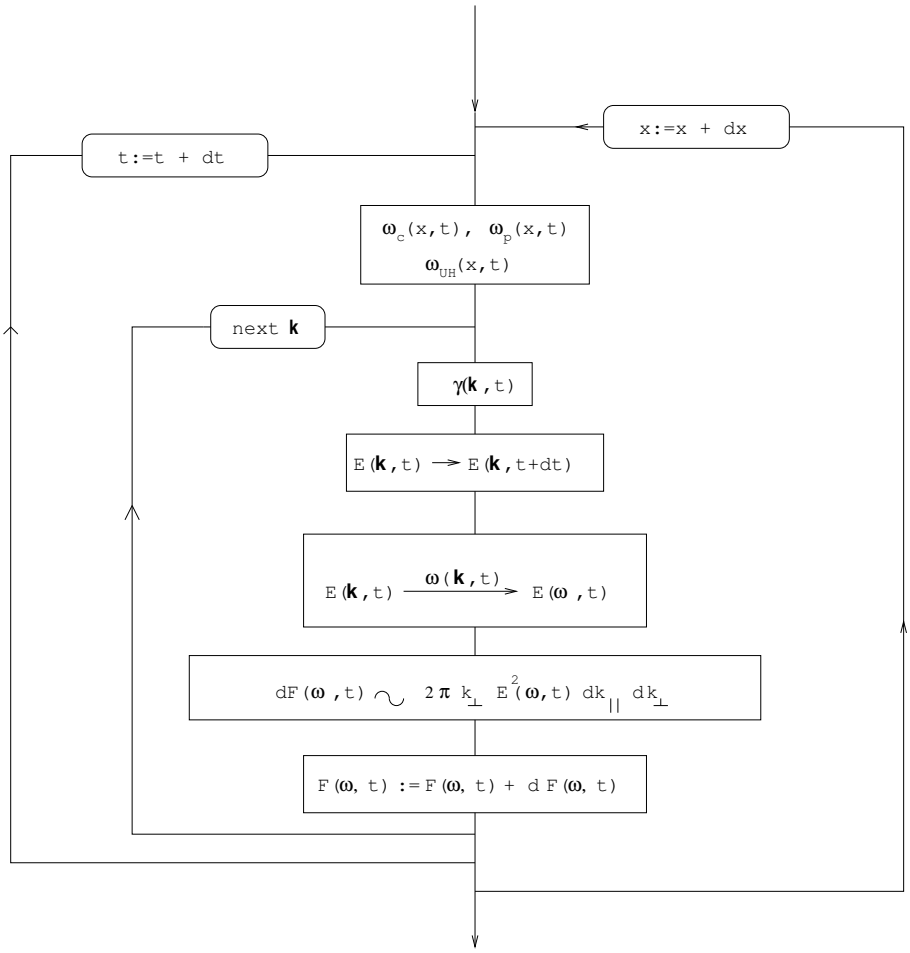

Fig. 4.15: The algorithm scheme used for computation of the radio flux from a single flux tube source.

Similarly, the frequency separation of zebra lines is

$$\Delta\omega \approx \frac{2s\omega_{Be}L_B}{\mid sL_B - (s+1)L_N \mid}. \tag{4.13}$$

Thus, when $L_B \gg L_N$ (a slow change in the magnetic field), $\Delta\omega \approx 2\omega_{Be}$. On the other hand, if $L_B \ll L_N$ (a fast change in the magnetic field) then $\Delta\omega \approx 2\omega_{Be}L_B/L_N \ll 2\omega_{Be}$. The last two formulae are used for the magnetic field determination. While Zheleznaykov & Zlotnik considered the case $L_B \gg L_N$, Ledenev et al. (2001) used the opposite case. Here, in accordance with Ledenev et al. , the case with $L_B \ll L_N$ is preferred because then (for small s) the estimated magnetic field is more realistic. Furthermore, as will be shown in the following, the separate s branches can explain the drifting chains of spikes and their clustering into some specific frequency bands.

On this stationary mean density profile the chaotically varying (in space and time) density and/or magnetic field perturbations are then superimposed. Due to these variations the positions, where the resonance condition (4.3) is fulfilled, move inside each magnetic flux tube. A schematic view of such a situation is shown in Fig. 4.16.
Assuming that the environment is optically thin except of strongly localised elementary sources (places, where the resonance condition (4.3) is matched), the total radio flux is simply the sum of contributions emitted by the length elements of each loop. First, for a fixed position on the

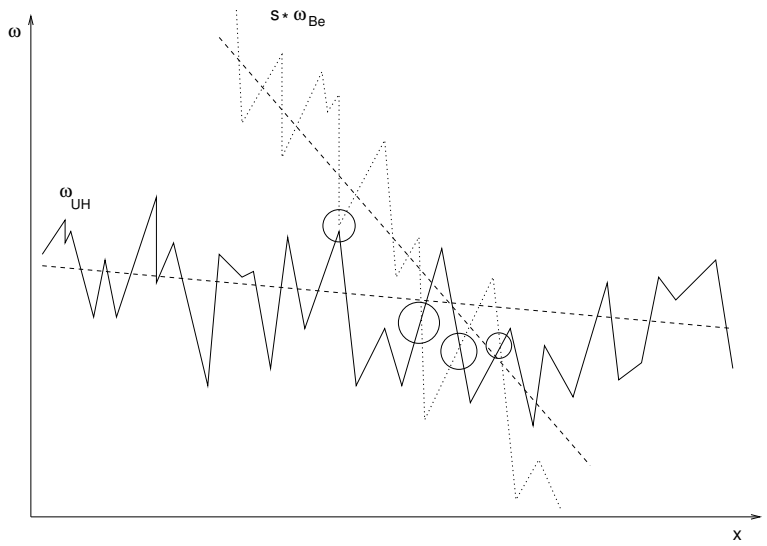

Fig. 4.16: A schematic picture of the double resonance in the turbulent radio source. The dashed lines show steady background values of the upper hybrid and one harmonic of the cyclotron frequencies along the source. The solid and dotted lines represent local values at a fixed time including the turbulent density and magnetic field perturbations. The small circles show the regions where the resonant condition (4.3) is fulfilled.

loop x and specific time t the local frequencies ω_{pe} and ω_{Be} are computed. Then using the relations (4.2) and (4.1) the frequency and growth rate of unstable waves are evaluated in each grid point of the 2-D k-space. The amplitude of these waves is computed using equation (4.9). The thermal level is used for the initial electric field value of the unstable upper hybrid waves. Due to nonlinear effects the instability under study needs to be saturated at a certain level. To simulate this effect the algorithm used ensures that when waves reach some chosen saturation level the appropriate wave mode does not grow further. Similarly, the energy of any wave mode does not decrease below the thermal level. The nonlinear process that causes saturation of the instability is not studied here in detail. Nevertheless, from the spacecraft measurement of the energy density of the Langmuir waves, observed during interplanetary type III bursts analysed by Thejappa & MacDowall (1998), the saturation level is estimated. Estimation gives for the amplitude of the electric field strength value 10^6 of the electric field strength corresponding to the thermal level wave energy.

There are two results of the presence of the MHD turbulence on the resulting radio emission: a) it chaotically changes the radio emission frequency, and b) the very fast plasma parameter changes in the radio source reduce or even stop the plasma instability under study. To simulate the latter effect, the time spent by each point of the source within the resonance is computed and when it becomes comparable or even less than the characteristic growth time, the instability is assumed to be not acting at all and, thus the growth rate is set to zero. This effect interrupts the radio emission.

The generated upper hybrid waves are then transformed to the observable electromagnetic waves. Here, for simplification, it is assumed that the frequency of spikes is $\omega_{elmg} \approx \omega_{UH}$ (the coalescence of the upper hybrid wave with some low frequency variations). Similarly as in the case of lace bursts (see the section 4.1 the wave transformation processes are not analysed in this phenomenological model. For details of standard transformation processes, see the paper by Zheleznyakov & Zlotnik (1975). An alternative estimation of transformation efficiency on the

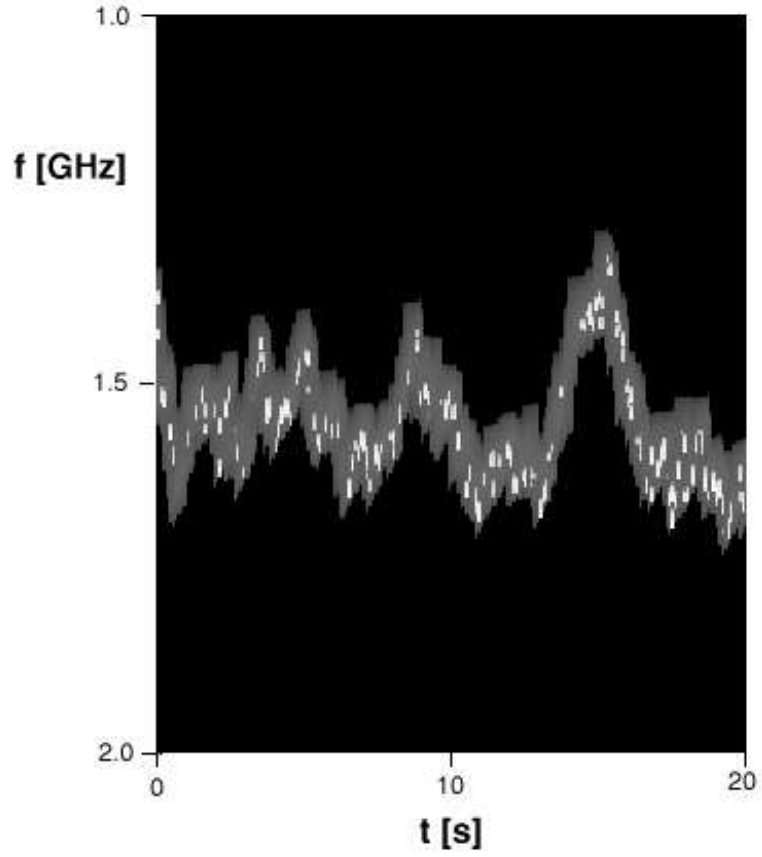

Fig. 4.17: The 1.0-2.0 GHz modelled radio spectrum of the chain of spikes. The radio flux shown is in a logarithmic scale.

background MHD turbulence is discussed in the section 5.2.
Here, for model purposes the radio flux is assumed to be proportional to the energy density of generated upper hybrid waves. Therefore the computed amplitudes of wave modes $E(\mathbf{k}, x, t)$ (for fixed times and positions) are squared and multiplied by a value of $k_\perp$ with respect to the cylindrical symmetry of the problem in the k-space. The obtained values for each mode are then sorted to frequency channels according to their frequencies (4.2). In the following step the time is increased ($t \rightarrow t + \mathrm{dt}$) and new values of the radio emission in specific frequency channels are evaluated in the same way. Repeatedly using this procedure, the dynamic radio spectrum for one elementary source at one given harmonic s is obtained. A full spectrum of the whole source is computed as the sum of elementary spectra. First, the spectra are integrated over the loop length, then contributions of all loops at one harmonic s are summed and, finally radio emissions of all considered harmonics are superimposed. The algorithm for a single flux tube source is schematically shown in Fig. 4.15.

4.2.3 Model – observations relation

Examples of the modelled radio spectra are shown in Figs. 4.17, 4.18 and 4.20. As notified above and discussed in the following, spikes radio sources are expected in the magnetic reconnection out-flows, where magnetic field gradients are probably higher then in the surrounding atmosphere. Therefore the following plasma parameters are used: $n_0 = 3 \times 10^{16} \mathrm{m}^{-3}$, $L = 4 \times 10^7$ m, $B_0 = 0.02$ T, and $b = 5 \times 10^5$ m. The superimposed disturbances have a spatial Fourier spec-

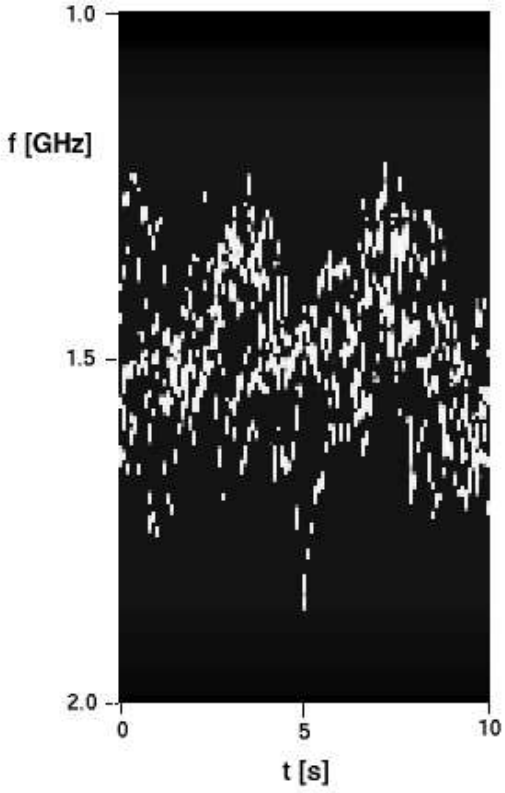

Fig. 4.18: The 1.0-2.0 GHz modelled radio spectrum of the cloud of spikes. The radio flux shown is in a logarithmic scale.

trum with a power-law form with the spectral index -2 in the range up to $10^{-2}\mathrm{m}^{-1}$, which is the minimum scale considered in the turbulence; phases are random and r.m.s. of the density perturbation reaches 10% of the static density profile. These values correspond to those observed in the solar wind space experiments (`Schwenn & Marsch 1991`) and they are also in agreement with the interpretation of the lace bursts in the previous section 4.1 (see also `Karlický et al. 2001`). As in the case of the lace bursts model the spatial turbulent density structure is simply advected by the jet with velocity $v_{outflow} = 2.0 \times 10^5 ms^{-1}$.
In the present case the magnetic field perturbations are not considered. The beam has the following parameters: $\alpha = 10^{-9}$, $T_\perp = 10^7$ K, $T_{||} = 10^3$ K, and the beam mean velocity along magnetic field lines $v_{||}$ is taken to be zero. Only the harmonic with $s = 4$ is considered.

Global spectral properties In the model with one magnetic flux tube the spikes are organised in chains. An example of such a spectrum is presented in Fig. 4.17. Such a way the correlation found among neighbouring spikes in observed spectra is easily explained in terms of this model. Furthermore, a combination of the radio emission from many magnetic flux tubes lead to a superposition of many spike chains, thus forming a cloud of narrowband dm-spikes (Fig. 4.18). As can be seen the presented modelled spike spectra are similar to observed ones.
Figure 4.19 shows comparison between the chain of the decimetric spikes and single lace burst line. Both modelled spectra were computed using the more accurate approach described in the section 4.2.2. The same parameters of surrounding environment were used as in the case of Fig. 4.17; for the lace burst, the shortest length scales in the turbulent spectrum were suppressed beginning by 100 km.

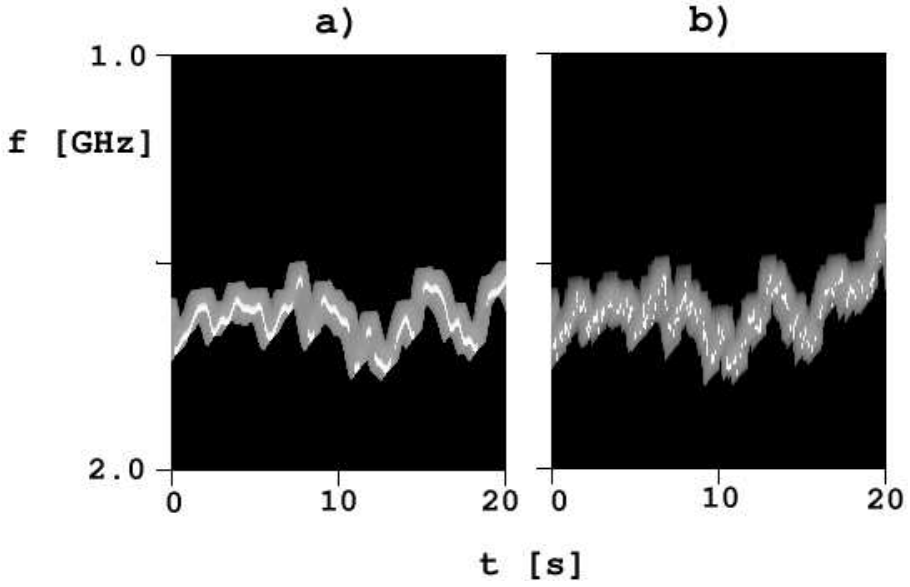

Fig. 4.19: Comparison between the single lace burst line (a) and the chain of dm-spikes (b). For both modelled spectra the more accurate approach based on equation (4.9) were used. For the lace line the high-frequency cut-off in the turbulent spectrum of density variations were taken into account. The corresponding length scale is 100 km; for spikes variations down to scales of 100 m were assumed on the other hand.

Individual spike characteristics Figure 4.20 shows the high-time resolution spectrum with single spikes and their instantaneous spectrum and time profile. The very narrow bandwidth and short duration corresponds well with observed data in this frequency range. The analysis by Güdel and Benz (1990) found that time profiles of individual spikes exhibit Gaussian raise and main phases followed by an exponential decay. To prove that, authors used the logarithmic derivative (LDF) of the radio flux F reduced of background continuum

$$LDF = \frac{\mathrm{d}}{\mathrm{d}t}\log(F(t)) = \frac{1}{F}\cdot\frac{\mathrm{d}F}{\mathrm{d}t}.$$

Prevailing exponential decay phase is indicated by constant value of LDF, linear decrease of the logarithmic derivative corresponds to the Gaussian time profile of radio flux on the other hand. Figure 4.21 shows results of this analysis for the modelled spike profile on 1670 MHz (a) and one observed on Trieste Observatory, Italy on 1420 MHz (b). The agreement between observed and modelled data is satisfactory.

The model properties overview As shown, this model is able to explain the main characteristics of the narrowband dm-spikes, especially their spectral features:

1. The spike decay profile is determined by the collisional damping of the upper hybrid waves.
2. There is a minimum bandwidth of spikes given by a size of the k-space of unstable upper hybrid waves. The spikes with broader bandwidth originate at spatially larger elementary sources or they are the result of a superposition of several individual spikes.
3. An interruption of spikes is given by very fast plasma parameter changes in a turbulent radio source. On the other hand, the slower component of plasma parameter changes change the spike emission frequency.

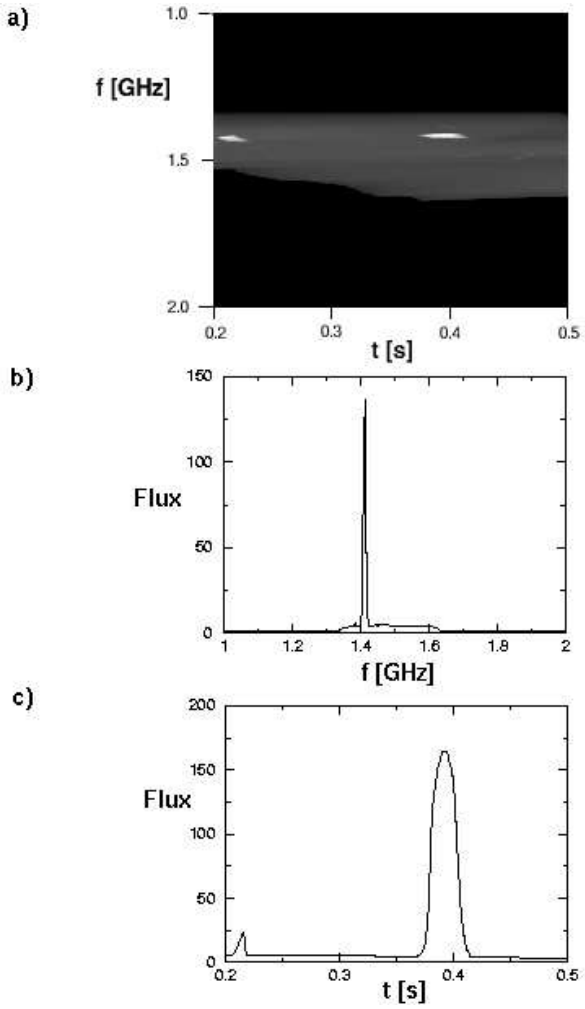

Fig. 4.20: **a)** The 1.0-2.0 GHz modelled radio spectrum of single spikes. The grey levels represent the radio flux in a logarithmic scale. **b)** The instantaneous spectrum of the spike at 0.4 s. The flux is in a linear relative scale. **c)** The time profile of the spike on the frequency 1412 MHz. The flux is in a linear relative scale.

4. Drifting chains of spikes are generated through a spatial "motion" of the resonance condition in the turbulent plasma inside the individual magnetic flux tube.

5. A superposition of the spike chains produce a cloud of spikes in the radio spectrum. These clouds can be divided into several branches according to their s-harmonics.

6. The narrowband line observed after the spike cloud (Fig. 4.13) can be explained by the same model, but with reduced turbulence.

7. A propagation of an anisotropic inhomogeneous beam can explain broad-band pulses with superimposed spikes.

8. The proposed model can also explain the observed time delays (2-5 sec) between hard X-rays and spikes (`Aschwanden & Gudel 1992`). This is due to a propagation effect. While the X-ray emission is caused by electrons propagating parallel to the magnetic field lines, the spikes in our model require the perpendicular electrons. It needs some time for the formation of the distribution function generating spikes.

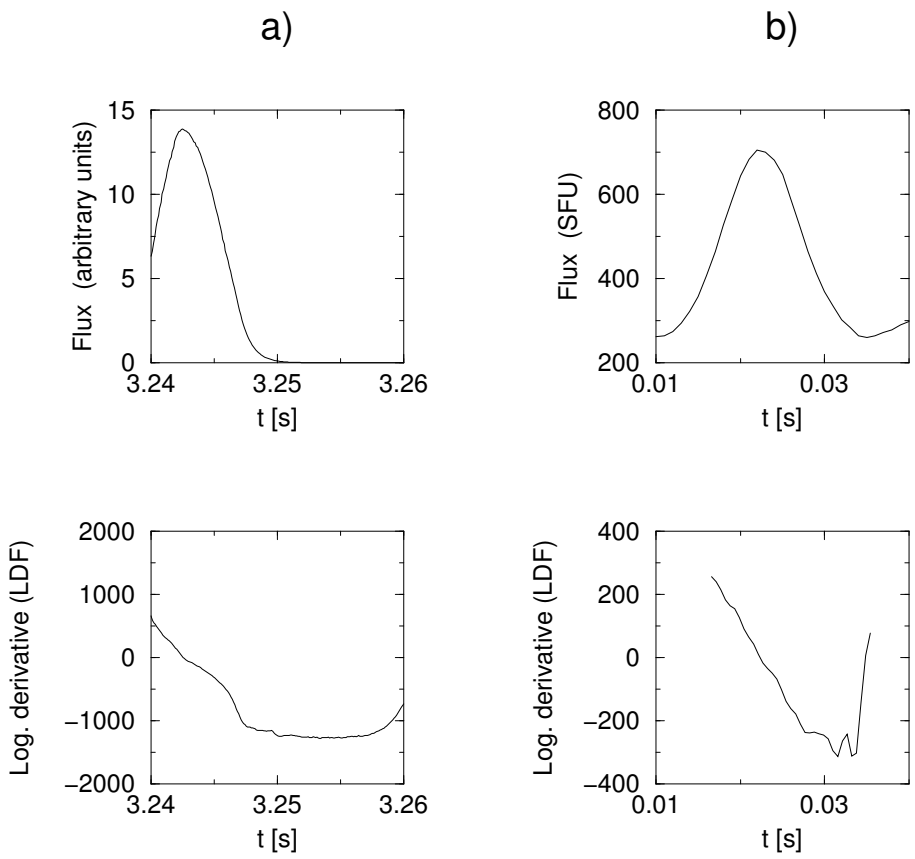

Fig. 4.21: Comparison between modelled and observed spike profile using logarithmic derivative of the flux (LDF). **a)** the time profile on 1670 MHz and its logarithmic derivative of modelled spike. The beginning of the spike profile is not included because of the high values of numerical noise in LDF. **b)** the time profile and its LDF of spike observed at Trieste Observatory, Italy (`INAF Trieste solar radioastronomy pages`) on 1420 MHz. The background of 215 SFU was subtracted before the analysis.

9. Observed Gaussian main phase followed by the exponential decay in time profiles of individual spike is in satisfactory agreement with the model. Fast decrease in Gaussian phase is caused by Landau-like damping of upper-hybrid waves in this model rather than by quasi-linear relaxation of unstable particle beam. The value of this non-linear damping rate is of the same order as the growth rate of the instability, what satisfies the nearly symmetrical time profiles of spikes.

10. In agreement with papers by Karlický et al. (1996) and Zlobec & Karlický (1998) is proposed that the narrowband dm-spikes are generated in the turbulent plasma reconnection out-flows (see Figs. 4.14, 1.10). The superthermal particles, leading to kinetic instabilities, are accelerated near the X-point of the magnetic field reconnection or directly in the cascading MHD turbulence according to the model.

11. Further development of the model is required – particularly the equation 4.9 should be generalised to take into account the propagation of the UH-waves in physical as well as Fourier spaces.

The present model of the narrowband dm-spikes shows that the zebra patterns, lace bursts and spikes belong to the same group of radio emissions and all these types of bursts are connected with the turbulence. These bursts, especially the lace bursts, provide a unique opportunity to study the flare turbulence.

Chapter 5

Wave mode conversion

As already mentioned in the Chapter 3 the wave mode conversion represents the second step in the plasma radiation processes. Conversion mechanisms have been studied by many authors as it is absolutely essential to estimate the efficiency of transformation into the escaping electromagnetic mode for the quantitative analysis of radio spectra. However, the complete understanding to this phenomenon is still far away due to the strong non-linearity of the problem.

Among conversion mechanisms described in the Chapter 3 the parametric instabilities of electrostatic plasma waves or their scattering on the electron density perturbations (ion-sound waves) are particularly important. This chapter is just devoted to the study of these two processes.

5.1 Parametric instabilities

It is commonly believed that in astrophysical plasmas, e.g. in the solar atmosphere, the Langmuir plasma waves are easily generated by particle (especially by electron) beams (see chapter 3, also Benz 1993). These Langmuir waves are transformed into the electromagnetic ones which can escape from the space of their origin and can be recorded by the Earth radio-telescopes. An example of such processes is the type III radio burst (e.g. Kundu 1965, Krüger 1979, Aschwanden & Treumann 1997). In older theoretical models of type III bursts, wave conversions are explained in terms of weak turbulence processes: $L \rightarrow T \pm S$, $L \rightarrow L' \pm S$, and $L + L' \rightarrow T$, for the radio emission on fundamental and harmonic frequency, respectively (Melrose 1980, Robinson et al. 1994). But more recently, a new non-linear concept with the four-wave hybrid modulational instability $\mathrm{L} \rightarrow \mathrm{T}^{+} + \mathrm{L}^{-} + \mathrm{S}$ was suggested (Abalde et al. 1998). These processes were studied to a limited extent by Akimoto (1988). In both these papers an analysis of the nonlinear dispersion equation derived from the Zakharov equations (see Zakharov 1972, Zakharov 1984) with the electromagnetic term was performed. On the other hand, analyses of the Zakharov equations in the electrostatic limit were made in many papers (e.g. one by Robinson (1997), and references therein). The various types of parametric instabilities of the monochromatic Langmuir waves were considered: a) decay, b) modified decay, c) modulational subsonic and supersonic, and hybrid which include also the electromagnetic waves. While in the electrostatic limit all instabilities in five regimes in the **k**-space are known (see Robinson 1997), in the general case with electromagnetic waves a general view is still missing. Namely, the above mentioned papers were devoted only to some special and particular cases.

Due to the great importance of electromagnetic waves for solar radioastronomy, a more general view on the parametric instabilities of Langmuir waves, in which electromagnetic ones are included is needed. In particular, the knowledge of the energy mode distribution at these instabilities is essential for estimation of radio radiation efficiency. In this new approach the energy transport (in the **k**-space) from the original monochromatic Langmuir wave into daughter modes

is more clearly shown – see papers by Bárta & Karlický (1999, 2000).

The principal non-linearity of the problem causes strong computational constraints. Therefore, only the linear stability analysis of the governing set of equations was made here for monochromatic plane Langmuir wave. Nevertheless, the energy description used here is similar to that used in the numerical codes solving the Zakharov equations directly, which enables direct comparison between these results and those at early stages of some numerical tasks.

5.1.1 Fundamental equations

The Zakharov equations in their generalised or "hybrid" form can be written as follows (Abalde et al. 1998, Zakharov et al. 1985):

$$\left(\frac{\partial^2}{\partial t^2} + \nu_e \frac{\partial}{\partial t} + c^2 \nabla \times \nabla \times - \gamma_e v_{th}^2 \nabla(\nabla \cdot) + \omega_p^2\right) \mathcal{E} = -\omega_p^2 \frac{n}{n_0} \mathcal{E},$$
$$n = F^{-1}\left(\frac{n_0}{k_B T_e} \cdot G(\mathbf{K}, \Omega) \cdot \hat{U}\right), \tag{5.1}$$

where n_0 and n are the electron density and slowly varying electron density fluctuation respectively, $\mathcal{E}(\mathbf{r}, t) = \mathbf{E}_0(\mathbf{r}, t) + \mathbf{E}(\mathbf{r}, t)$ is the total high-frequency electric field, $\mathbf{E}_0(\mathbf{r}, t)$ is the electric field strength of the parent Langmuir wave, while $\mathbf{E}$ is a small perturbation representing daughter modes; ω_p is the electron plasma frequency, v_{th} is the electron thermal velocity, ν_e is the damping frequency for electrons and γ_e is the ratio of the specific heats for electrons. F^{-1} means the inverse Fourier transform, $\hat{U}$ designates the Fourier transform of potential energy of the ponderomotive force and $G(\mathbf{K}, \Omega)$ is the plasma Green function (see Zakharov et al. 1985).
Now, supposing dispersion relations in a general form as $\omega = \omega(\mathbf{k})$, $\Omega = \Omega(\mathbf{K})$, the real quantity $\mathbf{E}(\mathbf{r}, t)$ can be expressed as a superposition of plane waves

$$\mathbf{E}(\mathbf{r}, t) = \frac{1}{2}\left(\int \mathbf{E}(\mathbf{k}) \cdot e^{i\cdot[\mathbf{kr} - \omega(\mathbf{k})t]} \mathrm{d}^3\mathbf{k} + c.c.\right)$$

and similarly

$$\mathbf{E_0}(\mathbf{r}, t) = \frac{1}{2}\left(\int \mathbf{E}_0(\mathbf{k_0}) \cdot e^{i\cdot[\mathbf{k_0 r} - \omega_0(\mathbf{k}_0)t]} \mathrm{d}^3\mathbf{k}_0 + c.c.\right) \tag{5.2}$$
$$n(\mathbf{r}, t) = \frac{1}{2}\left(\int n(\mathbf{K}) \cdot e^{i\cdot[\mathbf{Kr} - \Omega(\mathbf{K})t]} \mathrm{d}^3\mathbf{K} + c.c.\right),$$

where $\omega_0^2 = \omega_p^2 + \gamma_e v_{th}^2 k_0^2$ and ω, Ω are frequencies of perturbations. Inserting the relations (5.2) into the first Zakharov equation, omitting the second order terms and comparing terms with the same phase factors the formula for a perturbation of the electric field is obtained in form:

$$\mathbf{D}(\mathbf{k}, \omega) \cdot \mathbf{E}(\mathbf{k}) = -\frac{\omega_p^2}{2n_0} \int \mathbf{E}_0(\mathbf{k}_0)[n(\mathbf{k} - \mathbf{k}_0) + \bar{n}(\mathbf{k}_0 - \mathbf{k})] \mathrm{d}^3\mathbf{k}_0 \tag{5.3}$$

and matching relations for frequencies in the form

$$\omega(\mathbf{k}) = \omega_0(\mathbf{k}_0) + \Omega(\mathbf{k} - \mathbf{k}_0) = \omega_0(\mathbf{k}_0) - \bar{\Omega}(\mathbf{k}_0 - \mathbf{k}), \tag{5.4}$$

where $\mathbf{D}(\mathbf{k}, \omega)$ is the second order tensor

$$\mathbf{D}(\mathbf{k}, \omega) = -\omega^2 - i\nu_e\omega - c^2 \mathbf{k} \times \mathbf{k} \times + \gamma_e v_{th}^2 \mathbf{k}(\mathbf{k}\cdot) + \omega_p^2.$$

Multiplying the equation (5.3) by the tensor

$$\mathbf{D}^{-1}(\mathbf{k},\omega) = \frac{1}{k^2}\left[\frac{\mathbf{k}(\mathbf{k}\cdot)}{D_L} - \frac{\mathbf{k}\times\mathbf{k}\times}{D_T}\right],$$

which is the inverse operator to that of $\mathbf{D}(\mathbf{k},\omega)$ and where a designation

$$D_T(\mathbf{k},\omega) = -\omega^2 - i\nu_T\omega + c^2k^2 + \omega_p^2$$

$$D_L(\mathbf{k},\omega) = -\omega^2 - i\nu_L\omega + \gamma_e v_{th}^2 k^2 + \omega_p^2$$

was used, the perturbed electric field can be expressed as:

$$\begin{aligned}\mathbf{E}(\mathbf{k}) = -\frac{\omega_p^2}{2n_0}\int & \frac{E_0(\mathbf{k}_0)n(\mathbf{k}-\mathbf{k}_0)}{D_L}\frac{(\mathbf{k}\cdot\mathbf{k}_0)}{kk_0}\frac{\mathbf{k}}{k} + \\ & + \frac{E_0(\mathbf{k}_0)\bar{n}(\mathbf{k}_0-\mathbf{k})}{D_L}\frac{(\mathbf{k}\cdot\mathbf{k}_0)}{kk_0}\frac{\mathbf{k}}{k} + \\ & + \frac{E_0(\mathbf{k}_0)n(\mathbf{k}-\mathbf{k}_0)}{D_T}\frac{(\mathbf{k}\times\mathbf{k}_0)}{kk_0}\times\frac{\mathbf{k}}{k} + \\ & + \frac{E_0(\mathbf{k}_0)\bar{n}(\mathbf{k}_0-\mathbf{k})}{D_T}\frac{(\mathbf{k}\times\mathbf{k}_0)}{kk_0}\times\frac{\mathbf{k}}{k}\,\mathrm{d}^3\mathbf{k}_0.\end{aligned} \tag{5.5}$$

The fact that parent waves are longitudinal ($\mathbf{E}_0(\mathbf{k}_0) = E_0(\mathbf{k}_0)\cdot\mathbf{k}_0/k_0$) was taken into account. The wave dampings ν_L, ν_T for Langmuir and electromagnetic (transverse) waves, respectively, derived from the kinetic theory are used in the form:

$$\begin{aligned}\nu_L &= \left(\frac{\pi}{8}\right)^{1/2}|\mathbf{k}_0\pm\mathbf{K}|^{-3}\exp\left(-\frac{1}{2|\mathbf{k}_0\pm\mathbf{K}|^2}-\frac{3}{2}\right)+\nu_e,\\ \nu_T &= \nu_e = \frac{\ln\Lambda}{32\sqrt{2\pi}n_0\lambda_D},\end{aligned} \tag{5.6}$$

where $\ln\Lambda$ is the Coulomb logarithm.

5.1.1.1 Energy distribution to single modes

The relation (5.5) consists of four integrands which can be interpreted as the up- and down-converted Langmuir (the first two terms) and transverse electromagnetic (the second two) modes. Now, let us consider the case with the monochromatic plane wave

$$E_0(\mathbf{k}) = E_0\cdot\delta(\mathbf{k}-\mathbf{k}_0) \tag{5.7}$$

as a drive and introduce the phase energy density of electric field $w_E(\mathbf{k})$, i.e. the field energy contained in an unit volume and unit cube of the $\mathbf{k}$-space. Using the relation (3.25) the phase energy densities of electric fields in all four modes can be written as follows:

$$\begin{aligned}w_{E,L}^{\pm}(\mathbf{k}_0\pm\mathbf{K}) &= \frac{\mathrm{W}_0}{2n_0^2}\cdot|n(\mathbf{K})|^2\cdot\left|\frac{(\mathbf{k}_0\pm\mathbf{K})\cdot\mathbf{k}_0}{|\mathbf{k}_0\pm\mathbf{K}|k_0}\right|^2\cdot\frac{\omega_p^4}{|D_L(\mathbf{k}_0\pm\mathbf{K},\omega(\mathbf{k}_0\pm\mathbf{K}))|^2},\\ w_{E,T}^{\pm}(\mathbf{k}_0\pm\mathbf{K}) &= \frac{\mathrm{W}_0}{2n_0^2}\cdot|n(\mathbf{K})|^2\cdot\left|\frac{(\mathbf{k}_0\pm\mathbf{K})\times\mathbf{k}_0}{|\mathbf{k}_0\pm\mathbf{K}|k_0}\right|^2\cdot\frac{\omega_p^4}{|D_T(\mathbf{k}_0\pm\mathbf{K},\omega(\mathbf{k}_0\pm\mathbf{K}))|^2},\end{aligned} \tag{5.8}$$

where the factor of $(2\pi)^3/\mathrm{V}$, which would be cancelled in quantities of a physical significance, is omitted. Here W_0 is the electric field energy density of the parent wave and $\omega(\mathbf{k}_0\pm\mathbf{K})$ appearing in resonant denominators should be replaced by relations (5.4).

The phase energy densities of all daughter modes increase exponentially at the very beginning of considered instabilities. Now, supposing that the initial energy density is the thermal one given by the Rayleigh-Jeans law and using relations between electric field strength and density perturbation valid for ion-sound waves and relation (3.24) between total and electric field energy densities, the total phase energy densities at time t could be expressed as:

$$w_S(\mathbf{K},t) = \frac{1}{(2\pi)^3}\frac{1}{n_0\lambda_D^3}\cdot e^{2\Gamma(\mathbf{K})t}$$

$$w_L^{\pm}(\mathbf{k}_0 \pm \mathbf{K},t) = \tau \mathrm{W}_0 \cdot \cos^2\alpha^{\pm}\cdot \frac{w_S(\mathbf{K},t)}{|D_L^{\pm}|^2} \tag{5.9}$$

$$w_T^{\pm}(\mathbf{k}_0 \pm \mathbf{K},t) = \tau \mathrm{W}_0 \cdot \sin^2\alpha^{\pm}\cdot \frac{w_S(\mathbf{K},t)}{|D_T^{\pm}|^2},$$

where $\Gamma(\mathbf{K})$ is the imaginary part of the complex frequency $\Omega(\mathbf{K})$, and $\tau = (\gamma_e T_e + \gamma_i T_i)/T_e$. Furthermore, the standard dimensionless normalisation $\omega \to \omega/\omega_p$, $k \to (k\cdot\lambda_D)$ and $W \to W/(2n_0k_BT_e)$ (e.g. `Akimoto 1988`, `Abalde et al. 1998`) and the following designations were used:

$$\cos\alpha^{\pm} = \left|\frac{(\mathbf{k}_0 \pm \mathbf{K})\cdot\mathbf{k}_0}{|\mathbf{k}_0 \pm \mathbf{K}|k_0}\right|, \qquad \sin\alpha^{\pm} = \left|\frac{(\mathbf{k}_0 \pm \mathbf{K})\times\mathbf{k}_0}{|\mathbf{k}_0 \pm \mathbf{K}|k_0}\right|$$

$$D_L^{\pm} = -(\omega_0 \pm \Omega(\mathbf{K}))^2 \mp 2i\nu_L(\omega_0 \pm \Omega(\mathbf{K})) + 3(\mathbf{k}_0 \pm \mathbf{K})^2 + 1 \tag{5.10}$$

$$D_T^{\pm} = -(\omega_0 \pm \Omega(\mathbf{K}))^2 \mp 2i\nu_T(\omega_0 \pm \Omega(\mathbf{K})) + (c/v_{th})^2(\mathbf{k}_0 \pm \mathbf{K})^2 + 1.$$

It should be noted that the electron specific heat ratio of Langmuir waves was taken as $\gamma_e = 3$.

Now, the question arises up to what time this approach is valid. As a criterion of this validity, from which the time can be estimated, the condition

$$\mathrm{W}_{tot}(t) \ll \mathrm{W}_0$$

was used, where $\mathrm{W_{tot}(t)}$ and $\mathrm{W_0}$ are the total energy density (integrated over the **k**-space) contained in all daughter modes at time t and the initial Langmuir wave energy density respectively. Namely, it says that at time t only a small fraction of the input energy is transformed to daughter modes. The daughter modes density is calculated as follows:

$$\mathrm{W}_{tot}(t) = 2\pi \int \sum_i w_i(\mathbf{k},t)\mathrm{dk}_{\|}\cdot \mathrm{k}_{\perp}\mathrm{dk}_{\perp}, \tag{5.11}$$

where the axis-symmetry of these processes in the **k**-space was taken into account, and where the sum runs through all five modes (two electrostatic, two electromagnetic and ion-sound ones).

5.1.1.2 Dispersion equation

Computing the potential of the ponderomotive force the dispersion equation can be easily derived from the Fourier transform of the second Zakharov equation. Relations (5.2), (5.5) and (5.7), and only slowly varying terms were considered. Finally, eliminating $n(\mathbf{K})$ the full nonlinear dispersion equation in a dimensionless form can be written (see also `Robinson 1997`):

$$0 = 1 + G(\mathbf{K},\Omega)\cdot\frac{W_0}{2}\left(\frac{\cos^2\alpha^+}{D_L^+} + \frac{\sin^2\alpha^+}{D_T^+} + \frac{\cos^2\alpha^-}{D_L^-} + \frac{\sin^2\alpha^-}{D_T^-}\right),$$

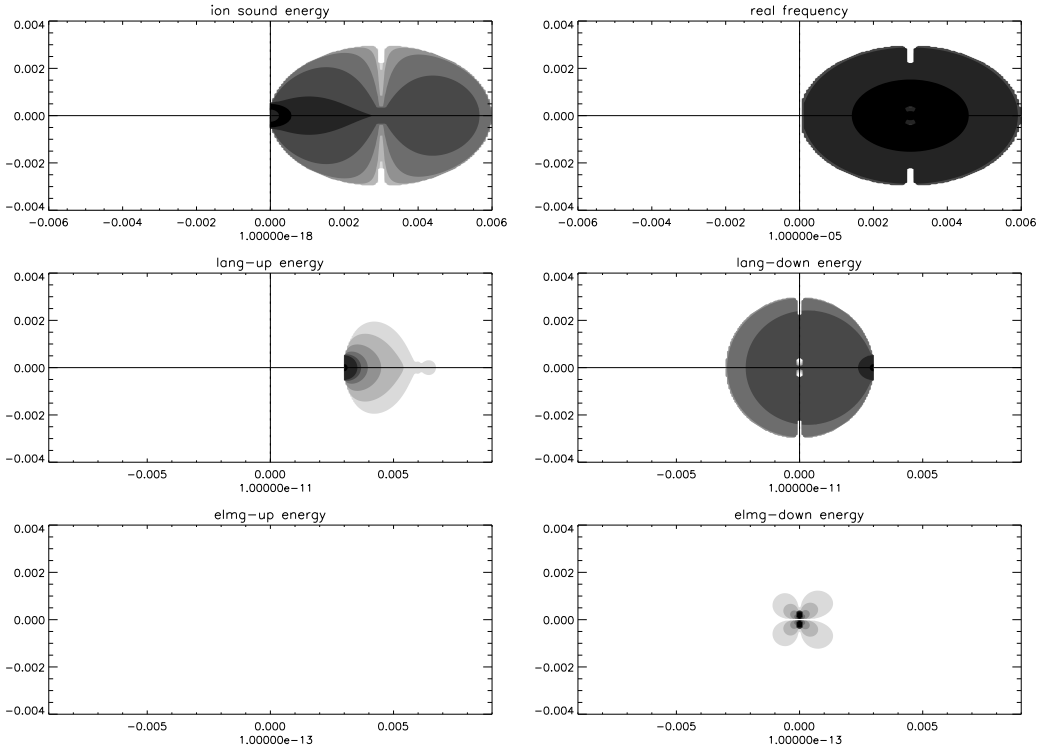

Fig. 5.1: The energy mode distribution for the regime of the modulational instability. The parent wave has $k_0 = 0.003$ and the wave energy $W_0 = 10^{-6}$. The hydrodynamic-like approximation (equation 5.19) and $\nu_L = 0$, $\nu_T = 0$ were used: (a) the contour plot of the phase energy density of ion-sound waves, (b) the contour plot of the real frequency of ion-sound waves, (c) the contour plot of the phase energy density of up-converted Langmuir waves, (d) the contour plot of the phase energy density of down-converted Langmuir waves, (e) the contour plot of the phase energy density of up-converted electromagnetic waves, and (f) the contour plot of the phase energy density of down-converted electromagnetic waves.

where the Green function $G(\mathbf{K}, \Omega)$ can be expressed by means of the ion dielectric function $\epsilon(\mathbf{K}, \Omega)$ as:

$$G(\mathbf{K}, \Omega) = -\frac{K^2 \cdot \epsilon(\mathbf{K}, \Omega)}{1 + K^2 \cdot \epsilon(\mathbf{K}, \Omega)}. \tag{5.12}$$

5.1.1.3 Approximations of the dispersion equation

The dispersion equation can be solved in several different approximations. The first one concerns a basic validity assumption of the Zakharov equations - i.e. that timescales of electron and ion motions are sufficiently different. This fact can be expressed in the form

$$\Omega \ll \omega_p. \tag{5.13}$$

So, one can neglect terms of the second order of Ω in the resonant denominators $D_L^{\pm}$ and $D_T^{\pm}$. This procedure corresponds to an omission of the second time derivative of the electric field envelope in the standard derivation of the first Zakharov equation. Thus, one can write:

$$\begin{aligned} D_L^{\pm} &\approx \mp 2 \left(\Omega(\mathbf{K}) \pm 3/2 k_0^2 \mp 3/2 (\mathbf{k}_0 \pm \mathbf{K})^2 + i\nu_e \right) \equiv \mp 2 \mathcal{D}_L^{\pm} \\ D_T^{\pm} &\approx \mp 2 \left(\Omega(\mathbf{K}) \pm 3/2 k_0^2 \mp 1/2 (c/v_{th})^2 (\mathbf{k}_0 \pm \mathbf{K})^2 + i\nu_e \right) \equiv \mp 2 \mathcal{D}_L^{\pm}. \end{aligned} \tag{5.14}$$

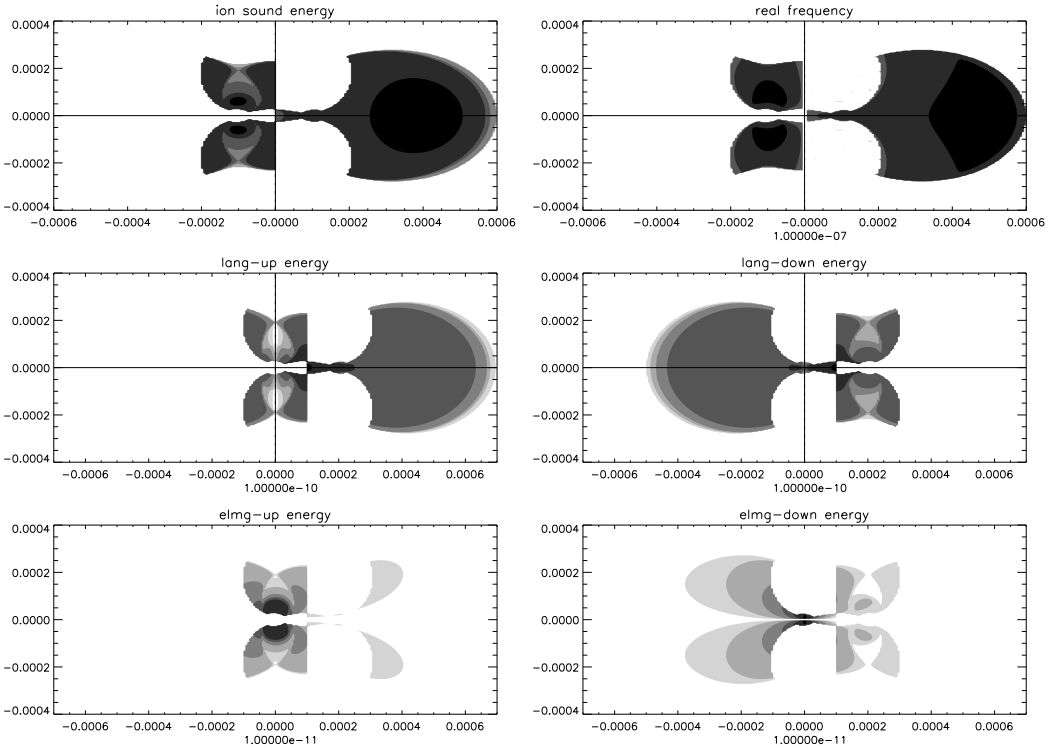

Fig. 5.2: The energy mode distribution for the regime of the subsonic modulational instability. The parent wave has $k_0 = 10^{-4}$ and the wave energy $W_0 = 10^{-6}$. The L_3 approximation (equation 5.19) and $\nu_L = 0$, $\nu_T = 0$ were used: (a) the contour plot of the phase energy density of ion-sound waves, (b) the contour plot of the real frequency of ion-sound waves, (c) the contour plot of the phase energy density of up-converted Langmuir waves, (d) the contour plot of the phase energy density of down-converted Langmuir waves, (e) the contour plot of the phase energy density of up-converted electromagnetic waves, and (f) the contour plot of the phase energy density of down-converted electromagnetic waves.

The second approximation is given by different expressions for the ion dielectric function. For example, in modulational instabilities, where wavenumber $\mathbf{k}$ is sufficiently small, the quasi-neutrality approximation $n_e = n_i$ can be used and $\epsilon(\mathbf{K}, \Omega)$ can be expressed as follows (SI units):

$$\epsilon(\mathbf{K}, \Omega) = -\frac{e^2}{\varepsilon_0 M_i K^2} \int \frac{\partial f_0(\mathbf{v})}{\partial \mathbf{v}} \cdot \frac{\mathbf{K}}{\mathbf{Kv} - \Omega} \mathrm{d}^3\mathbf{v}. \tag{5.15}$$

On the other hand, in decay instabilities where short-wavelength ion-sound waves also take part, a delay of ions must be taken into account and thus the dielectric function becomes:

$$\epsilon(\mathbf{K}, \Omega) = 1 - \frac{e^2}{\varepsilon_0 M_i K^2} \int \frac{\partial f_0(\mathbf{v})}{\partial \mathbf{v}} \cdot \frac{\mathbf{K}}{\mathbf{Kv} - \Omega} \mathrm{d}^3\mathbf{v}. \tag{5.16}$$

Here, the unperturbed ion distribution function $f_0(\mathbf{v})$ can be expressed in different forms. The Maxwellian distribution seems to be the most natural choice, but it will bring many computational difficulties and moreover, the ion distribution function in the solar wind indicates superthermal tails (`Cairns et al. 1998` and references therein). For these reasons generalised Lorenzian distributions are more appropriate. Two of them were tried (also in SI units):

$$L_2(\mathbf{v}) = \frac{an_0}{\pi^2} \cdot \frac{1}{(v^2 + a^2)^2}, \tag{5.17}$$

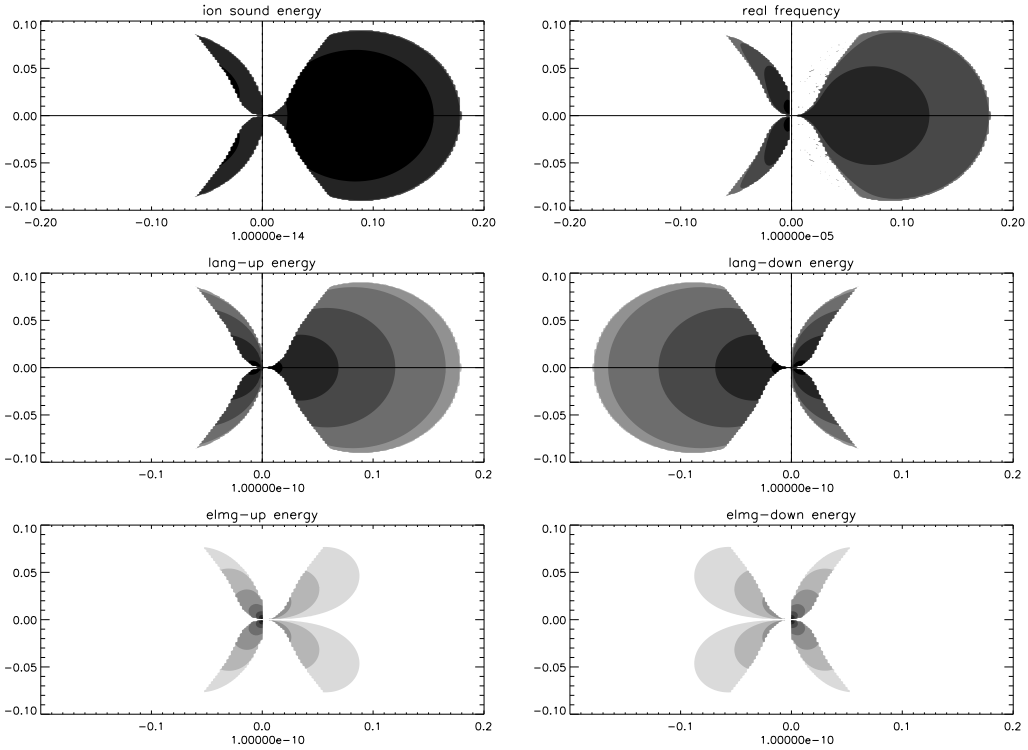

Fig. 5.3: The energy mode distribution for the regime of the supersonic modulational instability. The parent wave has $k_0 = 10^{-4}$ and the wave energy $W_0 = 0.1$. The hydrodynamic-like approximation (equation 5.19) and $\nu_L = 0$, $\nu_T = 0$ were used: (a) the contour plot of the phase energy density of ion-sound waves, (b) the contour plot of the real frequency of ion-sound waves, (c) the contour plot of the phase energy density of up-converted Langmuir waves, (d) the contour plot of the phase energy density of down-converted Langmuir waves, (e) the contour plot of the phase energy density of up-converted electromagnetic waves, and (f) the contour plot of the phase energy density of down-converted electromagnetic waves.

where the temperature parameter $a = \sqrt{\frac{3k_BT_i}{M_i}}$ was found by a matching of inflection points of the 1-D L_2 and Maxwellian distributions, and

$$L_3(\mathbf{v}) = \frac{4n_0a^3}{\pi^2} \cdot \frac{1}{(v^2 + a^2)^3}. \tag{5.18}$$

Here, the temperature parameter $a = \sqrt{\frac{5k_BT_i}{M_i}}$.

Now, combining all these approximations, one can obtain several different forms of the dispersion equation.

Hydrodynamic-like equation. This equation is derived from the general form (5.12) using (5.14), which follows from the $\Omega \ll \omega_p$ condition and choosing the quasi-neutral approximation (5.15) for the dielectric function. Here, the $L_2(\mathbf{v})$, which is defined by (5.17), stands for an unperturbed distribution function. As a result the formula (in dimensionless units, compare with `Akimoto 1988`)

$$\Omega^2 - 2i\nu_i\Omega - \mu\tau K^2 = -\frac{\mu W_0}{4}\left(\frac{\cos^2\alpha^-}{\mathcal{D}_L^-} - \frac{\cos^2\alpha^+}{\mathcal{D}_L^+} + \frac{\sin^2\alpha^-}{\mathcal{D}_T^-} - \frac{\sin^2\alpha^+}{\mathcal{D}_T^+}\right),$$

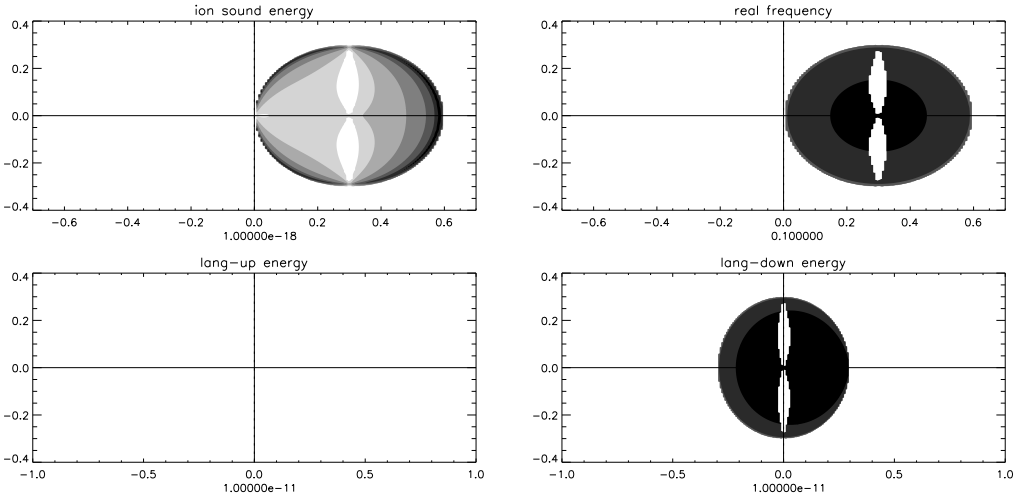

Fig. 5.4: The energy mode distribution for the regime of the electrostatic decay instability. The parent wave has $k_0 = 0.3$ and the wave energy $W_0 = 10^{-6}$. The hydrodynamic-like approximation without electromagnetic terms and $\nu_L = 0$ were used: (a) the contour plot of the phase energy density of ion-sound waves, (b) the contour plot of the real frequency of ion-sound waves (see non-physically high frequencies), (c) the contour plot of the phase energy density of up-converted Langmuir waves, and (d) the contour plot of the phase energy density of down-converted Langmuir waves (see a non-physically high energy density in the central part).

was obtained, where $\mu = m_e/M_i$, and the ion-sound damping ν_i was evaluated as:

$$\nu_i = K \cdot \sqrt{3\mu \frac{T_i}{T_e}}.$$

This equation was solved by Akimoto (1988) and Abalde et al. (1998) in the 1-dimensional case, who derived it directly from the hydrodynamic approximation of the Zakharov equations. The ion damping term appearing in their description must be seen as an *ad hoc* added element, because it cannot be correctly computed within the hydrodynamic theory. On the other hand, the ion-sound damping term ν_i introduced here is derived consistently from the kinetic theory. It means, that it can be used even for a computation of the long-wave modulational instability with a low-energy drive (in contrast to that derived by Akimoto (1988)).
Although this approximation is the simplest one from a numerical point of view and directly corresponds to the Zakharov equations in their most familiar form (see eqs. 3.84, 3.85 in the section 3.3.2.2, also Robinson 1997), its solution in a short wavelength regime brings several difficulties (see following results). So one should look for a better approximation of the dispersion equation to remove them.

L_3-approximation of the distribution function. At first, an attempt to improve the ion distribution function to be closer to the Maxwellian one was made. So the $L_3(\mathbf{v})$ function was chosen for the ion velocity distribution. The resulting equation is:

$$\frac{(\Omega + iKa)^3}{\Omega + 3iKa} - \mu\tau K^2 = -\frac{\mu W_0}{4}\left(\frac{\cos^2\alpha^-}{\mathcal{D}_L^-} - \frac{\cos^2\alpha^+}{\mathcal{D}_L^+} + \frac{\sin^2\alpha^-}{\mathcal{D}_T^-} - \frac{\sin^2\alpha^+}{\mathcal{D}_T^+}\right),$$

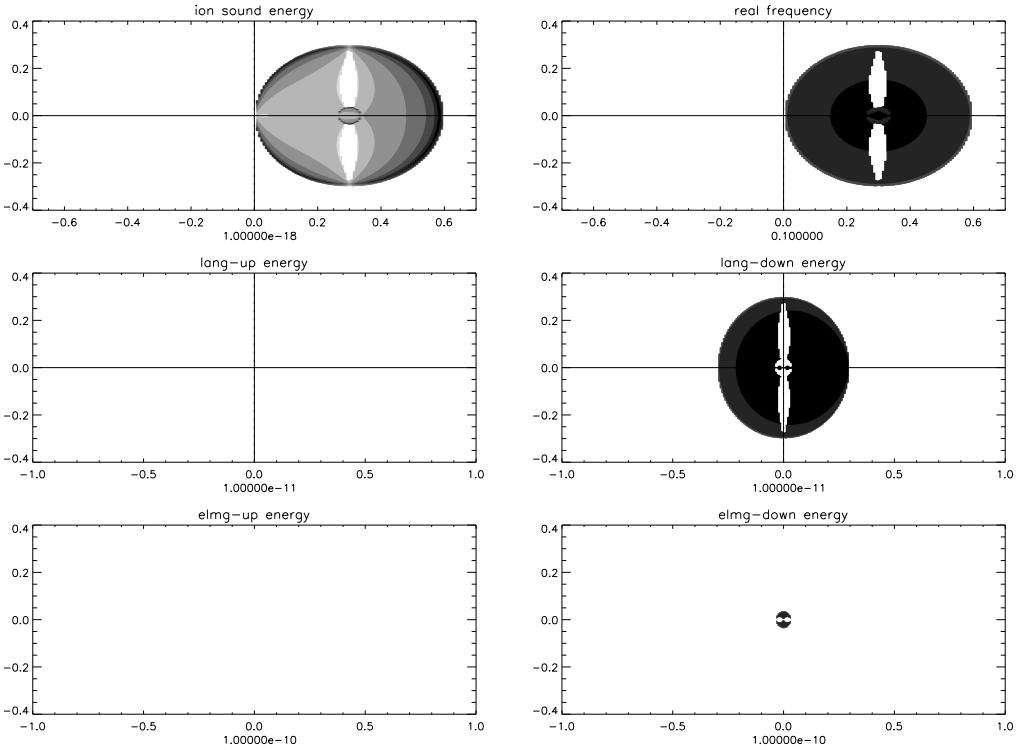

Fig. 5.5: The energy mode distribution for the regime of the decay instability. The parent wave has $k_0 = 0.3$ and the wave energy $W_0 = 10^{-6}$. The hydrodynamic-like approximation (equation 5.19) and $\nu_L = 0$, $\nu_T = 0$ were used: (a) the contour plot of the phase energy density of ion-sound waves, (b) the contour plot of the real frequency of ion-sound waves (see non-physically high frequencies), (c) the contour plot of the phase energy density of up-converted Langmuir waves, (d) the contour plot of the phase energy density of down-converted Langmuir waves (see a non-physically high energy density in the central part), (e) the contour plot of the phase energy density of up-converted electromagnetic waves, and (f) the contour plot of the phase energy density of down-converted electromagnetic waves (see a non-physically high energy density in the central part).

where the velocity spread parameter a (in dimensionless units) can be written as

$$a = \sqrt{5\mu \frac{T_i}{T_e}}.$$

It should be noted, that the similar equation in the electrostatic limit was solved by Robinson (1997) and Cairns & Robinson (1998). A small difference was found in an evaluation of the temperature parameter a which they computed by a matching of curvatures of L_3 and Maxwellian rather then by a matching of inflection points of these distributions. This leads to a different value of this parameter by a factor of ≈ 2.

Non-linear denominators. The main problem of equation (5.19) is, that in the short-wavelength limit, it gives a solution with non-physically high real frequencies for growing modes. This effect violates the basic assumption of the Zakharov equations. Thus, the standard linearization (5.14) could be no longer used and therefore nonlinear denominators $D^{\pm}_{L,T}$ should be accounted for. For the left-hand (ion-sound) side of the equation that from the paragraph of "**Hydrodynamic-like equation**" was used.

Quasi-neutrality violation. For short-wavelength ion-sound modes, where the condition $(K\cdot\lambda_D)^2 \ll 1$ is violated, the approximation $n_e = n_i$ is not valid. It needs to change the dielectric function to the form expressed in the relation (5.16), where the Poisson equation is considered. The dispersion equation with this dielectric function in both L_2 and L_3 approximations of the distribution function was computed. For the right-hand side the linearized forms of denominators (5.14) were used.

The most general approximation. Combining these approximations the dispersion equation with the lowest number of assumptions made was found. The non-linear denominators as well as the non-quasi-neutral dielectric function and the L_3 approximation was used. The result is expressed by the following equation:

$$\frac{(\Omega + iKa)^3}{\mu(\Omega + 3iKa) - (\Omega + iKa)^3} - K^2 = \\ = -\frac{W_0}{2}\left(\frac{\cos^2\alpha^+}{D_L^+} + \frac{\sin^2\alpha^+}{D_T^+} + \frac{\cos^2\alpha^-}{D_L^-} + \frac{\sin^2\alpha^-}{D_T^-}\right), \tag{5.19}$$

where the parameter a is again $a = \sqrt{5\mu T_i/T_e}$. Note only, that this equation is equivalent to the algebraic equation of eleven order.

5.1.1.4 Solution of dispersion equation

In the following the dispersion equations are solved numerically in two regimes: a) in the electrostatic limit, and b) in the full version with electromagnetic waves. The dispersion equation was transformed into the polynomial form, whose order depends on the approximation used. Orders of polynomials vary from four (electrostatic case) up to eleven (the most general approximation). The Newton (and gradient and Laguerr as auxiliary) methods are used in numerical solutions of this dispersion equation (5.12) in various approximations for different input parameters.
The methods used yield full information about parametric instabilities, i.e. growth rates, **K** and Ω of perturbations, and up- and down conversion modes. While in previous papers only growth rates *vs* **K** were presented, here more detailed view is presented, especially also the types of daughter modes to which the energy is transferred is shown. Therefore, the following presentation of results is used: Using a standard way, firstly the growth rate of the ion-sound perturbation in dependence on **K** is computed. Then, considering the thermal level of plasma density noise and a time interval which is sufficiently short (the energy in daughter waves has to be much smaller than that of the pump Langmuir wave), the value of the exponentially growing density perturbation was computed according to formula (5.9). Then putting this value into relations (5.5) and (5.9) the electric fields as well as their energies in all daughter modes were found. Thus, the energy mode distributions at the very early stages of parametric instabilities are estimated.

Somewhat confusing terminology concerning so called "up-" and "down-conversion" occurred in several previous papers. Waves which have the frequency $\omega = \omega_0 + \Omega$ are called up-converted while waves with the frequency $\omega = \omega_0 - \Omega$ are called down-converted waves. However, if the real part of Ω is negative, the resulting frequency of the up-converted wave becomes lower than that of the pump wave. It leads, for example, to false considerations that one-dimensional solutions of the dispersion equation (5.19) made by Akimoto (1988) and Abalde et al. (1998) are different. It is much more convenient to keep the real frequency positive. In this case the propagation direction of waves is given by the **K**-vector only. Moreover, the full **K** space is presented here, since it makes diagrams more understandable. Namely, in several papers only the quarter of the

K space is shown, and thus sometimes growth rates corresponding to the positive and negative values of Ω are superimposed.

5.1.2 Results

Generally speaking, there are many possibilities for choosing parameters for numerical computations. To compare electrostatic aspects of our results with previous ones, the same initial parameters as used in the paper by Robinson (1997) were taken into account. On the other hand, in applications a more realistic temperature ratio of $T_e/T_i = 4$ (see Lin et al. 1986) was considered. Moreover, in present case for most computations the full electromagnetic version of dispersion equations is used. Results are plotted in decadic logarithmic scales. First, the maximum value and its order are determined and then the highest eight decades are depicted. The highest level is black. The maximum order is printed below each contour plot. If the highest level of Langmuir or electromagnetic energy densities is smaller than the thermal noise, the waves are not considered.

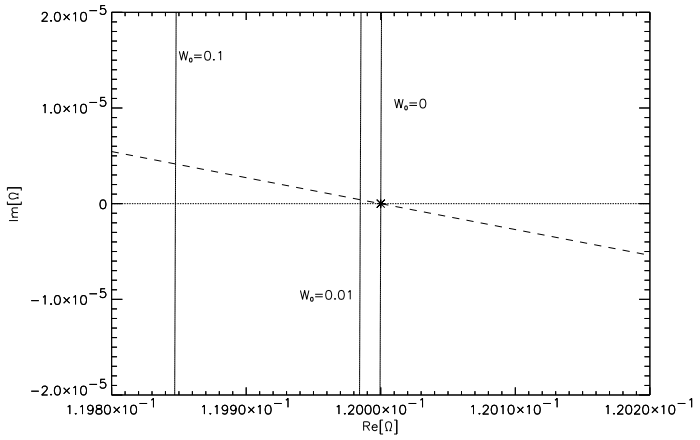

Fig. 5.6: The complex plane analysis of the dispersion equation. The electrostatic decay with the $k_0 = 0.3$, energies $W_0 = 0$, 7×10^{-3}, and 0.1 was considered. In the studied **K**-space $K_x = 0.4$, $K_y = 0$ were selected. Solid lines express the solution of the real part of the dispersion equation, the dashed line expresses the imaginary part. Asterisks correspond to zero energy of the parent wave.

5.1.2.1 Modulational instabilities

According to previous results in the electrostatic limit (Zakharov 1972, Zakharov 1984, Robinson 1997) there are three types of modulational instability: (a) modulational, (b) subsonic modulational, and (c) supersonic modulational instability.
Present analysis started with the first regime of the modulational instability. In this case the parent wave with the **k**-vector $k_0 = 0.003$ and the wave energy $W_0 = 10^{-6}$ was initiated. The hydrodynamic-like approximation of the dispersion equation (5.19) was used. Its validity needs to be verified by checking assumptions used with results. Namely, the real frequency should be much less than unity, i.e. in SI units much less than the plasma frequency. It is interesting to note, that in the case of L_2 approximation of the ion distribution function, the resulting dispersion equation has the same form as derived in the standard hydrodynamic approximation (compare with Akimoto 1988). Furthermore, it was found that the results for the L_3 approximation remain qualitatively the same as in the L_2 case. Firstly, the growth rate and corresponding real frequency were determined. As mentioned above, it is convenient to keep the real frequency

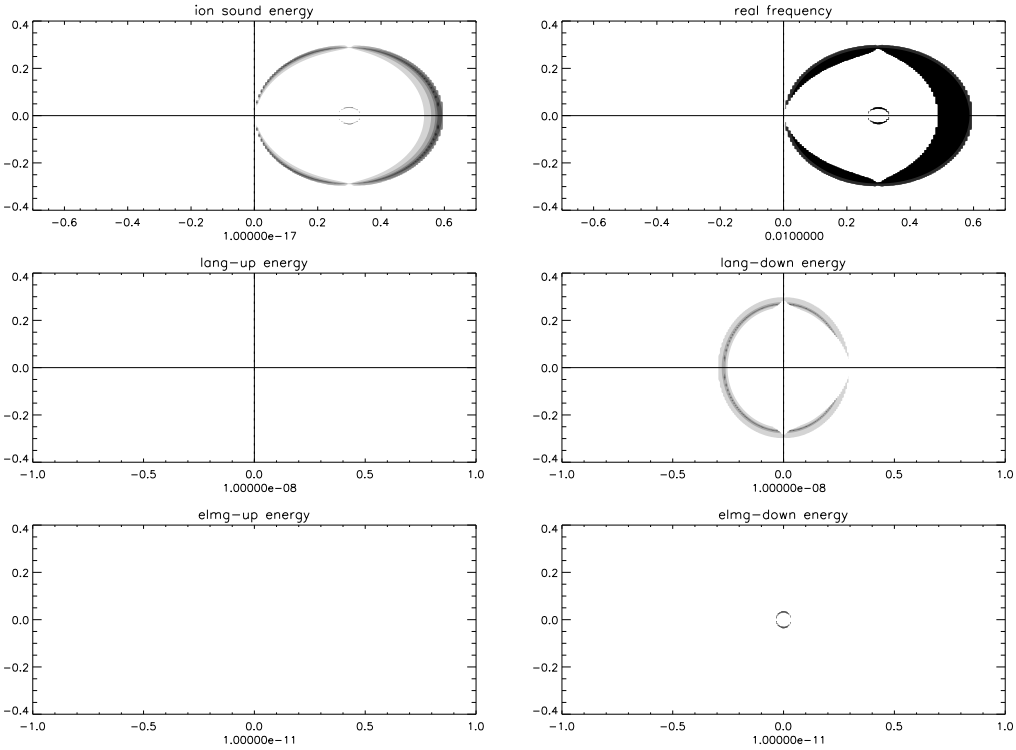

Fig. 5.7: The improved energy mode distribution for the regime of the decay instability. The parent wave has $k_0 = 0.3$ and the wave energy $W_0 = 10^{-6}$. The most general approximation (5.19) with the $\nu_L = 0$ and $\nu_T = 0$ was used: (a) the contour plot of the phase energy density of ion-sound waves, (b) the contour plot of the real frequency of ion-sound waves, (c) the contour plot of the phase energy density of up-converted Langmuir waves, (d) the contour plot of the phase energy density of down-converted Langmuir waves, (e) the contour plot of the phase energy density of up-converted electromagnetic waves, and (f) the contour plot of the phase energy density of down-converted electromagnetic waves.

positive. For this reason the invariance property $(\mathbf{K}, \Omega) \leftrightarrow (\mathbf{K}, \bar{\Omega})$ of the dispersion equation was used. It means that the $\mathbf{K}$-vector with the negative real frequency is transformed to new one with $-\mathbf{K}$. Then using the equation (5.9) with $t = 100$ plasma periods the phase densities of ion-sound, Langmuir and electromagnetic waves were computed. In all following cases $T_e = 100T_i$ is used. The Langmuir as well as electromagnetic waves are divided into two parts: up- and down-converted modes. This means that a full description of Langmuir and electromagnetic waves is given by a superposition of both modes.

The energy mode distribution for the regime of the modulational instability is shown in Fig. 5.1, where there are: (a) the contour plot of the phase energy density of ion-sound waves, (b) the contour plot of the real frequency of ion-sound waves (only real frequencies corresponding to the positive growth rates are shown) (c) the contour plot of the phase energy density of up-converted Langmuir waves, (d) the contour plot of the phase energy density of down-converted Langmuir waves, (e) the contour plot of the phase energy density of up-converted electromagnetic waves, and (f) the contour plot of the phase energy density of down-converted electromagnetic waves. As expected, the results show a typical four-wave process with the broad-band $\mathbf{k}$-spectrum. In the electrostatic limit similar results were obtained. Clearly, the electromagnetic modes are missing as well as the central bubble of perturbations around $k_x = 0.003$, $k_y = 0.0$.
Then the subsonic and supersonic regimes of the modulational instability were computed in the

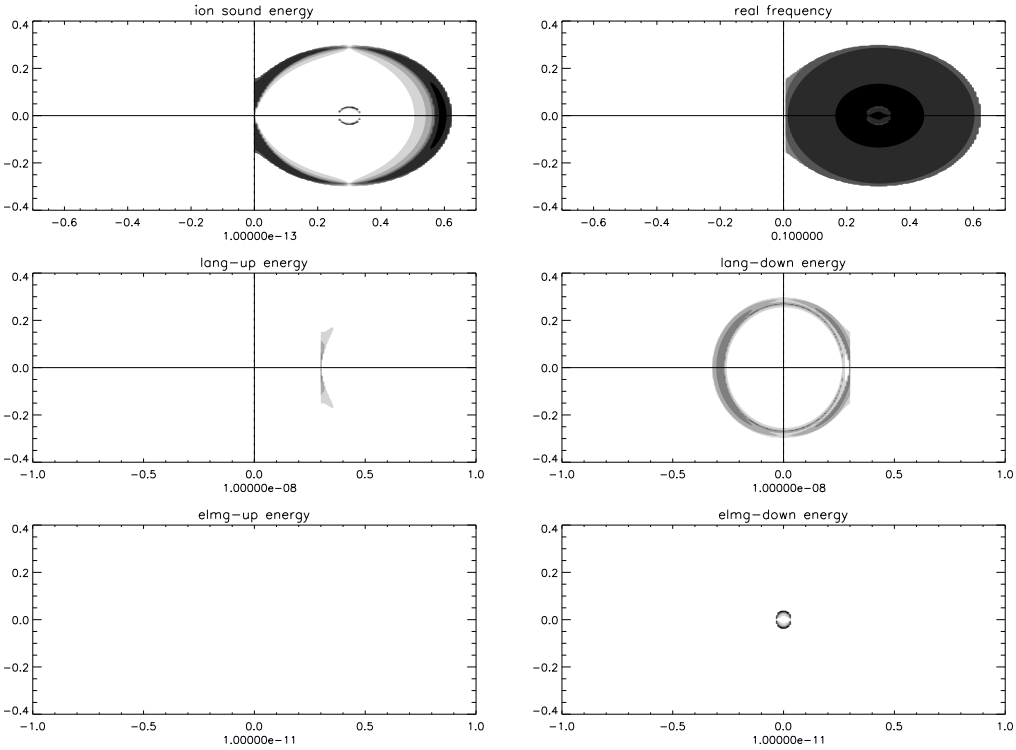

Fig. 5.8: The improved energy mode distribution for the regime of the modified decay instability. The parent wave has $k_0 = 0.3$ and the wave energy $W_0 = 0.1$. The most general approximation (5.19) with the $\nu_L = 0$ and $\nu_T = 0$ was used: (a) the contour plot of the phase energy density of ion-sound waves, (b) the contour plot of the real frequency of ion-sound waves, (c) the contour plot of the phase energy density of up-converted Langmuir waves, (d) the contour plot of the phase energy density of down-converted Langmuir waves, (e) the contour plot of the phase energy density of up-converted electromagnetic waves, and (f) the contour plot of the phase energy density of down-converted electromagnetic waves.

same way. Results are shown in Figs 5.2 and 5.3, where the parameters $k_0 = 10^{-4}$, $W_0 = 10^{-6}$ and $k_0 = 10^{-4}$, $W_0 = 0.1$ were considered. These regimes show nice and descriptive examples of the "mirroring" of waves in the **k**-space expressing thus the change of negative to positive real frequencies.

5.1.2.2 Decay instabilities

Decay instabilities in the electrostatic limit can be divided into two regimes (`Zakharov 1972`, `Zakharov 1984`, `Robinson 1997`): (a) decay and (b) modified decay instabilities. Results in the electrostatic and full electromagnetic cases in the hydrodynamic-like approximation, for the parameters $k_0 = 0.3$, $W_0 = 10^{-6}$ are shown in Figs 5.4 and 5.5. In both regimes unexpected problems appeared. See non-physically high energy densities (Figs 5.4d, 5.5d, and 5.5f) corresponding to real frequencies which are too high (see values below Figs 5.4b, 5.5b) in contradiction to the basic assumption (5.13). By a detailed analysis it was found that these problems are due to a presence of the ion-sound damping. Without this term these problems disappear. This fact was confirmed by an analysis of the polynomial form of the dispersion equation in the complex plane. An example of this analysis for the ES decay case (the same as presented in Fig. 5.4, for $K_x = 0.4$, $K_y = 0$) is shown in Fig. 5.6. Here, solutions of the dispersion equation correspond to crossing points between solid and dashed lines. The presence of the ion-sound damping causes a deviation of the imaginary part solution (dashed line) from the horizontal axis. For the zero-

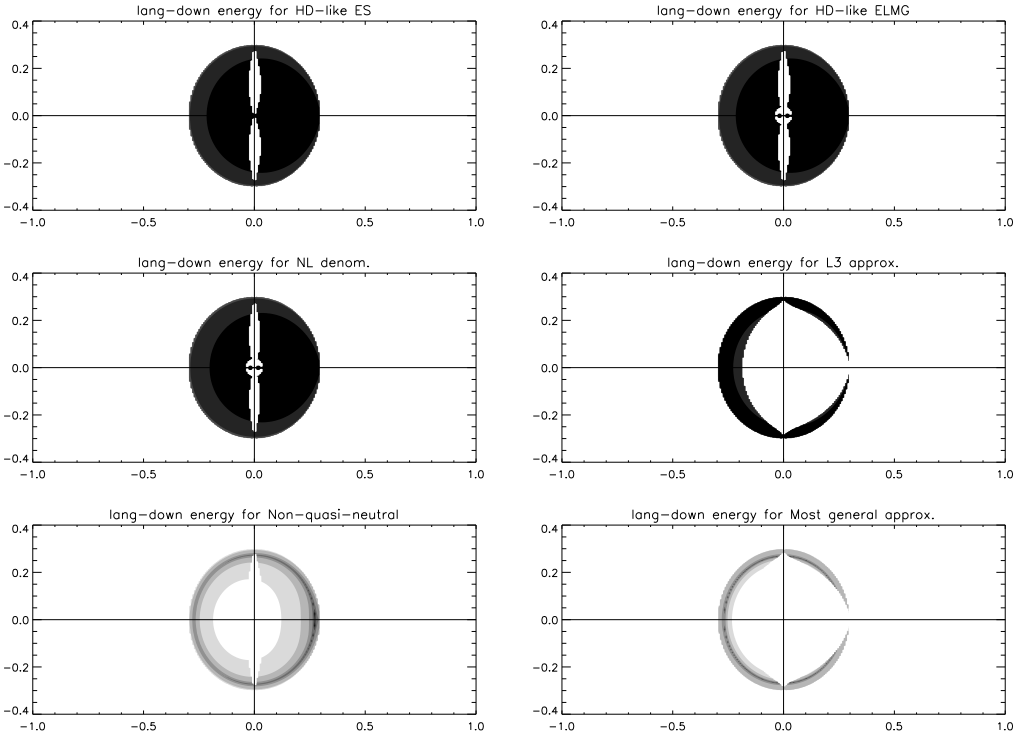

Fig. 5.9: The comparison of all considered approximations for the decay instability. The down-converted Langmuir waves energies are shown: (a) the electrostatic case of hydrodynamic approximation, (b) the electromagnetic hydromagnetic-like approximation, (c) the nonlinear denominators approximation, (d) L_3 approximation, (e) the non-quasi-neutral approximation with the L_2 distribution function, and (f) the most general approximation.

energy parent wave the solution is designated by the asterisk. With the increase of the wave energy the solution is shifted to the left and the growth rate becomes positive. But the problem is that the frequency of perturbation is non-physically high (real part of $\Omega \approx 0.12\omega_p$). Thus, it was found that the approximation used leads to serious problems. For these reasons more sophisticated approximations were suggested and analysed (subsection 5.1.1.3). The energy mode distributions were computed for all approximations and only a small part of these results are shown in Figs 5.7, 5.8, and 5.9.
In Fig. 5.7 the decay instability ($k_0 = 0.3$, $W_0 = 10^{-6}$) in the most general approximation is shown. In this case the non-physical high densities connected with the high real frequencies in the central part of Fig. 5.7d disappeared. Similarly in Fig. 5.8, where the modified decay instability ($k_0 = 0.3$, $W_0 = 0.1$) in the most general approximation is presented, problematic parts in the **k**-space are reduced. Also in this case the approximation leads to better results. Plots show two types of decay processes: $L \rightarrow L' + S$, $L \rightarrow T + S$. The first process is expressed by big circles in Figs 5.7a, 5.7d. In this case only down-converted Langmuir waves are generated and the bandwidth in the **K**-space is very narrow; in agreement with the three-wave process. Small circles close to $K_x = 0.3$, $K_y = 0$ (Fig. 5.7a) and $K_x = 0$, $K_y = 0$ (Fig. 5.7f) correspond to the three-wave electromagnetic decay. Comparing Figs 5.7 and 5.8 one can see the broadening effect of unstable regions due to an increase of the initial wave energy. To show the role of various assumptions, the energy densities of down-converted Langmuir waves for all approximations are plotted in Fig. 5.9. The first two plots at this figure show examples obtained in electrostatic and electromagnetic hydrodynamic approximations. Both show a non-physically high energy in the central part around $\mathbf{k} = 0$. Changing linear denominators into non-linear ones no improvement

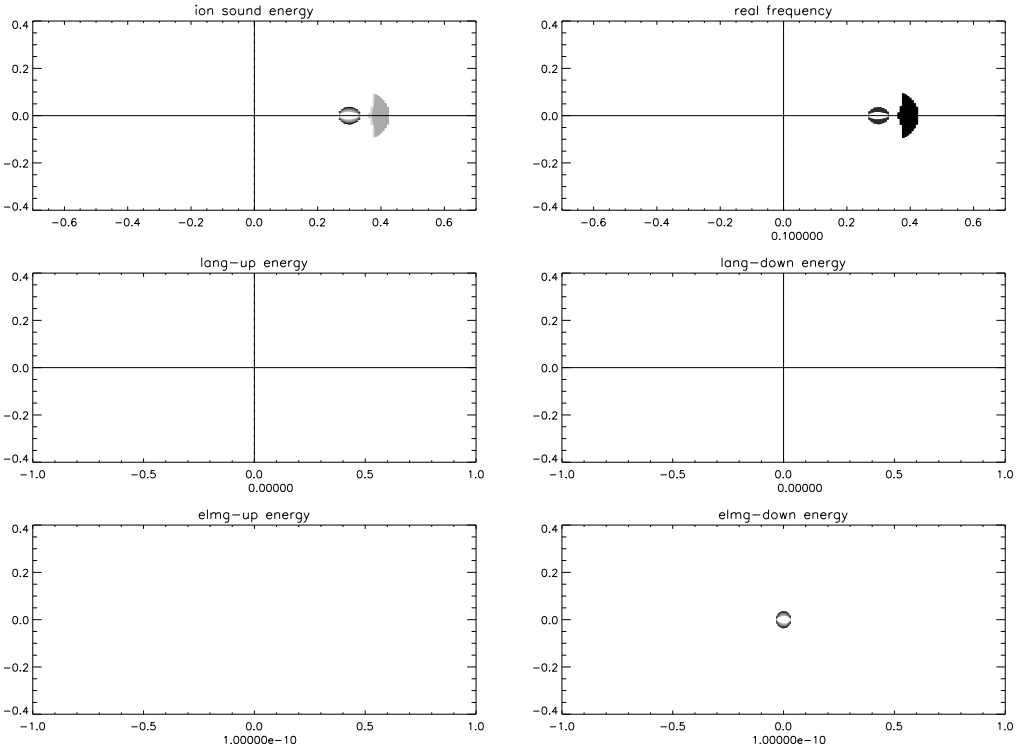

Fig. 5.10: The energy mode distribution for the regime of the decay instability influenced by dampings. The parent wave has $k_0 = 0.3$ and the wave energy $W_0 = 10^{-6}$. The L_3 approximation (5.19) with $T_e/T_i = 4$ and linear dampings of Langmuir and electromagnetic waves (5.6) were used: (a) the contour plot of the phase energy density of ion-sound waves, (b) the contour plot of the real frequency of ion-sound waves, (c) the contour plot of the phase energy density of up-converted Langmuir waves, (d) the contour plot of the phase energy density of down-converted Langmuir waves, (e) the contour plot of the phase energy density of up-converted electromagnetic waves, and (f) the contour plot of the phase energy density of down-converted electromagnetic waves.

was found (Fig. 5.9c). The change was found when the L_3 approximation was used (Fig. 5.9d). The energy around $\mathbf{k} = 0$ disappeared. However, the energy remains dispersed in broad round bands. Furthermore, in the modified decay regime in this approximation no improvement was found. The essential improvement appeared when the quasi-neutrality assumption was removed (Fig. 5.9e). But still there is problem with a distribution of scattered waves. While the energy density maximum is expected for back-scattered waves, the maximum in Fig. 5.9e is on the opposite side. The best result was obtained for the most general approximation (L_3, quasi-neutrality violation, and non-linear denominators) – see Fig. 5.9f.

5.1.2.3 Effects of electrostatic and electromagnetic wave dampings

I was found that the ES and EM wave dampings decrease maxima of growth rates and modify sizes and shapes of unstable regions in the **K**-space. Among many effects of these dampings one applicable example is presented here. It is known, that the initial Langmuir wave can decay into Langmuir or electromagnetic waves (see previous paragraph). According to the relation (e.g. `Zakharov et al. 1985`)

$$W_{th} = \frac{4\nu_i \nu_L}{\sqrt{\mu} k_0}, \tag{5.20}$$

valid for the ES decay the presence of wave dampings (5.6) increases the threshold of instabilities. In natural conditions the initial energy of the parent Langmuir wave is usually low. Due to different thresholds, in this case, the electrostatic decay can be stabilised and the electromagnetic decay is still unstable. An example of this situation is shown in Fig. 5.10. With respect to applications of these results in type III burst theory temperature ratio $T_e/T_i = 4$ was used, which is a typical value observed in the solar wind (`Lin et al. 1986`). This regime of decay instability was suggested in the interpretation of type III bursts (`Thejappa & MacDowall 1998`).

5.1.2.4 Effects of plasma temperature

In the paper by Li and Li (`1993`) it was found that the role of the electromagnetic term in the Zakharov equations increases with temperature increase. This could have a diagnostic significance. For this reason several computations in the regime of electromagnetic decay for several different temperatures were made. The constant amplitude and constant $\mathbf{k}_0$-vector of the parent wave in SI units were assumed. The energy density in the $\mathbf{k}$-space was integrated to obtain the total energy. It was found that this electromagnetic wave energy increases with the temperature increase (asterisks in Fig. 5.11). Then this result was checked analytically. We started from the simplest dispersion equation (5.19). Numerical computations yield the location of the electromagnetic decay process in the $\mathbf{k}$-space and show that generated electromagnetic waves are resonant. These facts allow simplification of the dispersion equation into the quadratic form whose solution (the growth rate and the real frequency) follows:

$$\begin{aligned} \Gamma(\mathbf{K}) &= \frac{\mu W_0 k_0^2 \cdot \sin^2 \alpha^-}{2(\omega_T + \omega_S)^2} \cdot \frac{\nu \omega_T}{\nu^2 + (\omega_T - \omega_S)^2}, \\ Re\{\Omega(\mathbf{K})\} &= \omega_T + \frac{\mu W_0 k_0^2 \cdot \sin^2 \alpha^-}{4(\omega_T + \omega_S)^2} \cdot \frac{\nu^2 + \omega_S^2 - \omega_T^2}{\nu^2 + (\omega_T - \omega_S)^2}, \end{aligned} \tag{5.21}$$

where

$$\omega_T = \frac{3}{2} k_0^2 - \frac{1}{2} \left(\frac{c}{v_T} \right)^2 (\mathbf{k_0} - \mathbf{K})^2,$$

$$\omega_S = \sqrt{\mu \tau K^2 - \nu^2},$$

$$\nu = \sqrt{3\mu \frac{T_i}{T_e}} K,$$

and $\sin^2 \alpha^-$ is defined by relation (5.10). The results corresponding to these formulae are shown in Fig. 5.11 by solid line. In both cases the temperature ratio $T_e/T_i = 4$ observed in the solar wind (`Lin et al. 1986`) was used. One can see that results of both methods are similar. In broad intervals the temperature dependence of the energy transformed into electromagnetic mode can be fitted by power-law functions. For example, in the 1×10^5–3×10^6K interval the power-law exponent is about 3, and in the 1×10^7–5×10^7K interval for numerical results is about 1. Moreover, numerical results show a sharp increase (2 decades) of the transformed energy in the 3×10^6–5×10^6K interval.

5.1.2.5 Effects of the temperature ratio

The temperature ratio T_e/T_i belongs to important plasma parameters, too. It directly influences the ion-sound wave damping – the temperature ratio decrease increases the ion damping, which in the approximations used here can be roughly expressed as $\nu_i \sim \sqrt{T_i/T_e}$. When moreover the

dampings of Langmuir and/or electromagnetic waves are present, thresholds of instabilities increase with the temperature ratio decrease (relation 5.20). However, if these dampings are small or negligible then the results remain qualitatively the same in the broad interval of temperature ratios (from 4 up to 100).

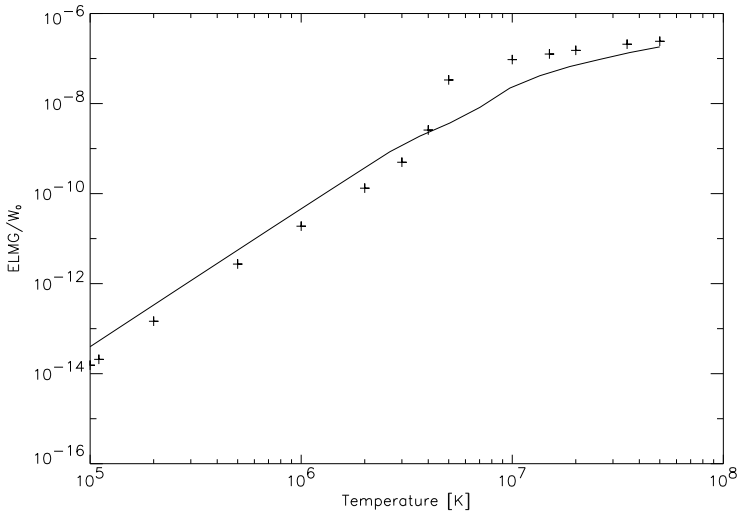

Fig. 5.11: The temperature dependence of electromagnetic wave energy in the regime of decay instability. The energy is expressed as a ratio with the initial parent wave energy. The solid line expresses values from the numerical integration of the analytical formulae (5.21), (5.9), and asterisks show numerical results. Temperature ratio $T_e/T_i = 4$ is used.

It was clearly shown, that parametric instabilities of electrostatic plasma waves represents an efficient wave conversion mechanism. This study, however restricted to the linear stability analysis of parametric processes yields basis for estimation of the efficiency of the wave transformation to the electromagnetic mode under various coronal conditions. Consequently, the relation between some coronal plasma parameters (i.e. temperatures of electronic and ionic components, amplitude of Langmuir waves) and observed values of the radio flux could be found. It would enhance the power of dynamic radio spectroscopy as of solar plasma diagnostic tool significantly.

5.2 Scattering of Langmuir wave-packet on density turbulence

The three- and four-wave non-linear interactions described briefly in the sections 3.3.1.2 and 3.3.2.2 and studied in details in the previous section 5.1 may act as efficient tool for Langmuir wave conversion into the electromagnetic radiation. These processes are favoured (besides other properties) due to the fact that they need not to pre-suppose nothing else than just the parent (pump) Langmuir wave – all other modes included in the interaction are self-generated by instability process. Particularly, ion-sound waves are excited due to ponderomotive force. Nevertheless, one can imagine situation in the flaring solar atmosphere such, that other, external sources (e.g. high-Reynolds-number plasma jets near the reconnection point) of the density turbulence are much more important than the ponderomotive force acting as the source term on the R.H. side of the second Zakharov equation (3.85). Hence, the density turbulence can be regarded as given quantity within the wave conversion problem as its evolution is governed by external forces and not by the Langmuir electric field distribution. Consequently, the second Zakharov equation can be omitted and wave transformation reduces to the scattering of parent electrostatic wave

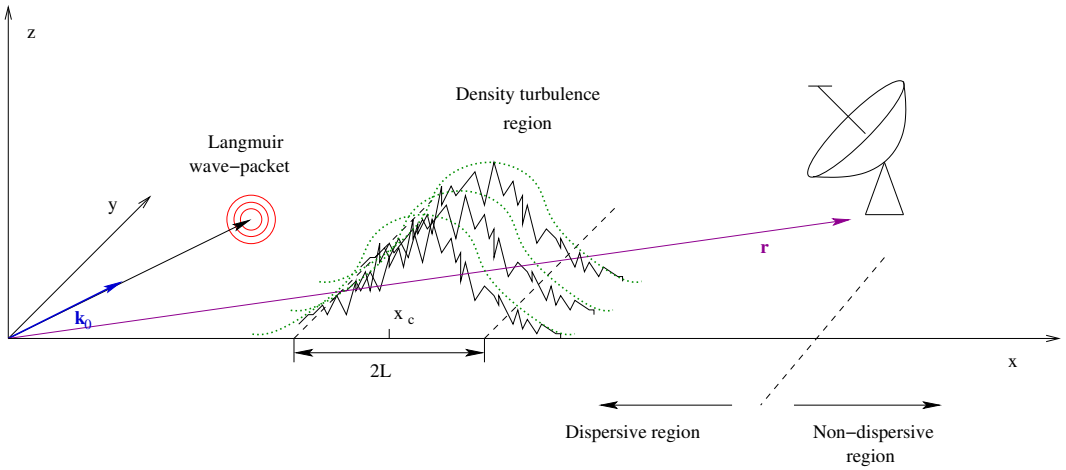

Fig. 5.12: Scattering of Langmuir wave-packets on the localised low-frequency electron density turbulence. Part of the initial Langmuir packet energy is transferred into the electromagnetic mode, detected by radiotelescope in position **r**.

on the density variations into the electromagnetic mode.

Conditions just described above was considered in the Chapter 4 for the modelling of lace bursts and the decimetric spikes. There, the quasi-linear amplification of the upper-hybrid (UH) waves was studied on the background of the MHD turbulence generated by reconnection outflows. The consequent step including the UH waves conversion into the radio radiation was not investigated there and for the sake of simplicity the proportionality between the UH waves energy density and radio flux was assumed. Such an approach was sufficient to make a *qualitative* comparison between observed and modelled data.

Here, on the other hand, the attempt is made to estimate mode conversion efficiency due to scattering of the longitudinal waves into the transversal ones. The Langmuir waves that can be regarded as limiting case of the UH waves for unmagnetised plasmas or for parallel propagation – see dispersion equation (4.2) – are considered here for simplicity. Generation of the UH (Langmuir) waves studied in the Chapter 4 is now viewed as separated problem. One can expects that instability of UH waves interrupted from time to time by the MHD turbulence results in formation of the UH (Langmuir) wave-packets. These are then used as a model input. The scattering (MHD turbulence) region is considered to occupy a limited volume of the corona only. At some distance from the wave interaction region an imaginary radiotelescope is located, at which position the radio flux is determined. The distance is chosen in order to simulate finite dimensions of dispersive region, where the group velocity of the resulting electromagnetic radiation depends (rather strongly) on the frequency. The obtained value of the flux is finally re-calculated for the distance of 1 AU. The general overview of the radio source model is illustrated on the Fig. 5.12.

5.2.1 Basic equations

For time development of the electric field at the radio source as well as at the (imaginative) radiotelescope position the first Zakharov equation with electromagnetic term is supposed (c.f. 5.1, see also `Zakharov et al. 1985`):

$$\left(\frac{\partial^2}{\partial t^2} + c^2\nabla\times\nabla\times - \gamma_e v_{th}^2 \nabla(\nabla\cdot) + \omega_p^2\right)\mathbf{E} = -\omega_p^2\frac{n}{n_0}\mathbf{E}, \tag{5.22}$$

where n_0 and n are the electron density and slowly varying electron density fluctuation, $\mathbf{E}(\mathbf{r},t)$ is the total high-frequency electric field, ω_p is the electron plasma frequency, v_{th} is the electron thermal velocity, and γ_e is the ratio of the specific heats for electrons.

As already mentioned, the slowly varying electron density fluctuations in the radio source are supposed to be given by the hydrodynamic turbulence (due to external sources) and therefore the function $n = n(\mathbf{r},t)$ is prescribed. The Fourier transform of the equation (5.22) yields the expression for $\mathbf{k}$-component of the electric field spectra. It can be written in the scalar form using the local vector base $(\mathbf{e}_{T1}, \mathbf{e}_{T2}, \mathbf{e}_L)$ (see Fig. 5.13):

$$\mathbf{E}(\mathbf{k},t) = \mathbf{e}_L(\mathbf{k}) \cdot E_L(\mathbf{k},t) + \mathbf{e}_{T1}(\mathbf{k}) \cdot E_{T1}(\mathbf{k},t) + \mathbf{e}_{T2}(\mathbf{k}) \cdot E_{T2}(\mathbf{k},t), \tag{5.23}$$

where

$$\mathbf{e}_L(\mathbf{k}) = \frac{\mathbf{k}}{|\mathbf{k}|}, \qquad \mathbf{e}_{T2}(\mathbf{k}) = \frac{\mathbf{k} \times \mathbf{z_0}}{|\mathbf{k}|}, \qquad \mathbf{e}_{T1}(\mathbf{k}) = \mathbf{e}_{T2}(\mathbf{k}) \times \mathbf{e}_L(\mathbf{k}). \tag{5.24}$$

Here $\mathbf{z_0}$ is the unit vector in z-direction and subscripts L, $T1$ and $T2$ represents longitudinal and two polarisations of transversal electric field components, respectively. For each component of the electric field this procedure provides the following ordinary differential equation for independent variable t (time):

$$\frac{\mathrm{d}^2\mathrm{E_i}(\mathbf{k},\mathrm{t})}{\mathrm{dt}^2} + \omega_i^2(\mathbf{k}) E_i(\mathbf{k},t) = -\frac{\omega_p^2}{n_0} \cdot \int \mathbf{e}_i \cdot \mathbf{E}(\mathbf{k}-\mathbf{K},t) n(\mathbf{K},t) \frac{\mathrm{d}^3\mathbf{K}}{(2\pi)^3}, \tag{5.25}$$

where subscript $i \in \{L, T1, T2\}$; $\omega_{i=L}$ stands for

$$\omega_L^2(\mathbf{k}) = \omega_p^2 + \gamma_e v_{th}^2 k^2$$

and $\omega_{i=T1,T2}$ corresponds to (c.f. equations 3.21, 3.20):

$$\omega_{T1}^2(\mathbf{k}) = \omega_{T2}^2(\mathbf{k}) = \omega_p^2 + c^2 k^2. \tag{5.26}$$

In similar way as in the paper by Li and Li (1993) the formal solution of the equation (5.25) can be written as:

$$E_i(\mathbf{k},t) = E_i(\mathbf{k},0)\cos(\omega_i t) + \frac{E_i'(\mathbf{k},0)}{\omega_i} \cdot \sin(\omega_i t) -$$
$$-\frac{\omega_p^2}{n_0 \omega_i} \int_0^t \sin[\omega_i(t-\tau)] \int \mathbf{e}_i \cdot \mathbf{E}(\mathbf{k}-\mathbf{K},\tau) n(\mathbf{K},\tau) \frac{\mathrm{d}^3\mathbf{K}}{(2\pi)^3}\,\mathrm{d}\tau \tag{5.27}$$

Now supposing that the daughter electrostatic and electromagnetic mode amplitudes are small in comparison with the parent Langmuir wave packet over the whole time of interest, the electric field $\mathbf{E}(\mathbf{k}-\mathbf{K},\tau)$ on the right-hand side of the equation (5.27) can be replaced by the electric field $\mathbf{E}_0(\mathbf{k}-\mathbf{K},\tau)$ of the parent Langmuir packet only[1]

$$\mathbf{E}(\mathbf{k},\tau) \approx \mathbf{E}_0(\mathbf{k},\tau). \tag{5.28}$$

Further, let us assume that parent Langmuir waves and also ion-sound waves in the hydrodynamic turbulence evolve according to their linear dispersion equations for simplicity, i.e.:

$$\mathbf{E}_0(\mathbf{k}_0,t) = \mathbf{E}_0^+(\mathbf{k}_0) \cdot \exp[-i\omega_L(\mathbf{k}_0)t] + \mathbf{E}_0^-(\mathbf{k}_0) \cdot \exp[i\omega_L(\mathbf{k}_0)t] \tag{5.29}$$

and

$$n(\mathbf{K},t) = n^+(\mathbf{K}) \cdot \exp[-i\Omega(\mathbf{K})t] + n^-(\mathbf{K}) \cdot \exp[i\Omega(\mathbf{K})t], \tag{5.30}$$

[1] Possibilities of better approach are discussed in the subsection 5.2.4.

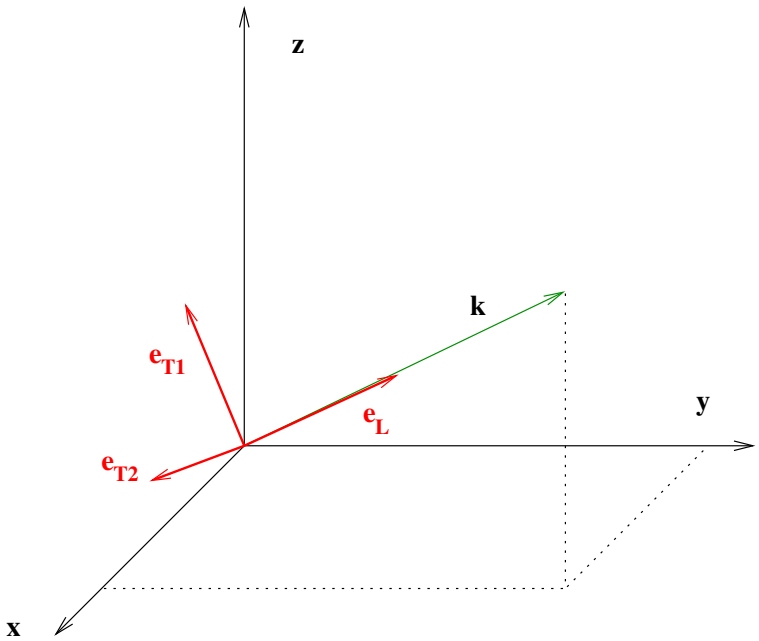

Fig. 5.13: The local vector base $(\mathbf{e}_{T1}, \mathbf{e}_{T2}, \mathbf{e}_L)$ definition.

where $\Omega(\mathbf{K}) = c_s|\mathbf{K}|$ is the ion-sound dispersion relation, c_s is the sound speed. Here the "+" and the "–" signs represent waves moving forward and backward, respectively. Inserting the relations (5.29) and (5.30) into the equation (5.27) and using the reality condition for the Fourier spectra, the electromagnetic daughter waves can be in the only interesting limit of time much greater than plasma period

$$t\omega_p \gg 1$$

expressed as:

$$E_T(\mathbf{k},t) = E_T^+(\mathbf{k}) \cdot \exp(-i\omega_T t) + \bar{E}_T^+(-\mathbf{k}) \cdot \exp(i\omega_T t), \tag{5.31}$$

where

$$E_T^+(\mathbf{k}) = \frac{-i\pi\omega_p^2}{2\omega_T n_0} \int \mathbf{e}_T \cdot \mathbf{E}_0^+(\mathbf{k}+\mathbf{K})\bar{n}^+(\mathbf{K})\delta(\omega_0^+ - \Omega - \omega_T) + \\ + \mathbf{e}_T \cdot \mathbf{E}_0^+(\mathbf{k}-\mathbf{K})n^+(\mathbf{K})\delta(\omega_0^- + \Omega - \omega_T)\,\frac{\mathrm{d}^3\mathbf{K}}{(2\pi)^3} \tag{5.32}$$

with designations

$$\Omega \equiv \Omega(\mathbf{K}) = c_s|\mathbf{K}|, \qquad \omega_0^{\pm} \equiv \omega_L(\mathbf{k}\pm\mathbf{K}) \approx \omega_p + \frac{\gamma_e v_{th}^2}{2\omega_p} \cdot (\mathbf{k}\pm\mathbf{K})^2, \tag{5.33}$$

and

$$\omega_T \equiv \omega_T(\mathbf{k}) \approx \omega_p + \frac{c^2k^2}{2\omega_p}. \tag{5.34}$$

The equation (5.32) has a clear physical interpretation: the delta-functions in the integral represent two surfaces in the $\mathbf{K}$-space, where the resonant conditions

$$\omega_T(\mathbf{k}) = \omega_L(\mathbf{k}+\mathbf{K}) - \Omega(\mathbf{K}) \tag{5.35}$$

or

$$\omega_T(\mathbf{k}) = \omega_L(\mathbf{k}-\mathbf{K}) + \Omega(\mathbf{K}) \tag{5.36}$$

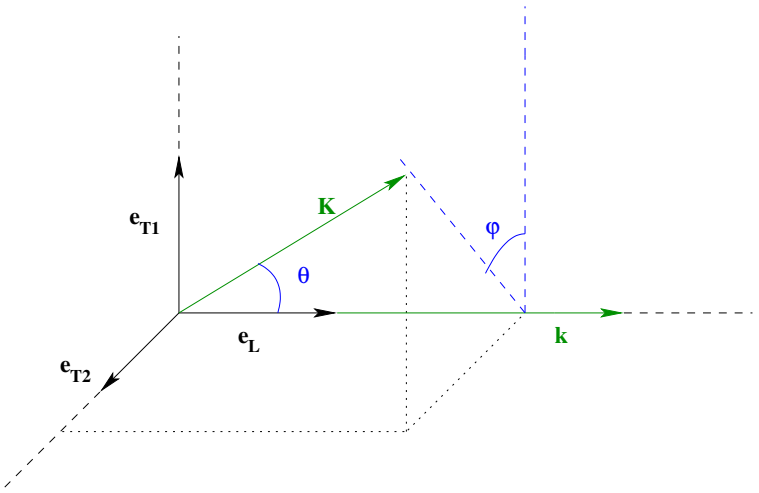

Fig. 5.14: Transformation from Cartesian coordinates (K_x, K_y, K_z) to the pseudo-spherical ones $(\Delta\omega, \theta, \phi)$

are fulfilled. The first one corresponds to the electromagnetic decay, and the second one represents the Langmuir-sound wave coalescence.

Now, using Kelvin's method of stationary phase (e.g. `Leibovich & Seebass 1974`, `Pekárek & Beránek 1979`), the electric field of electromagnetic waves in a position $\mathbf{r}$ (location of radiotelescope) and for sufficiently long time t can be written as:

$$E_T(\mathbf{r},t) = \sqrt{\frac{1}{(2\pi t)^3 \left\|\mathbf{D}(\mathbf{k}_T)\right\|}} \left[E_T^+(\mathbf{k}_T)\cdot \exp[i(\mathbf{k}_T\cdot\mathbf{r} - \omega_T(\mathbf{k}_T)t - 3/4\pi)] + c.c\right], \tag{5.37}$$

where

$$\mathbf{k}_T = \frac{\omega_p}{c}\cdot\frac{\mathbf{r}}{\sqrt{c^2t^2 - r^2}} \tag{5.38}$$

is the wave vector which solves the condition of the stationarity of the phase:

$$\frac{\mathrm{d}}{\mathrm{d}\mathbf{k}}\left[\mathbf{k}\cdot\mathbf{r} - \omega_T(\mathbf{k})t\right] = 0$$

and the $\|\mathbf{D}\|$ designates the determinant of the dispersion tensor:

$$D_{ij}(\mathbf{k}) \equiv \frac{\partial^2\omega_T(\mathbf{k})}{\partial k_i \partial k_j} = \frac{c^2}{\omega_T^2(\mathbf{k})}\left[\omega_T(\mathbf{k})\cdot\delta_{ij} - \frac{c^2}{\omega_T(\mathbf{k})}k_i k_j\right]. \tag{5.39}$$

Inserting now relations (5.26), (5.38) and (5.39) into the equation (5.37), the electric field (one polarisation) in the radiotelescope position can be finally expressed as:

$$E_T(\mathbf{r},t) = \left(\frac{\omega_p}{2\pi}\right)^{3/2} \frac{t}{\sqrt{c}}\left(c^2t^2 - r^2\right)^{-5/4} E_T^+\left[\mathbf{k}_T(\mathbf{r},t)\right] \exp\left[-i\left(\frac{\omega_p}{c}\sqrt{c^2t^2 - r^2} + \frac{3\pi}{4}\right)\right] + c.c. \tag{5.40}$$

Here, the determinant of the dispersion tensor $D_{ij}(\mathbf{k})$ was calculated in the Cartesian coordinate system where $\mathbf{k} = (k, 0, 0)$ and *c.c.* means complex conjugate.

5.2.2 Algorithm used

To compute a time evolution of the electric field strength at a given point (the radiotelescope position) the equation (5.40) is used repeatedly for gradually increasing time. The main problem

is to compute the integral in the equation (5.32) for the parameter $\mathbf{k} = \mathbf{k}_T$ properly. As written above, the delta-functions in this integral describe two surfaces in the **K**-space, where the integrand is non-zero only. At first, one has to split the integral into two parts, where the first one of them describes the decay and the second one the coalescence processes. Then, transforming coordinates in the **K**-space (separately in each part) from original variables (K_x, K_y, K_z) to new ones $(\Delta\omega, \theta, \phi)$ the resonant surfaces in the **K**-space become rectangles in plane and the integration thus simplifies to the two-dimensional case. The angle variables θ, ϕ are defined by relations (see also Fig. 5.14):

$$\cos\theta = \frac{\mathbf{k}\cdot\mathbf{K}}{|\mathbf{k}|\cdot|\mathbf{K}|}$$

and

$$\sin\phi = \frac{(\mathbf{K}\times\mathbf{k})\cdot\mathbf{e}_{T1}}{|\mathbf{K}\times\mathbf{k}|},$$

and the frequency mismatch by

$$\Delta\omega = \omega_L(\mathbf{k}+\mathbf{K}) - \Omega(\mathbf{K}) - \omega_T(\mathbf{k})$$

for decay and

$$\Delta\omega = \omega_L(\mathbf{k}-\mathbf{K}) - \Omega(\mathbf{K}) + \omega_T(\mathbf{k})$$

for coalescence, respectively. Thus, the wave vector **K** expressed in base $(\mathbf{e}_{T1}, \mathbf{e}_{T2}, \mathbf{e}_L)$ can be written partly in the new coordinates as

$$\begin{aligned} K_{T1} &= K\sin\theta\cos\phi \\ K_{T2} &= K\sin\theta\sin\phi \\ K_L &= K\cos\theta \end{aligned} \tag{5.41}$$

where $K = |\mathbf{K}|, \theta \in \langle 0;\pi\rangle, \phi \in \langle 0;2\pi\rangle$. The final relations of the coordinate transformation, which is derived solving the resonant conditions (5.35) and (5.36) and using (5.33) and (5.34), is that one between $\Delta\omega$ and K:

$$K_\pm = \pm\left(-k\cos\theta + \frac{c_s\omega_p}{\gamma_e v_{th}^2}\right) + \sqrt{\left(-k\cos\theta + \frac{c_s\omega_p}{\gamma_e v_{th}^2}\right)^2 + k^2\left(\frac{c^2}{\gamma_e v_{th}^2} - 1\right) + \frac{2\omega_p\Delta\omega}{\gamma_e v_{th}^2}} \tag{5.42}$$

where the sign "+" is valid for decay and sign "–" for coalescence processes, respectively.

Now, the algorithm can be summarised into the following items:

- At first $\mathbf{k}_T$, base vectors $\mathbf{e}_{T1}, \mathbf{e}_{T2}, \mathbf{e}_L$ and $\omega_T(\mathbf{k}_T)$ are computed from the equations (5.38), (5.24) and (5.26) for the fixed position $\mathbf{r}$ at given time t.
- To compute integral (5.32) in new coordinates $\Delta\omega, \theta, \phi$ the θ–ϕ plane is covered by grids. (Note that the integration over the $\Delta\omega$ is trivial due to delta-functions).
  1. Each grid corresponds to specified value of θ and ϕ. Inserting them into the equations (5.42) and (5.41), where the general wave vector $\mathbf{k}$ was replaced by $\mathbf{k}_T$ and $\Delta\omega$ set to zero, the **K**-vector can be computed in the local base $(\mathbf{e}_{T1}, \mathbf{e}_{T2}, \mathbf{e}_L)$ for both decay and coalescence processes.
  2. Then, the **K**-vectors are transformed to the global Cartesian base (K_x, K_y, K_z) using relation
  $$\mathbf{K} = \mathcal{R}\cdot\mathbf{K}_{loc},$$
  where the rotation matrix $\mathcal{R} = (\mathbf{e}_{T1}, \mathbf{e}_{T2}, \mathbf{e}_L)$ has as its columns the base vectors $\mathbf{e}_{T1}, \mathbf{e}_{T2}$ and $\mathbf{e}_L$.

3. At this point quantities $\mathbf{E}_0^+(\mathbf{k}_T \pm \mathbf{K}), n^+(\mathbf{K})$ and $\bar{n}^+(\mathbf{K})$ at the grid with coordinates θ, ϕ can be evaluated, as they are known functions of wave vectors expressed in the global Cartesian coordinates. For the parent Langmuir wave packet the expression

$$\mathbf{E}_0^+(\mathbf{k}) = E_0 \cdot \frac{\mathbf{k}}{k} \cdot \exp\left[-(\mathbf{\Sigma} \cdot (\mathbf{k} - \mathbf{k}_0)) \cdot (\mathbf{k} - \mathbf{k}_0)\right]$$

was used. Here $\mathbf{k}_0$ is the central wave vector of the packet, matrix $\mathbf{\Sigma}$ represents the measure of diffusion of Langmuir waves in the $\mathbf{k}$-space and E_0 is the scaling factor, which determines Langmuir waves intensity . For the ion-sound waves the turbulent spectrum in the form

$$n^+(\mathbf{K}) = n_0 \exp\left[-\frac{(\mathbf{K} - \mathbf{K}_0)^2}{2\sigma_n^2}\right] \cdot \exp[i\phi(\mathbf{K})] * S(\mathbf{K})$$

was used. Here n_0 is the factor determining the strength of the density turbulence, $\phi(\mathbf{K})$ is the random phase, σ_n describes the wave energy spread in the k-space, and the function $S(\mathbf{K})$ is the Fourier transform of the function, which localises the turbulent region - here

$$S(\mathbf{r}) = \exp\left[-\frac{(x - x_C)^2}{2L^2}\right] \otimes 1(y) \otimes 1(z),$$

where x_C is the central position of the turbulent region and L is its characteristic half-width – see Fig. 5.12.

4. Then Jacobian of the coordinate transformation $(K_x, K_y, K_z) \mapsto (\Delta\omega, \theta, \phi)$ is computed as it depends on θ only.

- Values of the integrand from the equation (5.32) (including appropriate Jacobian) on single grids of the θ–ϕ plane are then summed and thus the integration over the $\mathbf{K}$-space is done.

- After multiplying the result of the sum by the factor standing before the integral in the equation (5.32), a computed value of $E_T^+(\mathbf{k}_T)$ is inserted into the equation (5.40).

- When the electric field strength $E(\mathbf{r}, t)$ in the fixed place (the radiotelescope position) $\mathbf{r}$ is completely evaluated, the time t is incremented of time step dt and the next value of the electric intensity $E(\mathbf{r}, t + dt)$ is computed by the same way.

When sufficiently long time sequence of the electric strengths is obtained it will be analysed by the standard Fourier transform to get their power spectra at different times. From sufficiently long and dense series of these spectra the final dynamic radio spectrum at the location of radiotelescope could be constructed using the relation

$$F_{rad}(\omega) = c\varepsilon_0 |\hat{E}(\omega)|^2$$

between the radio flux density F and the Fourier transform $\hat{E}$ of the electric field strength. The flux density is finally re-calculated to that in the Earth orbit distance ($R = 1AU$):

$$F_{Earth} = F_{rad} \cdot \frac{r^2}{R^2},$$

which can be directly compared with observed data.

Background plasmas	
Electron density n_0	1.1×10^{16} m^{-3}
Plasma frequency ω_{pe}	6.0×10^{9} s^{-1}
Electron temperature T_e	25 MK
Langmuir wave-packet	
Central wave vector k_0	85 m^{-1}
Spread in k-space $\Delta k/k_0$	10^{-3}
Electric field amplitude E_L	4.0×10^{-3} Vm^{-1}
Wave energy to plasma thermal en. ratio $\varepsilon_0 \langle E(\mathbf{r},t)^2 \rangle / 2 n_0 k_B T_E$	1.9×10^{-17}
Density turbulence	
Central wave vector K_0	80 m^{-1}
Spread in k-space σ_n/K_0	0.2
Relative RMS of the turbulence $\sqrt{\langle \Delta n^2 \rangle}/n_0$	0.1
Turbulent region localisation	
Position of the centre of the region x_C	500 km
Region half-width L	100 km
Radiotelescope distance $\lvert\mathbf{r}\rvert$	10^4 km

Tab. 5.1: Parameters used in the model of Langmuir wave-packet scattering on the density turbulence region.

5.2.3 First results

Since the model is currently still in the development stage and further improvement in its concept are expected (see the next subsection 5.2.4) only preliminary results can be presented here. The parameters used in the model are summarised in the Tab. 5.1, wave vector geometry is shown on the Fig. 5.15.
The central wave vector of the Langmuir wave-packet was chosen to correspond to the electron beam with speed of c/4, the electric amplitude was adopted from the solar wind measurements (see e.g. `Thejappa & MacDowall 1998`). The density turbulence RMS estimation comes from the the Section 4.1.5 (see also the paper by Karlický et al. (`2001`)); rather broad-band spectrum of turbulence was chosen with random phases included. The distance of the radiotelescope was set to be of the order of the background electron density lenght-scale $L_N = (1/N \cdot |\mathrm{dN/dr}|)^{-1}$.
The results are shown in the Fig. 5.16 where the time profile of the total radio flux re-calculated to the distance of the Earth orbit is presented. From the first analysis it seems, that duration (and consequently also the amplitude) of this elementary burst is given basically due to the frequency dependence of the radio waves group velocity and not by Langmuir wave-packet pass-through-turbulence time as could be expected. Hence, decreasing background electron density is essential for correct modelling of this process – possible improvements of the model are suggested in the subsection 5.2.4. Concerning the low values of radio flux, they should be viewed in context of chosen parameters of the model. Particularly, the model simulates radio radiation from **one** Langmuir wave-packet that, according to parameters given in the Tab. 5.1, is of dimensions about $24 \times 24 \times 24$ m^3 and hence the total energy contained in it is $\approx 10^{-12}$ J. It is likely due to underestimation of the Langmuir electric field amplitude which was directly adopted from the solar wind measurements regardless of very low inferred Langmuir wave energy density to thermal energy density ratio in the coronal conditions (see Tab. 5.1).

Despite these problems the results seem to be promising, however, further improvement of the model is required.

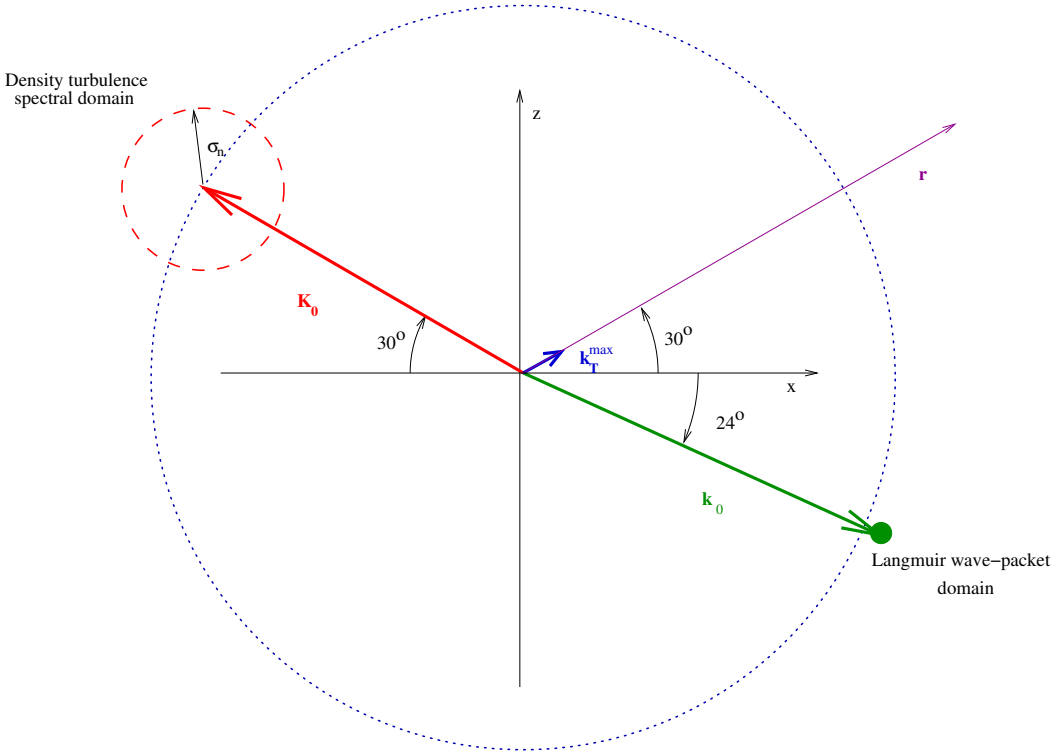

Fig. 5.15: Wave vector geometry used in the model. All wave vectors are situated in the x–z plane. The blue dotted circle schematically depicts the surface in the k-space where the resonant condition 5.36 for the wave coalescence is fulfilled. Wave vector $\mathbf{k}_T^{max}$ corresponds to the maximum of the electromagnetic waves spectrum.

5.2.4 Further development of the model

As was already shown in several papers (e.g. `Robinson 1997`), the problem of Zakharov equations is closely related to the fundamentals of the (non-relativistic) quantum theory. Particularly, the first Zakharov equation (3.84) can be after some scaling rewritten in the form of the Schrödinger equation. This analogy applies also to the currently discussed problem of the Langmuir wave-packet scattering on the density turbulence.

The time evolution of the state marked by ket $|\psi(t)\rangle$ is in the quantum theory usually described using Green operator $\hat{\mathbf{G}}(t, t_0)$ which is implicitly defined by relation

$$\left(i\hbar\frac{\partial}{\partial t} - \hat{\mathbf{H}}(t)\right)\ \hat{\mathbf{G}}(t, t_0) = i\hbar\delta(t - t_0).$$

Then $|\psi(t)\rangle$ can be written as

$$|\psi(t)\rangle = \hat{\mathbf{G}}(t, t_0)\ |\psi(t_0)\rangle \tag{5.43}$$

and the Green operator fulfils the relation

$$\hat{\mathbf{G}}(t, t_0) \equiv \hat{\mathbf{G}}(t, t_0) \cdot \Theta(t - t_0), \tag{5.44}$$

where $|\psi(t_0)\rangle$ is the initial state at the time t_0 and $\Theta(t - t_0)$ is the Heaviside function. It is often convenient, particularly in the case of particle interaction with external fields localised in some region, to split the Hamiltonian operator of the problem into two parts

$$\hat{\mathbf{H}}(t) = \hat{\mathbf{H}}_0(t) + \hat{\mathbf{H}}_I(t)$$

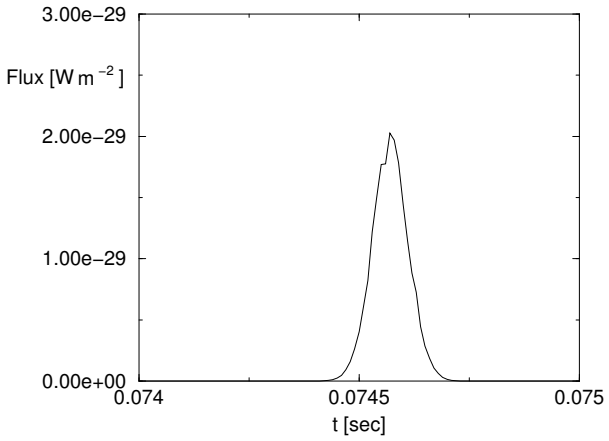

Fig. 5.16: Time-profile of the total radio flux re-calculated to the Earth orbit distance.

describing "free" particle propagation and the interaction with external fields itself, respectively. Then, the Green operator satisfies fundamental integral equation (e.g. `Formánek 1983`)

$$\hat{\mathbf{G}}(t,t_0) = \hat{\mathbf{G}}_0(t,t_0) - \frac{i}{\hbar}\int_{-\infty}^{\infty} \hat{\mathbf{G}}_0(t,\tau)\hat{\mathbf{H}}_I(\tau)\hat{\mathbf{G}}(\tau,t_0)\ \mathrm{d}\tau, \tag{5.45}$$

where $\hat{\mathbf{G}}_0(t,t_0)$ is the Green operator corresponding to free Hamiltonian $\hat{\mathbf{H}}_0$. Hence, the state $|\psi(t)\rangle$ evolves in time according to the formula

$$|\psi(t)\rangle = \hat{\mathbf{G}}_0(t,t_0)|\psi(t_0)\rangle - \frac{i}{\hbar}\int_{t_0}^{t} \hat{\mathbf{G}}_0(t,\tau)\hat{\mathbf{H}}_I(\tau)|\psi(\tau)\rangle\ \mathrm{d}\tau. \tag{5.46}$$

where the property (5.44) of the Green operator was used. Setting $t_0 = 0$ the close analogy between the equations (5.46) and (5.27) is obvious. Consequently, the problem under study (the scattering of wave-packets on the density turbulence) can be translated into the quantum theory language as problem of the particle interaction with non-stationary external fields acting in some localised region.

The solution of the eq. (5.45) is found by the iterative procedure to be (`Formánek 1983`):

$$\hat{\mathbf{G}}(t,t_0) = \hat{\mathbf{G}}_0(t,t_0) + \sum_{n=1}^{\infty} \hat{\mathbf{G}}_n(t,t_0) \tag{5.47}$$

with

$$\hat{\mathbf{G}}_n(t,t_0) \equiv \left(-\frac{i}{\hbar}\right)^n \times$$
$$\times \int_{-\infty}^{\infty} \mathrm{dt_n} \int_{-\infty}^{\infty} \mathrm{dt_{n-1}} \ldots \int_{-\infty}^{\infty} \mathrm{dt_1} \hat{\mathbf{G}}_0(\mathrm{t},\mathrm{t_n})\hat{\mathbf{H}}_\mathrm{I}(\mathrm{t_n})\hat{\mathbf{G}}_0(\mathrm{t_n},\mathrm{t_{n-1}}) \ldots \hat{\mathbf{H}}_\mathrm{I}(\mathrm{t_1})\hat{\mathbf{G}}_0(\mathrm{t_1},\mathrm{t_0})$$

and it represents the basic relation of the non-stationary perturbation quantum theory. Comparing this result with the approximation (5.28) used in the present analysis (with respect to analogy between the equations 5.46 and 5.27) it is clear, that the approximation used here corresponds to the first order ($n = 1$) of the iterations (5.47).

Resuming this discussion, there are two directions in which the model can be improved using the described analogy with the related quantum theory problem:

1. Hamiltonian splitting. The well chosen splitting of potential (which corresponds to the electron density by this analogy) enables one to solve the problem even in the case of the non-homogeneous (but stationary) background electron density. This would allow to take into account decreasing electron density distribution in the solar corona and, hence to solve recognised problem of overestimated radio wave-packet dispersion.

2. There is plenty of already developed methods of solving the problems of the non-stationary perturbation quantum theory now. This analogy enables their use also for the studied case of Langmuir wave-packet scattering on the density turbulence.

Both just suggested improvements of the model are matter of the future work.

References

Abalde J.R., Alves M.V., Chian A.C.-L., 1998, A&A 331, L21

Akimoto K., 1988, Phys. Fluids 31, 538

Anzer, U., 2002, 10^{th} European Solar Physics Meeting "Solar variability: From core to outer frontiers", Prague, The Czech republic

Aschwanden, M.J., Dennis, B.R., & Benz, A.O., 1998, ApJ 497, 972

Aschwanden, M.J., 1990, A&AS 85, 1141

Aschwanden, M.J., Güdel, M., 1992, ApJ 401, 736

Aschwanden M.J., Treumann R.A., 1997, in Coronal Physics from Radio and Space Observations (ed. G. Trottet), Lecture Notes in Physics 483, p. 108

Bárta, M., Karlický M., 1999, 9^{th} European Solar Physics Meeting, "Magnetic field and solar processes", Florence, Italy

Bárta, M., Karlický M., 2000, A&A 353, 757

Bárta, M., Karlický M., 2000b, 5^{th} Hvar Astrophysical Colloquium, "Physical processes in the solar atmosphere", Hvar, Croatia

Bárta, M., Karlický M., 2001, A&A 379, 1045

Benz, A.O., 1986, Sol. Phys. 104, 99

Benz A.O., 1993, Plasma Astrophysics, Kluwer Acad. Publ., Dordrecht, The Netherlands

Cairns I.H., Robinson P.A., Smith, N.I., 1998, J. Geophys. Res. 103, 287

Cairns I.H., Robinson P.A., 1998, ApJ 509, 471

Chen, F.F., 1984, Introduction to plasma physics, Academia Publ., Prague, Czechoslovakia (in Czech)

Sawant, H.S., Subramanian, K.R., Faria, C., Fernandes, F.C.R., Sobral, J.H.A., Cecatto, J.R., Rosa, R.R., Vats, H.O., Neri, J.A.C.F., Alonso, E.M.B., Mesquita, F.P.V., Portezani, V.A., Martinon, A.R.F., 2001, Sol. Phys. 200, 167.

Fleishman, G.D., Melnikov, V.F., 1998, Uspechi fizicheskich nauk 168, 1265 (in Russian)

Fleishman, G.D., Yastrebov, S.G., 1994, Sol. Phys. 154, 361

Formánek, J., 1983, Introduction to quantum theory Academia Publ., Prague, Czechoslovakia (in Czech)

Fu, Q.J., Li, C.S., Yin, S.Z., 1985, Kunming Workshop on Solar Physics and Interplanetary travelling phenomena, ed. C. de Jager & C. Biao (Science Press, Beijing), 560

Garcia, H.A., 1995, ApJ 420, 422-432

Ginzburg, V.L., Zheleznyakov, V.V., 1958, Astron. Zh., 35, 694

Güdel, M., 1990, A&A 239, L1

Güdel, M., Benz, A.O., 1990, A&A 231, 202

Holman, G.D., Eichler, D., Kundu, M., 1980, in Radio Physics of the Sun, ed. M. Kundu & T. Gergely, IAU Symp. 86, 465

Isliker, H., Benz, A.O., 1994, A&AS, 104, 145

Jiřička, K., Karlický, M., Kepka, O., Tlamicha A. 1993, Solar Phys. 147, 203.

Jiřička, K., Karlický, M., Mészárosová, H., & Snížek, V. 2001, A&A 375, 243

Karlický, M., 1984, Sol. Phys. 92, 329

Karlický, M., 1988, Bull. Astron. Czech. 39, 13

Karlický, M., Sobotka, M., Jiřička, K., 1996, Sol. Phys. 168, 375

Karlický, M., Jiřička, K., Sobotka, M., 2000, Sol. Phys. 195, 165

Karlický, M., Bárta, M., Jiřička, K., Mészárosová, H., Sawant, H.S., Fernandes, F.C.R., Cecatto, J.R., 2001, A&A 375, 638

Krüger A., 1979, Introduction to Solar Radio Astronomy and Radio Physics, D. Reidel Publ. Comp., Dordrecht, Holland

Kuijpers, J., Van der Post, P., Slottje, C., 1981, A&A 102, 331

Kundu M.R., 1965, Solar Radio Astronomy, Interscience Publ., New York

Ledenev, V.G., Karlický, M., Yan, Y., Fu, Q., 2001, Sol. Phys. 202, 71

Leibovich, S., Seebass, A.R., 1974, Nonlinear waves, Cornell Univ. Press, London

Li L.H., Li X.Q., 1993, Phys. Fluids B 5, 1

Lin R.P., Levedahl W.K., Lotko W., Gurnett D.A., Scarf F.L., 1986, ApJ 308, 954

Martens, P.C.H., Kuin, N.P.M., 1989, Solar Phys. 122, 263

McLean, D.J., Labrum, N.R., 1985, Solar Radiophysics, Cambridge University Press, Cambridge, UK

Melrose, D.B., 1975, Solar Phys., 43, 211

Melrose, D.B., 1980, Plasma Astrophysics, Gordon & Breach, London, UK

Melrose, D.B., Dulk, G.A., 1982, ApJ 259, 844

Messmer, P., Benz, A.O., 2000, A&A 354, 287

Mészárosová, H., Karlický, M., Veronig, A., Zlobec, P., Messerotti, M., 2000, A&A 360, 1126

Mikhailovsky, A.B., 1975, Theory of Plasma Instabilities Vol. I, Nauka Publ., Moscow, Russia (in Russian)

Moffat, H.K., 2000, in "New trends in turbulence", Les Houches Ser. LXXIV, Springer, Paris, France, p. 321

Newkirk, G., 1967, Annual Rev. Astron. Astrophys., 5, 213

Pekárek, L., Beránek, J., 1979, Czechosl. Journal for Physics, A 29, 1 (in Czech)

Priest, E.R., 1984, Solar Magnetohydrodynamics, D, Reidel Publishing Comp., Dordrecht, Holland

Robinson P.A., Cairns I.H., Willes A.J., 1994, ApJ 422, 870

Robinson, P.A., 1997, Review of Modern Physics 69, 507

Saito, K., 1970, Ann. Tokyo Astron. Obs., Ser. 2, 12, 53

Schwarz, U., Benz, A.O., Kurths, J., Witt, A., 1993, A&A 277, 215

Schwenn, R., 2002, 10^{th} European Solar Physics Meeting "Solar variability: From core to outer frontiers", Prague, The Czech republic

Schwen, R., Marsch, E., 1991, Physics of the Inner Heliosphere Vol. II (Springer-Verlag, Berlin), 210

Slottje, C., 1981, Atlas of Fine Structures of Dynamic Spectra of Solar Type IV-dm and Some Type II Radio Bursts, Dwingeloo Observatory, The Netherlands

Sreenivasan, K.R., 2000, in "New trends in turbulence", Les Houches Ser. LXXIV Springer, Paris, France, p. 56

Stähli, M., Magun, A., 1986, Sol. Phys. 104, 117

Stepanov, A.V., Kliem, B., Krüger, A., Hildebrandt, J., Garaimov, V.I., 1999, ApJ 524, 961

Tajima, T., Benz, A.O., Thaker, M., Leboeuf, J.N., 1990, ApJ 353, 666

Thejappa, G., MacDowall, R.J., 1998, ApJ 498, 465

Uchida, Y., 1960, Publ. Astron. Soc. Japan, 12, 376

Varady, M., 2002, Observations and modelling of plasma loops in solar corona, doctoral thesis

Vernazza, J.E, Avrett, E.H., Loeser, R., 1981, ApJS 45, 635

Vlahos, L., Sharma, R.R., 1984, ApJ 290, 347

Wentzel, D.G., 1991, ApJ 373, 285

Wild, J.P., 1950, Aust. J. Sci. Res., Ser. A, 3, 541

Wild, J.P., 1962, Publ. Astron. Soc. Japan, 17, 249

Wild, J.P., McCready, L.L., 1950, Aust. J. Sci. Res., Ser. A, 3, 387

Willes, A.J., Robinson, P.A., 1996, ApJ 467, 465

Winglee, R.R., Dulk, G.A., Pritchett, P.L., 1988, ApJ 328, 809

Wu, C.S., Li, L.C., 1979, ApJ 230, 621

Zaitsev, V.V., 1966, Soviet Astron. – AJ, 9, 572

Zakharov V.E., 1972, Zh.Exp.Theor.Fiziky 62, 1745

Zakharov V.E., 1984, in Handbook of Plasma Physics (eds. A.A. Galeev and R.N. Sudan), North Holland Prss Comp., Amsterdam, The Netherlands, Vol. 2, p. 81

Zakharov V.E., Musher S.L., Rubenchik A.M., 1985, Physics Reports 129, p. 317

Zheleznyakov, V.V., Zlotnik, E. Ya., 1975, Sol. Phys. 44, 461

Zlobec, P., Karlický, M., 1998, Sol. Phys. 182, 477

On-line references

BBSO website: http://www.bbso.njit.edu/cgi-bin/LatestImages

HXRS website: http://www.asu.cas.cz/HXRS/

FASR home webpage: http://www.ovsa.njit.edu/fasr/

H. Hudson's flare models archive: http://isass1.solar.isas.ac.jp/~hudson/cartoons/overview.html

Ondřejov MFS website: http://www.asu.cas.cz/~pkotrc/index.html

NoRH home webpage: http://solar.nro.nao.ac.jp/norh/

RHESSI website: http://hesperia.gsfc.nasa.gov/hessi/

SOHO home webpage: http://soho.estec.esa.nl/ (*SOHO is a project of international cooperation between ESA and NASA*)

SpaceScience.com: http://spacescience.spaceref.com/ssl/pad/solar/default.htm

Ondřejov Solar Patrol site: http://www.asu.cas.cz/~sunwatch/index.html

TRACE home pages: http://vestige.lmsal.com/TRACE/

Yohkoh website: http://isass1.solar.isas.ac.jp/

OSRA Tremsdorf homepage: http://www.aip.de/groups/osra/

Ondřejov solar radiodata webpage: http://www.asu.cas.cz/~radio/

INAF Trieste solar radioastronomy pages: http://radiosun.ts.astro.it

Acknowledgements

It is really pleasant obligation of the author to thank several people and institutions who contributed greatly to successful completion of this thesis.

Above all I would like to thank my colleagues from the Solar Department of the Astronomical Institute Ondřejov for establishing very pleasant and creative atmosphere that has helped me in my work even by itself. My warmest thanks belong namely to the supervisor Dr. Marian Karlický without whose inspirative ideas, informal initiation as well as kind correction of my work this thesis hardly could be finished.

This work was partly supported by grants A 3003 707 and A 3003 202 by AS ČR. Concerning the financial support I would like to appreciate also that by European Commission whose grants allowed me to participate in several scientific meetings and conferences.

Very nice and illustrative pictures are by courtesy of corresponding institutions and consortia. My thanks belong particularly to the SOHO, Yohkoh, RHESSI and TRACE teams as well as other institutions whose data were used in the thesis – namely to AIP–OSRA Tremsdorf, INAF Trieste (Bassovizza Solar Radio Observatory), and – of course – to the Astronomical Institute Ondřejov.

It surely worths to note that almost all the work on this thesis was made using free GNU tools under LINUX environment - above all C/C++ compiler, LaTeX desktop publishing system, Emacs editor, and many others. I really appreciate all the people connected with this great, unselfish project.

Finally, I would like to thank my family and friends for moral support during my doctoral studies.

Ondřejov, November 6, 2002 Miroslav Bárta